Master's thesis

NTNU
Norwegian University of Science and Technology
Faculty of Information Technology and Electrical Engineering
Department of Electric Power Engineering

Casper Leonard Klop

ModHVDC

Forces and vibrations in a Modular HVDC Generator

Master's thesis in The European Wind Energy Master
Supervisor: Pål Keim Olsen
Co-supervisor: Jianning Dong
August 2022

NTNU
Norwegian University of
Science and Technology

TU Delft

Casper Leonard Klop

ModHVDC

Forces and vibrations in a Modular HVDC Generator

Master's thesis in The European Wind Energy Master
Supervisor: Pål Keim Olsen
Co-supervisor: Jiannning Dong
August 2022

Norwegian University of Science and Technology
Faculty of Information Technology and Electrical Engineering
Department of Electric Power Engineering

NTNU
Norwegian University of
Science and Technology

Preface

With this thesis, the European Wind Energy Master comes to an end for me. It was a journey that led me to Copenhagen, Delft and Trondheim, and that taught me so many things, both academically and personally.

I would like to thank Jianning Dong and Pål Keim Olsen for their supervision. Our meetings made me get a better grasp of the multidisciplinary field of electrical machines, which I very much enjoyed. I'm also grateful to Michiel, Runar and Yannick for our talks about machine design, and to Nils Petter Vedvik and Xuezhou Wang for their insights on the mechanical aspect of this thesis.

Finally, I would like to thank everyone involved in the EWEM organization for making this program possible, and all the people I have met along the way. This one's for you.

C.L. Klop
Delft, July 2022

Summary

Offshore wind energy is expected to play a major role in the upcoming energy transition. For long distances to shore, it is preferable to connect the wind farms to land by means of High-Voltage DC (HVDC) cables to reduce losses and costs. This currently poses challenges, as wind turbine generators produce variable-frequency low-voltage AC power, which needs to be converted to HVDC with heavy transformers in the wind turbine nacelle and large offshore substations. One proposed solution is to develop integrated drives which produce HVDC directly inside the nacelle, by segmenting the stator of a direct-drive generator. Each segment has its own dedicated Power Electronic (PE) converter, of which the DC output is connected in series.

This thesis studies one of the challenges of this Modular HVDC generator concept: the segmented stator generates additional vibrations in the structure, and will respond differently to the occurring forces than a stator without segmentation. The goal is to design a concept for the structure that holds the segments in place, while still allow individual modules to be replaced after failure.

As a first step, the machine design is updated taking into account saturation and design limits which were neglected in previous studies. For a 10 MW Direct-Drive generator with an output DC-link voltage of 100 kV, a 10 m diameter inner-rotor Permanent Magnet Synchronous Generator (PMSG) with Fractional-Slot Concentrated Windings (FSCW) is designed. It has 384 slots and 320 poles, and the stator is split in 16 segments. The design is verified with Finite-Element simulations in COMSOL.

Secondly, the electromagnetic effects of the flux barriers created by the insulated gaps between the segments are analyzed analytically and numerically. The analytical model of the magnetic fields and forces agrees well with the numerical simulations in COMSOL. The FSCW result in a broad spectrum of vibrations, including a strong slot harmonic caused by the open slots. Segmentation of the stator has two important consequences: the addition of radial harmonics with a low spatial order at multiples of the number of segments, called the segment harmonics, and an increase in the cogging torque. These effects are more pronounced in the numerical simulations than in the analytical model, due to the change of the magnetic flux distribution in the segmented stator, which is neglected in the analytical calculations. Furthermore, time harmonics in the current due to the PE converters are found to significantly increase the breathing mode and torque ripple.

Thirdly, the mechanical response of two different design concepts has been analyzed by performing a modal analysis. The first design uses an interference fit, where the segments are pressed into the frame and held in position by friction. This design behaves similarly to a ring-shaped frame, and has the same eigenmodes at similar eigenfrequencies. The second design uses beams between the frame and stator to support the segments. In this case, the stiffness and structural integrity of the design is significantly reduced, leading to larger deflections and lower eigenfrequencies.

Combining the obtained forces and eigenmodes, it is concluded that the breathing mode, the segment harmonics and the slot harmonics cause the strongest vibrations. The amplitude of the forces causing the first two is low, but the mechanical stiffness of these modes is low and the excitation frequency is close to the eigenfrequency. The slot harmonic is mainly important due to the low spatial order and large amplitude of the force, caused by the combination of concentrated windings and open slots. The PE converter harmonics will not lead to a stronger breathing mode vibration due to the high switching frequency of the converters, but could create resonance of the slot harmonic.

Based on these results, both designs were found to be feasible from an electromechanical perspective, as long as care is taken to mitigate the vibrations caused by the segment harmonics, and resonance of the PE converter harmonics is prevented. Due to the uncertainty of the mechanical model, experimental validation of the eigenfrequencies and the vibration levels is recommended, which can be done by using modal analysis.

Contents

Nomenclature

Symbols

Symbol	Definition	Unit
A	Deflection amplitude	[m]
B	Magnetic flux density (scalar)	[T]
$\mathbf{B}$	Magnetic flux density (vector field)	[T]
c	Damping coefficient	[Ns/m]
d_s	Slot depth	[m]
E	Young's modulus	[Pa]
$\mathbf{E}$	Electric field	[V/m]
E_p	Back-EMF	[V]
$F1$	Number of machine sections	[-]
F_d	Torque density	[kN/m^2]
f	Force density	[N/m^2]
f_e	Electrical frequency	[Hz]
f_p	Penalty factor (COMSOL)	[-]
G	Shear modulus	[Pa]
g	Air gap	[m]
h	Height/thickness	[m]
h	Time harmonic	[-]
i/I	Current	[A]
i	Relative permeance harmonic	[-]
J	Current density	[A/mm^2]
K_m	Stiffness of mth mode	[N/m]
K_s	Linear current density	[A/m]
k	Spring stiffness	[N/m]
k_c	Carter coefficient	[-]
k_{cp}	Conductor packing factor	[-]
k_{so}	Slot opening factor	[-]
k_{st}	Lamination stacking factor	[-]
k_w	Winding factor	[-]
k_τ	Rotation factor	[-]
L	Inductance	[H]
L	Length	[m]
l_m	Magnet length	[m]
M	Magnetization	[A/m]
M	Mass	[kg]
M_{ij}	Mutual inductance of phase i and j	[H]
m	Force order harmonic	[-]
N_L	lcm $(N_s, 2p)$	[-]
N_{ph}	Number of phases	[-]
N_s	Number of slots	[-]
N_{seg}	Number of segments	[-]
N_t	Number of turns in series	[-]
n	Axial vibration mode	[-]
n_s	Number of turns per slot	[-]
P	Nominal power	[W]
P_c	Permeance coefficient	[-]

Symbol	Definition	Unit
p	Number of pole pairs	[-]
q	Number of slots per pole per phase	[-]
R	Resistance	[Ω]
R	Radius	[m]
r	Radial position	[m]
S	Rotation speed	[RPM]
$\mathbf{S}$	Poynting vector	[W/m^2]
s_b	Phase belts per phase	[-]
T	Torque	[Nm]
T_c	Cogging torque	[Nm]
t	Time	[s]
$\mathbf{u}$	Displacement vector	[m]
V	Line-to-line voltage	[V]
V_r	Rotor volume	[m^3]
v	Armature spatial harmonic	[-]
w	Width	[m]
X	Reactance	[Ω]
Y	Quasi-static deflection	[m]
Z	Impedance	[Ω]
α_m	Magnet fraction	[-]
β	Pitch	[rad]
Γ_s	Core loss density	[W/kg]
δ	Interference	[m]
ϵ_0	Permittivity of vacuum	[F/m]
ζ	Damping coefficient	[-]
η	Efficiency	[-]
η_m	Magnification factor of mth order	[-]
θ	Angular position	[rad]
κ	Non-dimensional thickness	[-]
Λ_{g0}	Constant air gap permeance	[H]
λ	Relative permeance	[-]
λ	Non-dimensional length	[-]
μ	Rotor field spatial harmonic	[-]
μ_0	Permeability of vacuum	[H/m]
μ_s	Static friction coefficient	[-]
ν	Poisson ratio	[-]
ρ	Density	[kg/m^3]
σ	Conductivity	[S/m]
$\overleftrightarrow{\boldsymbol{\sigma}}$	Maxwell stress tensor	[N/m^2]
φ	Phase angle	[rad]
ϕ	Flux	[Wb]
ω	Angular velocity/frequency	[rad/s]
ω^*	Eigenfrequency	[rad/s]
Ω	Frequency parameter (Donnell-Mushtari)	[-]

Abbreviations

Abbreviation	Definition
2L-VSC	Two-Level Voltage Source Converter
DD	Direct-Drive
FEA	Finite-Element Analysis
FFT	Fast-Fourier Transform
FRF	Frequency-Response Function
FSCW	Fractional-Slot Concentrated Windings
LCM	Lowest Common Multiple
ModHVDC	Modular High-Voltage Direct Current
HVDC	High-Voltage Direct Current
PE	Power Electronics
PM	Permanent Magnet
PMSG	Permanent Magnet Synchronous Generator
PWM	Pulse-Width Modulation
RPM	Rotations per minute
RMS	Root Mean Square

Sub- and superscripts

Symbol	Definition
arm	Armature
bi	Back-iron
c	Stator core
d	Direct axis
e	Electrical
f	Frame
g	Air gap
gap	Flux gap between segments
h	Time harmonic
i	Inner
LL	Line-to-line
m	Force harmonic order
n	Axial vibration mode
o	Outer
p	In-plane
ph	Phase
q	Quadrature axis
r	Radial
r	Rotor
s	Stator/slot
so	Slot opening
t	Tangential
th	Teeth
v	Armature field spatial harmonic
w	Winding
y	Yoke
z	Out-of-plane axis
μ	Rotor field spatial harmonic

List of Figures

List of Tables

1

Introduction

In the coming decades, a rapid energy transition is needed to limit the effects of anthropogenic climate change. In order to approach the targets set by the Paris Agreement, the capacity of low-emission energy sources needs to increase more than tenfold by 2030 [39]. Offshore wind energy is expected to play a key role in this transition, with the International Energy Agency (IEA) predicting the EU capacity to increase from 18 GW in 2018 to 80 GW in 2030 [38]. Even higher ambitions have been put forward following the 2021-2022 energy crisis, with an important role for offshore energy in the North Sea [81].

With wind farms moving further away from shore, the transmission costs are becoming a significant part of the total offshore energy costs, potentially over 20% of the upfront capital costs [38]. High-Voltage DC (HVDC) transmission cables offer a potential for cost reduction, but this requires high-power substations collecting and converting the variable AC output of the wind turbines to HVDC before transmission, as shown in Figure 1.1 [25]. Improving the transmission infrastructure of offshore wind energy is one of the key technological innovation requirements that is identified by the IEA.

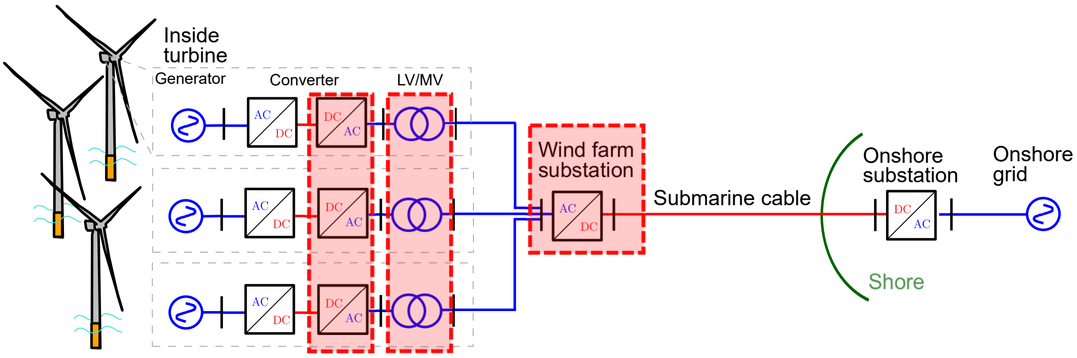

Figure 1.1: The layout of an offshore wind farm, connected to shore with a HVDC cable. The components that could be eliminated with a HVDC generator are shown in red [25].

The envisioned goal of the Modular HVDC generator project is to simplify the offshore transmission system by using a segmented generator with integrated power converters. By connecting the DC output of each module in series, the generator is capable of producing HVDC within the wind turbine nacelle. This eliminates the need of a transformer inside the wind turbine, and possibly the need of a large offshore substation, as shown in Figure 1.1 as well [30, 52]. This could improve the reliability and efficiency of the offshore wind energy system, and thus reduce its cost.

To be able to connect the DC output of each module in series, the stator segments need to be insulated from each other. This influences the electromagnetic fields inside the machine, the structural integrity of the stator and thermal management system of the generator. The machine will be discussed in more detail in Chapter 2.

1.1. Reason for research

Splitting the generator into modules creates multiple challenges, especially regarding the insulation of the segments and the control system of the array of power converters. The structural aspects of the machine have also been identified as challenge [30, 52]. The reason is twofold:

1. The insulated gaps between the segments act as flux barriers, changing the magnetic fields and forces occurring in the machine
2. The structural integrity of the stator is compromised, while it is known that large generators using concentrated windings and open slots experience a high level of vibrations [71].

Vibrations in electrical machines have been studied extensively, often in relation to the resulting noise resulting from these vibrations [28, 69]. Vibrations of segmented machines have not been researched in detail, and existing research often focused on E-cores for relatively small machines [20, 27, 34]. This thesis aims to contribute to the understanding of the effect of modularity on the vibrations occurring in a large electrical machine.

1.2. Research questions

The goal of this thesis is to study and design the structural support of the stator segments in a 10 MW Direct-Drive Modular HVDC generator. Subquestions of this goals include:

1. Which forces occur due to the magnetic field in the proposed ModHVDC machine?
    - What is the influence of the flux gaps on the magnetic field and the resulting forces?
    - What is the influence of the PE converter on the magnetic field and the resulting forces?
2. How do the laminated stator segments respond to the air gap forces?
3. Which designs for the stator-frame mount are feasible, taking into account cooling and electrical insulation?

These questions will be studied both with an analytical model in MATLAB[1] and a numerical simulation in COMSOL, and their results will be compared. Finally, the conclusions of this report will be used to formulate design rules for the stator segments of the ModHVDC machine.

---

[1] All code is available on `https://github.com/CasperKlop/Thesis`. Figures labeled with an asterisk (*) are available as animated GIFs to visualize their time development.

1.3. Structure

The first two chapters of this thesis report describe the background of the ModHVDC concept, and the machine design used in this research. An overview of the following analysis is shown in Figure 1.2, which consists of the following chapters:

- Chapter 4 describes the analytical analysis of the electromagnetic fields and the resulting forces
- Chapter 5 describes the mechanical model, including an analytical analysis of the eigenfrequencies of the system
- Chapter 6 describes the numerical analysis performed in COMSOL to simulate both the electromagnetic fields and the mechanical response of the stator system
- Chapter 7 discusses the experiments that can be performed to improve and validate the mechanical model

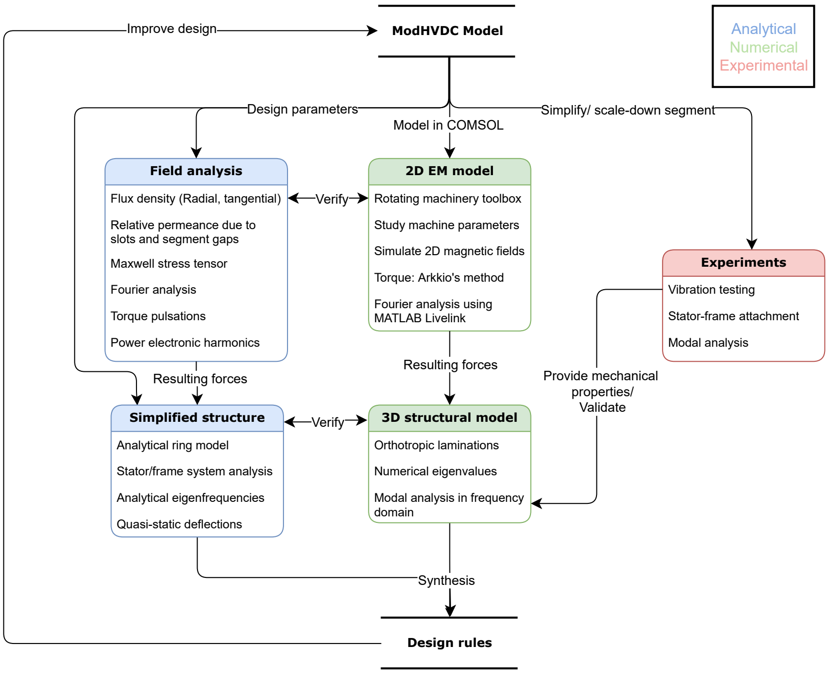

Figure 1.2: Approach for research conducted in this thesis

2

Background

The ModHVDC generator concept will in this thesis be considered in the particular application of a 10 MW Direct-Drive Wind Turbine, with a 100 kV DC link output. This chapter will introduce the concept and the background reasons for this research.

2.1. The ModHVDC concept

The proposed system is an integrated Permanent Magnet Synchronous Generator (PMSG), capable of producing High-Voltage Direct Current (HVDC) without the need of a transformer. This is achieved by dividing the system into multiple modules. Each module consists of a segment of the stator, which acts as an individual three-phase generator, and a dedicated AC-DC power converter. The DC output of each converter is connected in series in order to produce HVDC, as shown in Figure 2.1.

The initial proposal focused on the insulation and converter design of a PMSG with an ironless core [30, 31, 52, 53]. The segments are insulated from each other, and the insulating screens are clamped to the mid-point of the DC-link. This system has several envisioned benefits:

- The transformer in the nacelle of the wind turbine could be eliminated, reducing the top mass. This could be especially beneficial for Direct-Drive generators, as their large weight poses challenges for high-power offshore wind applications [43].
- The number of power conversion steps is reduced, possibly including the need of an offshore rectifier substation. This increases efficiency and reduces complexity and costs.
- By making the system modular, the maintenance and reliability of the offshore wind farm could be improved. This will be discussed in more detail in Section 2.2.

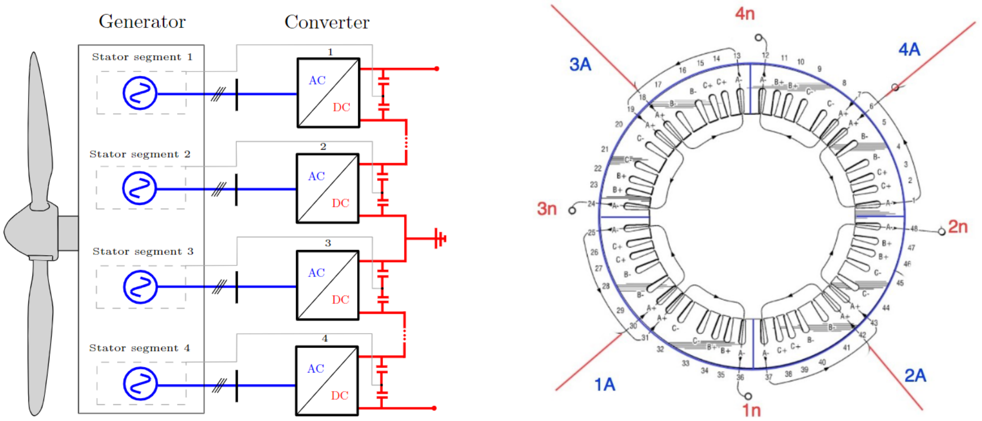

(a) The ModHVDC system layout

(b) A stator with four segments

Figure 2.1: The ModHVDC concept, in this case shown with 4 segments and 48 slots [47].

Recent research has studied variations on this design, using a conventional laminated iron core split into insulated segments. Both geared and direct drive versions of the machine have been studied [68], as well as different power converter configurations [25]. Segmentation has also been found to influence the power losses and force harmonics which occur in the generator, and it was concluded that this required a more detailed analysis [50]. Most recently, the thermal design of the generator has been studied. Since the magnetic insulation between the segments acts as a thermal barrier as well, cooling the machine poses challenges. To solve this, cooling in between the stator segments and the support frame has been proposed, but the structural aspects of this design remain to be analyzed [47].

2.2. Modularity and Fault tolerance

A modular system is a system that consists of multiple independent subsystems. The system can contain different subsystems or modules which each have their own function, or multiple similar modules. In both cases, the construction of the system can be simplified by producing modules separately and integrating them later, instead of producing the whole system at once. Furthermore, if modules are relatively simple to replace, the maintainability of the system is improved as well.

In electrical machines, modularity has been researched and implemented on various levels [1, 63]. On a functional level, power converters have been used in parallel, in order to reduce the power level of each individual converter. In the case one of these converters fails, it can be bypassed while the system continues to operate at a reduced capacity. This concept can be extended to using power converters for each individual phase, or each individual coil [49, 82]. This again creates the possibility of continuing operation with a reduced number of phases or coils.

Modularity can also be implemented on a physical level. In electrical machines, this can be achieved by splitting the stator into multiple segments, for which several methods have been proposed. Some focus mainly on manufacturability and standardization, and integrate the segment into a complete stator ring afterwards. This can be achieved by connecting E-cores or T-cores together, or by producing the teeth separately from the back iron [34, 62, 87]. Other designs include a dedicated power converter to each stator segment, as shown in Figure 2.2 [15, 63, 67]. In this case, each module can be considered as a standalone integrated electrical machine, operating independently.

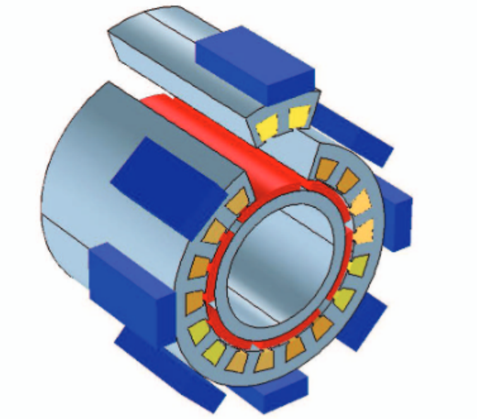

Figure 2.2: A segmented stator with dedicated converters for each segment. [63]

Making the generator of an offshore direct-drive wind turbine modular could be interesting due to the large and heavy generator structure, and the challenges of installation and maintenance at sea [63]. Ideally, one module can be repaired or replaced when its windings or converter fails, without the need to replace the entire machine. By reducing the downtime, the availability of the wind turbine can be increased.

Another method of increasing the availability of the wind turbine is by improving the fault tolerance of the system. A fault-tolerant system is capable of continuing operation after a fault has occurred in one of its components [58]. Using a modular stator can improve the fault tolerance by containing the fault in one segment. Using concentrated windings contributes to this as well, due to the low mutual inductance between phases [21]. This prevents a single-phase winding fault from affecting the other phases. By segmenting the stator, the mutual inductance between segments is even further reduced, improving the fault tolerance [46]. This holds especially in case a faulty module can be bypassed, and the generator can continue to operate with a reduced number of modules.

For high-voltage drivetrains without gearboxes, winding faults are one of the most important failure modes [58]. As maintenance is complex and costly for remote offshore wind farms, improving the fault tolerance of the stator can thus potentially be very beneficial. This however only holds if the failure rate of the system is not significantly increased. One way this could happen is by the increase of the amount of semiconductors in the system, which have a relatively high failure rate as well [58]. This is partially mitigated if the collector substation can be removed from the wind farm in the case of the ModHVDC system, as the high-power converters of the substation are replaced by more standard power electronics within the wind turbine, with a lower failure rate. The failure rate could also be increased if the structural integrity of the generator is compromised by segmenting the stator, which will be studied in this report.

2.3. Vibrations

The forces and vibrations in electrical machines have been widely studied. They are important in electrical machine design in general, and wind turbine generators in particular, for various reasons:

- Effects on the load: some of the force harmonics lead to pulsations in the output torque. This can cause speed deviations of the load of a motor, and a varying power output of a generator. For a geared wind turbine, this is especially relevant as it introduces additional loads on the gearbox [28, 70]
- Effects on noise: vibrations in the machine structure lead to airborne noise, which is mainly important if the vibrations occur at frequencies within the audible range [28]. For wind turbines, noise generated by the drivetrain is small compared to the noise coming from the wind turbine blades [55], and is irrelevant for offshore wind turbines.
- Effect on structural integrity: vibrations are an important cause of machine failures [70]. As offshore wind turbines are design to operate remotely for long periods of time, reducing the failure rate due to excessive vibrations will be important.

Vibrations and noise in electrical machines have several sources [28, 70]:

- Mechanical vibrations, in particular bearings and gearboxes
- Load effects, such as the fluctuating torque of the wind turbine blades due to the tower shadow effect
- Magnetostriction of the laminations in the stator and rotor core
- Unbalanced magnetic pull due to asymmetries in the air gap, caused by oval or misaligned shafts
- Electromagnetic vibrations due to the higher spatial and time harmonics in the stator and rotor magnetic fields

Segmenting the stator will mainly affect the last type of vibrations, both by changing the occurring harmonics as well as by changing the mechanical response of the generator. The other vibrations are considered outside the scope of this thesis.

3

Machine Design

During an initial study on the same machine, it was concluded that the design contained various issues [42]. The machine designed and analyzed in previous studies [50, 68] is significantly smaller than other 10 MW Direct Drive machines [57, 61] and was found to have a very high armature reaction leading to saturation. To obtain a more realistic model of the forces, the machine was redesigned, and is presented here in detail.

3.1. Initial sizing

First of all, a non-modular 10 MW Direct Drive PM machine is designed based on an analytical design procedure[33] and verified with numerical simulations in COMSOL as described in Chapter 6. In this case, all coils in each phase are assumed to be connected, leading to a very high voltage machine. The design parameters are given in Table 3.1.

Table 3.1: Design parameters of the ModHVDC machine

Nominal Power P	10 MW
Speed S	10 RPM
RMS line voltage V_{LL}	74 kV
RMS Phase voltage V_{ph}	42.8 kV
Topology	Inner Rotor PMSM
Winding configuration	Concentrated single-layer
Number of phases N_{ph}	3

While using this design procedure, two additional design limits were taken into account:

- A torque density limit $F_d = 30 - 60$ kN/m^2 for air-cooled machines [59]. The torque density relates the available power to the size of the machine through the relation $P = 2\omega_m V_r F_d$, with V_r as the rotor volume.
- A maximal thermal loading of $K_s J_s = 1000 - 2000$ A^2/mm^2/cm for air-cooled machines [78]. K_s represents the linear current density, and J_s the slot current density.

Using these limits, an air gap diameter in the range of 10 m is obtained, which is in agreement with similar 10 MW Direct Drive Permanent Magnet Synchronous Generators [57] including those designed for the DTU Reference Wind Turbine [5, 61].

3.2. Concentrated Windings

Different from other 10 MW DD generators, this machine will use concentrated single-layer windings in order to enable modularity. Fractional-slot concentrated windings (FSCW) have less than one slot per pole per phase ($q < 1$) which reduces the number of slots required.

3.2.1. Advantages and disadvantages

Concentrated windings, also called modular windings, are often used in large multipole machines [1], as they have various advantages. These include a high slot fill factor leading to a higher power density, especially when open slots are used [71], short end windings and an improved fault tolerance, as was discussed in Section 2.2 [21, 46]. In case the slot/pole combination is chosen well, a low cogging torque can be obtained [21, 71] while achieving a high main winding factor [12]. The 12 slot/10 pole base winding, with $q = 0.4$, is often used [1, 12] due to its high main winding factor of 0.966. A multiple of this base winding was also selected in earlier designs of the ModHVDC machine [68].

Concentrated windings can be single-layer, with a coil found around every alternating tooth, or double-layer, with a coil wound around every tooth. As the latter, shown in Figure 3.1c, is consecutive, this pattern is infeasible for a segmented stator, and thus a single-layer concentrated winding as shown in Figure 3.1d is used. In this configuration, the coil pitch is twice the slot pitch. The main disadvantage of this single-layer configuration is the addition of several strong harmonics in the winding MMF including low subharmonics, making the magnetic field non-sinusoidal [12, 21]. This leads to high rotor losses and strong vibrations [1, 20, 71] as was also observed in earlier studies on the ModHVDC machine [50]. Analyzing these additional harmonics will be one of the key aspects of this thesis.

Another downside of FSCW is the strong magnetic fields caused by the windings, especially when a low number of slots is used [57]. In the original design, a very strong armature reaction was observed, causing saturation in the teeth and distortion in the output voltage. To reduce this, while keeping the design comparable to earlier studies, the number of slots and poles has been doubled to 384 and 320 respectively. Furthermore, to reduce rotor losses, segmented permanent magnets are used [50].

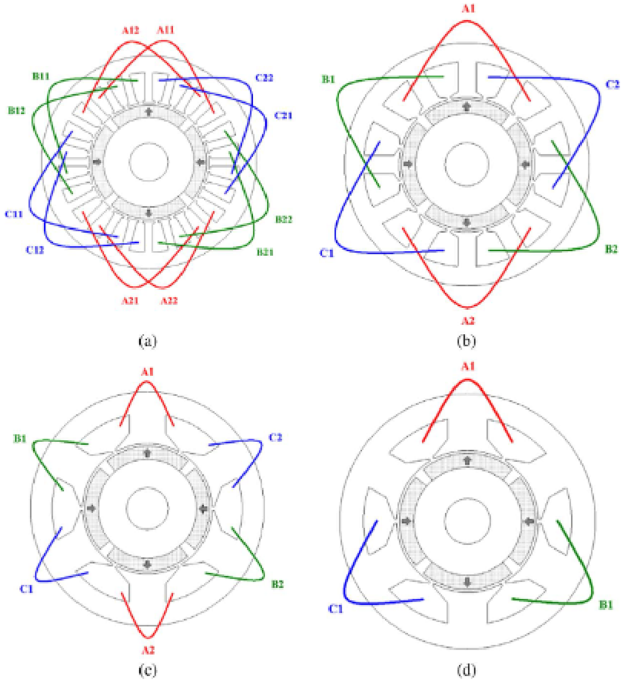

(a) (b) (c) (d)

Figure 3.1: Different winding configurations: a) distributed, overlapping b) concentrated, overlapping c) non-overlapping, double-layer d) non-overlapping, single-layer [21]

3.2.2. Winding factors

A challenge in modeling machines with concentrated windings lies in finding the winding factors relating to the spatial harmonics [22, 79]. Several closed-form formulas exist [65, 93] but the most certain method of finding the winding factors is by analyzing the winding function. This represents a turn-counting function along the machine circumference, centered around zero. For machines with a large number of slots and poles, the periodicity of the machine can be used, also referred to as the number of machine sections F_1 [12, 45]. The periodicity is the greatest common denominator of the number of slots N_s and pole pairs p, and represents the number of parts that can operate as a separate machine.

$$F_1 = \text{gcd}\left(N_s, p\right) \tag{3.1}$$

For this specific machine, the slot/pole combination is chosen in such a way that it operates as F_1 individual 12 slot/10 pole machines, or in other words, $N_s/F_1 = 12$ and $2p/F_1 = 10$. First, the winding factors k_w of one individual section can be obtained. The spatial harmonics v of the winding function are obtained from its Fourier transform, and divided by the spatial harmonics of a concentrated full pitch base winding:

$$k_{wv,F_1} = \frac{N_v}{N_{v,base}} \tag{3.2}$$

The base winding with N_t turns in series has a square winding function resulting in

$$N_{v,base} = (-1)^{\frac{v-1}{2}} \frac{2}{v\pi} N_t \qquad \text{for } v = 1, 3, 5, ... \tag{3.3}$$

Applying Equation 3.2 to a concentrated winding gives

$$k_{wv,F_1} = \sin\left(\frac{v\pi}{N_s/F_1}\right) \tag{3.4}$$

For a machine with multiple sections, the winding pattern repeats F_1 times. The fundamental harmonic $v = 1$ in one section results in a $v = F_1$ harmonic in the whole machine, so harmonics will occur at multiples of F_1 [45]. Taking into account the fact that the third harmonic is canceled out in balanced, three-phase systems, the winding factors for the whole machine are given by

$$k_{wv} = \sin\left(\frac{v\beta_s}{2}\right) \qquad \text{for } v = 1 \times F_1,\ 5 \times F_1,\ 7 \times F_1, ... \tag{3.5}$$

for a slot pitch of $\beta_s = 2\pi/N_s$. This agrees with results found in literature [17, 93] in which Equation 3.5 reflects the pitch factor, and the distribution factor is 1. The same result could be obtained using the star of slots method [11]. Figure 3.2 shows the winding factors for this machine. As $p = 5 \times F_1$, this is the main harmonic, and the figure shows a main winding factor of 0.966.

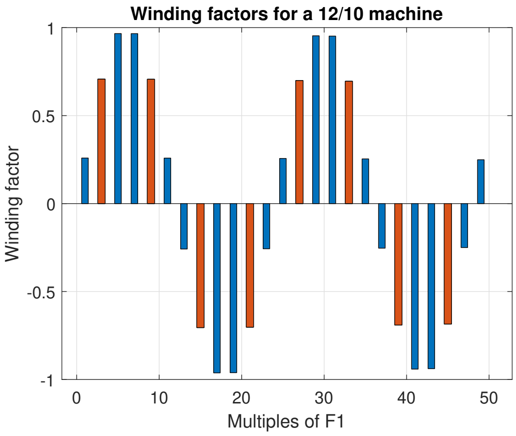

Figure 3.2: Winding factors in a machine with a base winding of 12 slots/ 10 poles. Multiples of 3, which cancel out in a balanced three-phase machine, are depicted in red.

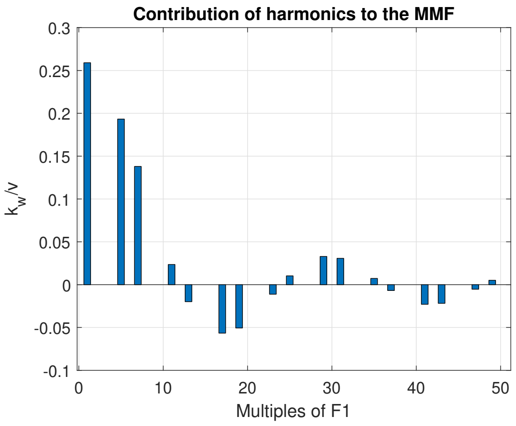

Figure 3.3: The contribution of the occurring harmonics to the MMF, which is proportional to k_{wv}/v. Multiples of 3 have been removed.

The MMF resulting from concentrated, single-layer windings adds an additional complexity, as it generates both forward and backward rotating magnetic fields [45]. The rotational direction of harmonic v can be determined from the rotation factor $k_{\tau v}$, given by Equation 3.6 [85]. In this formula, s_b represents the number of phase belts per phase in one section. In the used winding pattern, $s_b = 2$ as each phase has two coils per section, which are not neighboring to each other.

$$k_{\tau v} = \frac{\sin\left(\pi v/s_b\right)}{m \sin\left(\pi v/s_b N_{ph}\right)} \tag{3.6}$$

Harmonics for which holds that $k_{\tau(v-1)} = 1$ rotate forwards, while harmonics with $k_{\tau(v+1)} = 1$ rotate backwards. For this specific winding pattern, this means

Forward rotating: $(6n+1)F_1$ for $n = 0, 1, 2, 3...$
Backward rotating: $(6n-1)F_1$ for $n = 1, 2, 3...$

The magnitude of the MMF resulting from an individual harmonic v is proportional to k_{wv}/v, which is shown in Figure 3.3. This shows the importance of the subharmonic at $v = F_1$ for a single-layer concentrated winding, which is even stronger than the working harmonic at $v = 5 \times F_1$, as is also found in literature [12, 17]. Furthermore, based on Equation 3.6, it is found that the first and fifth harmonic rotate in opposite direction [13].

3.3. Phasor diagram

In the previous design, the power factor of the machine has not been considered. In order to ensure the machine is capable of producing 10 MW of active power, the power factor is taken into account in the design when calculating the required phase current. The machine is analyzed for the case that all current is supplied in the quadrature axis of the machine, and none in the direct axis. This reduces the copper losses in the armature winding but requires an overdesigned power converter as the terminal output will have a relatively low power factor [59].

The phasor diagram for the machine in case all current is applied in the q-axis is shown in Figure 3.4. The phase current i can be seen to lead the terminal voltage U_{ph}. Neglecting the resistive losses, the power factor of the terminal can be calculated using the phase inductance $L_{ph} = L_s + L_\sigma$ and the induced voltage E_p by

$$pf = \cos\varphi = \cos\left(\arctan\frac{\omega_e L_{ph} i}{E_p}\right) \tag{3.7}$$

This equals approximately 0.85, which is similar to other large Direct-Drive machines [45]. Different load cases, with positive or negative currents in the d-axis, will lead to different levels of vibrations [73].

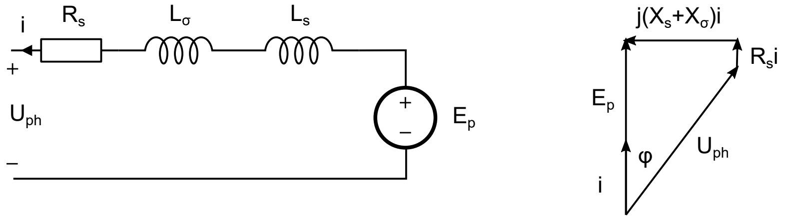

Figure 3.4: The phasor diagram of the machine when all current is applied in the q-axis.

3.4. Obtained model

Summarizing the discussion above, compared to the earlier machine model, the current machine has the following properties:

- An increased diameter, to take into account torque density and thermal loading limits
- Twice the number of poles and slots to reduce the armature reaction
- A higher phase current, as the power factor is now taken into account when calculating the active power.

The obtained machine is now similar to other 10 MW DD generators found in literature [57, 61] and its characteristics are shown in Table 3.2. The geometric parameters used in this thesis are explained in Figure 3.5. The model is not optimized in terms of costs, size or weight, but should be considered as a first approximation.

Table 3.2: Machine parameters

Design goals		
	Full machine	Per segment
Electrical Power P	10 MW	625 kW
RMS Phase voltage V_{ph}	42.8 kV	2.67 kV
Rotation speed S	10 RPM	
Max magnetic flux in the iron B_{max}	1.5 T	
Max current density in the slots J_{max}	3 A/mm^2	
Machine layout		
Number of slots N_s	384	24
Number of coils N_c	192	12
Number of pole pairs p	160	10
Number of segments N_{seg}	16	
Slots per pole per phase q	0.4	
Geometric parameters		
Outer rotor radius R_{ro}	4.85 m	
Inner stator radius R_{si}	4.89 m	
Outer stator radius R_{so}	5.0 m	
Mean yoke radius R_y	4.977 m	
Active length L	1.7 m	
Air gap g	10 mm	
Magnet length l_m	30 mm	
Lamination stacking factor k_{st}	0.8	
Conductor packing factor k_{cp}	0.76	
Magnet fraction α_m	0.7	
Back iron thickness h_{bi}	47 mm	
Tooth width w_{th}	39 mm	
Average slot width w_s	41 mm	
Slot depth d_s	63 mm	
Gap between segments w_{gap}	10 mm	
Pole pitch β_p	0.0196 rad	
Slot pitch β_s	0.0164 rad	
Slot opening pitch β_{so}	0.0084 rad	
Magnetic circuit parameters		
PM remanence B_r	1.2 T	
Permeance coefficient P_c	3.64	
Carter coefficient k_c	1.1	
Air gap flux density B_g	0.69 T	
RMS Air gap flux ϕ_g	67 mWb	
Electric parameters		
Electrical frequency f_e	26.7 Hz	
Main winding factor k_w	0.966	
Number of turns per slot n_s	61	
RMS coil current i	92.4 A	
Slot current I_s	5.6 kA	
Coil resistance (slot + end winding) R_{coil}	0.165 + 0.025 = 0.19 Ω	
Phase resistance R_{ph}	12.1 Ω	0.76 Ω
Phase inductance (nominal + leakage) L_{ph}	1.75 + 0.02 = 1.77 H	0.11 H
Output power factor cos φ	0.85	
Operational parameters		
Equivalent torque T_e	9.55 MNm	
Slot current density J_c	2.8 A/mm^2	
Force density F_d	37 kN/m^2	
Thermal loading $K_s J$	1906 A^2/mm^2/cm	
Frame parameters		
Frame thickness h_f	5 mm	
Frame length L_f	2.0 m	

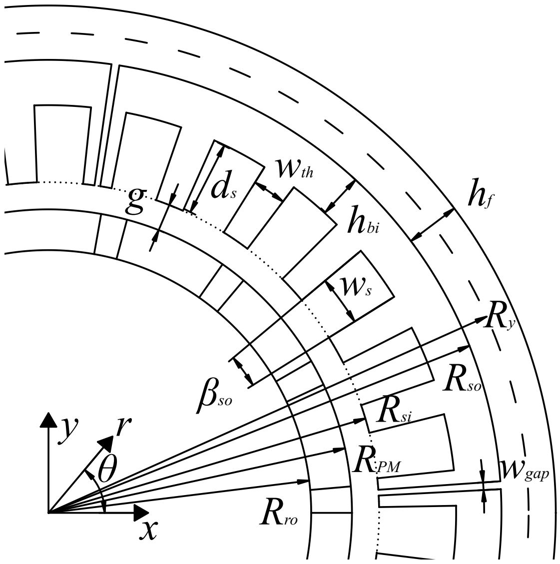

Figure 3.5: Layout of the electrical machine with an explanation of the geometric parameters.

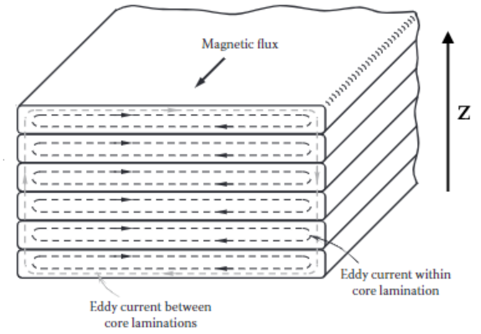

Figure 3.6: The use of laminations in the z-direction, adapted from [70]

The cores of the rotor and stator are made of laminations, insulated, thin sheets of metal stacked in the z-direction, to reduce eddy current losses as shown in Figure 3.6 [70]. The exact electromagnetic and mechanical properties of these laminations are a source of uncertainty when modeling electrical machines, as will be discussed in Section 5.2.1.

The winding pattern for the single-layered concentrated winding is shown in Table 3.3, which is repeated 32 times.

Table 3.3: Winding pattern of the 384 slot - 320 pole machine.

Slot	1	2	3	4	5	6	7	8	9	10	11	12
Winding	A	-A	-B	B	C	-C	-A	A	B	-B	-C	C

Using these parameters, an estimate of the performance of the machine can be made. 3 types of losses are included:

- Ohmic losses, based on I^2R.
- Core losses, based on the iron weight (density times volume) and a core loss density of Γ_s = 1.0 W/kg. This is low due to the low rotational speed and the resulting electrical frequency.
- Stray losses, assumed to be 2% of the total power.

This results in the losses and efficiency as shown in Table 3.4. For a mechanical power of 10 MW, the acquired efficiency results in an available electrical power of 9.5 MW.

Table 3.4: Performance parameters

Ohmic losses P_r	309 kW
Core losses P_{cl}	24.8 kW
Stray losses P_s	200 kW
Efficiency η	95 %

3.5. Incorporating modularity

In the ModHVDC design, physical modularity is used by splitting the stator is segments. As shown in Figure 3.1d, non-overlapping single-layer windings have teeth without any windings attached to them, which can be used to segment the stator in the middle of a tooth. In order to use a 3-phase converter to generate a DC output from each module, a stator segment needs to contain a multiple of 6 slots. For this design, 16 segments with 24 slots each will be used, which means each segment contains two machine sections. This means each segment produces 1/16$^{\text{th}}$ of the total power, at 1/16$^{\text{th}}$ of the nominal voltage level, as shown in Table 3.2.

All segments will need to be insulated from each other, as well as from a potential support structure, in order to prevent short-circuits. Due to the high voltage, this will requires several millimeters of insulation material around the stator segments. In this thesis, the details of insulation will not be considered, but the gaps between the segments will simply be considered as insulated boundaries. A segment gap width $w_{gap} = 10$ mm is assumed.

3.5.1. Mechanical design

These segments need to be constrained in the wind turbine to create a full stator ring, while also maintaining the option of replacing one module after it has failed. The easiest way to make the segments removable is by using an external frame. Two different attachment methods will be considered in this thesis. The first is an interference fit, which consists of an external ring with fins on the inner radius. The inner radius of the frame will have a small overlap with the outer radius of the stator core segments, the interference δ. The segments will be pressed into the frame, creating a normal force due to the required deformation, and are held in position by the resulting friction. Insertion happens by means of a high compression force, a press fit, by cooling the segment in order to create a shrink fit, or by a locking mechanism that expands after insertion [70]. This method has been used in small scale modular machines,[46] as shown in Figure 3.7. For this design, there is direct contact between the segments and frame, which means a layer of insulation material is required between the two components.

The second method consists of attaching the segments to the frame with beams. This makes installation easier, and allows for an air gap between the segments and the frame, which can be used for electric insulation and cooling, discussed in Section 3.6. This design has been proposed for segmented stators with E-cores as well, as shown in Figure 3.8 [67]. The downside of this design is the fact that the frame will not provide as much stiffness to the stator core as a press fit would do. The feasibility of this design is studied in this thesis.

The support frame could be made from metal or a reinforced composite. For this thesis, a simple steel cylinder is assumed as frame, with a thickness close to the stator core back iron, 5 mm. The length is chosen to be 2 m, to allow space for the end windings and the attachment to the wind turbine nacelle. While this design is arbitrary, Chapter 5 will provide an analysis method that can be used to study other possible designs as well. Sketches of the considered designs are shown in Figure 3.9 and 3.10.

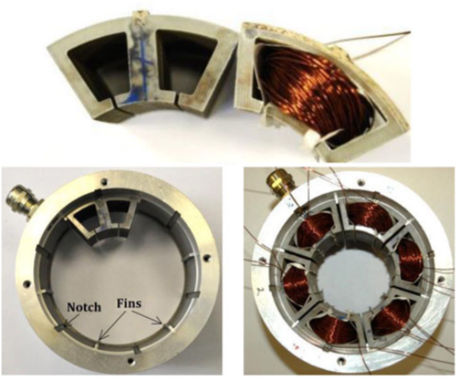

Figure 3.7: Example of a small-scale modular machine using a press fit [46].

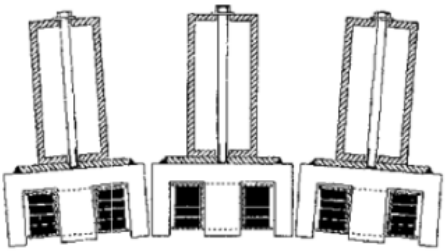

Figure 3.8: Example of individual support structures for each segment [67].

3.5.2. Effect on electromagnetic fields

The insulated gaps between the segments will also change the magnetic flux distribution in the stator core by acting as flux barriers, which could influence the winding factors discussed in Section 3.2. If a flux barrier is added in every second tooth, this can significantly reduce the subharmonic $v = 1$

for 12 slot/10 pole machines [17, 18, 20]. The effect of flux barriers and segmentation has primarily been studied for gaps at every tooth [87], every second tooth [20], E-cores [1] and U-cores [34], while the effect of larger segments is not well known. For this machine, 16 flux barriers are added by the 16 segments with 24 teeth each. As the spatial orders of the magnetic flux density are multiples of $F_1 = 32$ due to the periodicity of the machine, the segment gaps are not expected to block any low spatial orders, so the impact on the winding factors will be limited.

Segmenting the stator also influences the mutual inductance of the phases. If flux barriers are added between each coil, the mutual inductance becomes close to zero, leading to an increased fault tolerance [46]. For this machine, the effect of the segment gaps on the mutual inductance is expected to be limited, as the use of concentrated windings already leads to a low mutual inductance and the phases within one segment are still physically connected. This will be studied numerically in Chapter 6.

3.6. Cooling

The insulation around the segments acts as a thermal barrier as well. Together with the high rotor losses caused by the use of concentrated windings, this can lead to challenges in the thermal design of the ModHVDC generator. An earlier study suggested that air cooling through ducts in the stator core would be insufficient, and proposed additional cooling in between the stator segments and the support frame [47]. This would require an air gap of 2 cm between these two components, as well as an insulated or non-conducting mounting structure. In another study, the use of segmented permanent magnets was proposed to lower the rotor losses [50]. If the expected loss reduction is correct, this would invalidate the requirement of having cooling in between the segments and frame, and make the press fit design more feasible.

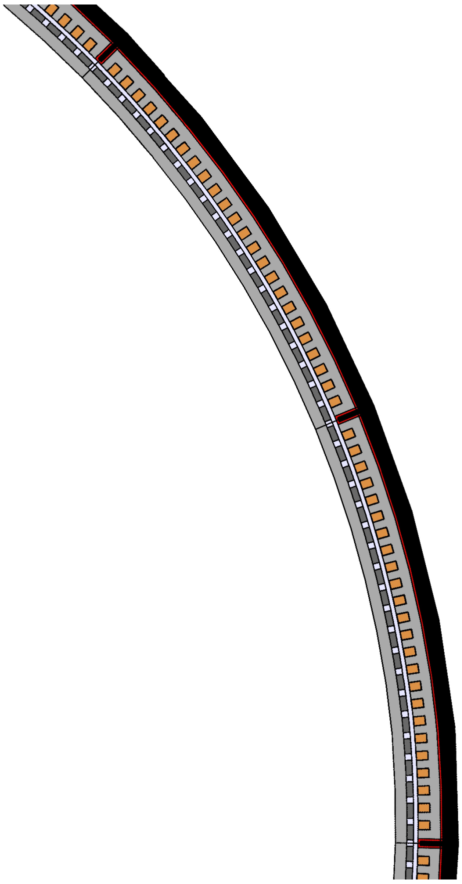

Figure 3.9: Design 1 (not to scale): the segments are pressed into a frame, and are held in place by friction. The red lines indicate the required insulation. Cooling happens by ducts through the stator core (not shown)

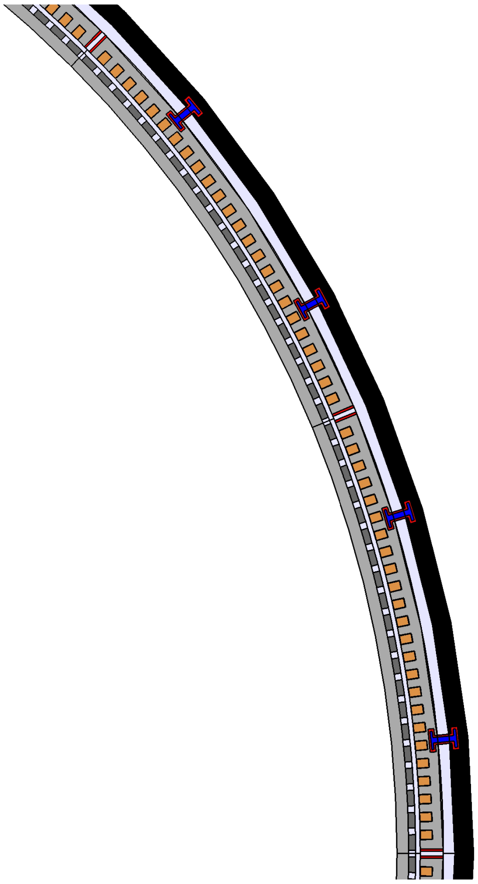

Figure 3.10: Design 2 (not to scale): the segments are held in position by beams connected to the frame. There is an air gap in between the core and frame, which insulates the components and allows for cooling

4

Analytical electromagnetic model

This chapter describes an analytical model to calculate the forces occurring in the Modular HVDC generator. Forces can be calculated either using an energy-based method [41] or using the magnetic flux density distribution together with Maxwell's stress tensor. In this report, the latter is used, based on the method described in *Noise in Polyphase Electric Motors* by J.F. Gieras [28] and extended with the analytical magnetic field calculations from *Zhu et al.* [90–95], the implementation of the complex relative permeance described by *Žarko et al.* [96], and several other papers referred to in this chapter.

4.1. Method outline

The method is summarized in Figure 4.1. The resulting forces are used as input to the mechanical model, described in the next chapter, to analyze the resulting vibrations and deformations. Often, these vibrations are used to calculate the acoustic noise generated by the machine, shown in the figure as well, but this step is not considered in this report.

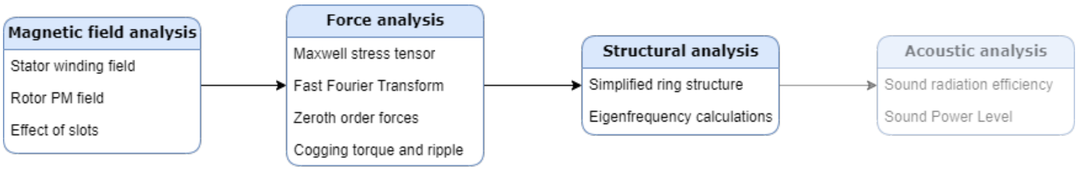

Figure 4.1: The analytical method used in this report

4.1.1. Simplifications

Regarding the overall approach, the main simplification that is made is the decoupling of the electromagnetic analysis of the fields and the deformation of the stator and rotor structure. In reality, this deformation will result in changes in the magnetic fields due to the displacement of the permanent magnets and the windings. This effect could be significant due to the positive feedback loop of attractive forces coming from two (electro)magnets: as they attract each other, the distance between them decreases, increasing the attractive force and thus resulting in negative stiffness [41]. However, the impact of this coupling is generally limited, as the deformation is small compared to the air gap width in Permanent Magnet machines. This means the magnetic fields and forces are calculated assuming a rigid structure.

To calculate the magnetic fields analytically, the following assumptions are made:

- All stator segments are assumed to be identical, including the currents applied to them, and independent from each other.
- A 2D analysis is performed, assuming the magnetic fields are constant along the active length of the machine.
- Losses are neglected

- The permanent magnets are radially magnetized. Due to the large diameter of the machine, the effect of parallel-magnetized PMs is limited.
- Saturation is neglected, meaning the magnetic fields in the air gap are a linear superposition of the stator and rotor fields.
- The stator and rotor are assumed to be perfectly aligned and centered
- The magnetic fields and forces are calculated close to the stator, as the vibration of the stator segments is of main interest to this thesis. The provided method can be adapted to calculate the forces on the rotor as well.
- The rotor speed is assumed to be the rated speed of 10 RPM. Lower rotational speeds will reduce the frequency at which the force harmonics occur.

4.2. Sources of force harmonics

The electromagnetic fields in the machine cause vibrations primarily due to harmonics in the magnetic flux density of the stator and rotor. These harmonics are caused by: [28]

- The interaction between permanent magnets and the stator slots
- Eccentricity of the rotor due to shaft misalignment or deformation of the rotor structure
- Magnetic saturation of the stator core
- Time harmonics in the coil currents for converter-connected machines. Especially the switching frequency of the converter is an important factor [10]
- In the case of a segmented stator, the gaps between the segments will change the flux density pattern in the stator and air gap, potentially leading to additional forces

These harmonics in the air gap flux density will interact with each other to create a wide range of harmonics at different spatial orders and frequencies in the radial and tangential forces occurring in the machine. The following chapter will break down the different harmonics that occur and describe an analytical model to analyze them.

4.3. Forces in Electrical Machines

The general form of the radial and tangential force density in a synchronous machine is shown in Equations 4.1 and 4.2, in which θ and t represent the angular position and time, ω_r is the mechanical angular velocity, and m and k_f represent the spatial and temporal harmonic orders, respectively [28, 71]. The term $\omega_r t$ can also be interpreted as the mechanical rotor position θ_r.

$$f_r(\theta, t) = \sum_m \sum_n f_{r(m,k)} \cos\left(m\theta - k_f \omega_r t\right) \tag{4.1}$$

$$f_t(\theta, t) = \sum_m \sum_n f_{t(m,k)} \sin\left(m\theta - k_f \omega_r t\right) \tag{4.2}$$

This means the radial and tangential forces are a superposition of various spatial orders at different frequencies, which are multiples of the mechanical frequency. The spatial orders are easiest to visualize for the radial forces, as shown in Figure 4.2. Three different types of forces can be observed:

- $m = 0$, the breathing mode: the radial pressure is constant along the circumference, but could vary in time. This creates a pulsating force on the stator
- $m = 1$, the beam bending mode: the radial pressure is higher on one side. This is usually caused by eccentricity, and could be static (located on a fixed position on the stator) or dynamic (rotating along with the rotor).
- $m > 2$, the higher orders: the radial pressure varies along the circumference, with m peaks and troughs along the circumference of the machine. For a force order with a frequency ω, a fixed point on the stator encounters a force varying with this frequency. This means the m^{th} force harmonic can be imagined as rotating around the machine axis with a angular velocity of ω/m.

The tangential force has similar spatial orders, of which the zeroth order can be interpreted as the torque of the machine. The goal of the following analysis is to determine the relevant time and space harmonics occurring in the ModHVDC machine. These harmonics will be those with a relatively large amplitude, a low spatial order, and a frequency close to one of eigenfrequencies of the structure.

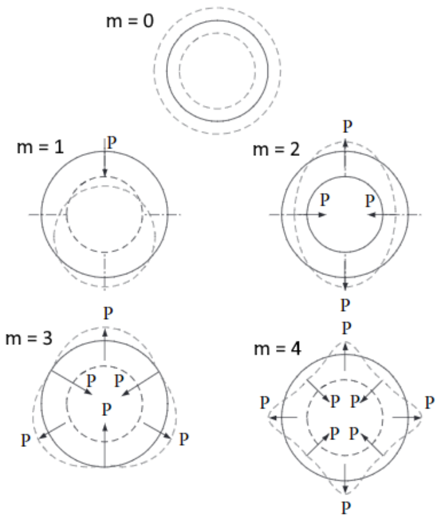

Figure 4.2: Visualization of the spatial radial orders [28].

4.4. Force calculations

The forces resulting from the magnetic fields in an electrical machine can be determined either using the method of virtual work, or using the Maxwell stress tensor. While the method of virtual work can provide a way to incorporate the effects of magneto-mechanical coupling [41], the simplified forms of the Maxwell stress tensor are far more often applied [8, 28, 71, 93] as they provide a clear insight in the way the design parameters of the machine result in the occurrence of spatial harmonics. The downside of this method is its inaccuracy close to singularities, especially if the spatial resolution is low [41]. To mitigate this problem, the magnetic field is calculated at a large number of values for θ [2].

The dyadic of the Maxwell stress tensor is given by Equation 4.3, from which the force density is calculated using Equation 4.4. The derivation of the Maxwell stress tensor is provided in Appendix A.

$$\overleftrightarrow{\boldsymbol{\sigma}} = \epsilon_0 \mathbf{E} \otimes \mathbf{E} + \frac{1}{\mu_0} \mathbf{B} \otimes \mathbf{B} - \frac{\epsilon_0 E^2 + \frac{1}{\mu_0} B^2}{2} \overleftrightarrow{\boldsymbol{I}} \tag{4.3}$$

$$\nabla \cdot \overleftrightarrow{\boldsymbol{\sigma}} = \mathbf{f} + \epsilon_0 \mu_0 \frac{\partial \mathbf{S}}{\partial t} \tag{4.4}$$

As explained at the end of Appendix A, by neglecting the electric field and the derivative of the Poynting vector, the force density equations in radial coordinates become:

$$f_r = \frac{1}{2\mu_0} \left(B_r^2 - B_t^2 \right) = f_{rr} - f_{rt} \tag{4.5}$$

$$f_t = \frac{1}{\mu_0} B_r B_t \tag{4.6}$$

An important conclusion is that radial and tangential forces are both dependent on the radial as well as the tangential component of the flux density in the air gap. In most machines the tangential flux density is negligible compared to the radial flux density due to the high magnetic permeability of the stator core, causing the magnetic flux lines to be nearly perpendicular to the stator teeth [28]. In this case, the radial force equation could be simplified by neglecting the tangential flux density. However, for large machines with open slots, the flux lines have a significant tangential component perpendicular to the tooth wall and can thus not be neglected [77].

The flux density is often written as a complex value $B = B_r + jB_t$. In that case, the complex stress can be written as [8]

$$f = f_r + jf_t = \frac{1}{2\mu_0} B^2 \tag{4.7}$$

4.4.1. Interactions between harmonics

The goal of the following sections is to find which spatial force orders occur in the machine under no-load and loaded conditions. The Maxwell stress tensor shows that the forces are calculated as the multiplication of two flux densities, and as will be shown below, the magnetic flux density is often given as an infinite sum of harmonics. To understand how flux density harmonics create force harmonics, it is useful to look at the general form of the product of two cosine series [19, 72].

For $B_1 = \sum\limits_{k_1=1,2,3...} b_{k_1} \cos\left(k_1\theta + \omega_{k_1}t\right)$ and $B_2 = \sum\limits_{k_2=1,2,3...} b_{k_2} \cos\left(k_2\theta + \omega_{k_2}t\right)$, their product equals

$$\begin{aligned} B_1B_2 &= \left(\sum_{k_1=1,2,3...} b_{k_1} \cos\left(k_1\theta + \omega_{k_1}t\right)\right) \times \left(\sum_{k_2=1,2,3...} b_{k_2} \cos\left(k_2\theta + \omega_{k_2}t\right)\right) \\ &= \sum_{k_1=1,2,3...}\sum_{k_2=1,2,3...} b_{k_1}b_{k_2} \cos\left(k_1\theta + \omega_{k_1}t\right)\cos\left(k_2\theta + \omega_{k_2}t\right) \\ &= \sum_{k_1=1,2,3...}\sum_{k_2=1,2,3...} \frac{b_{k_1}b_{k_2}}{2}\left[\cos\left((k_1-k_2)\theta + (\omega_{k_1}-\omega_{k_2})t\right) + \cos\left((k_1+k_2)\theta + (\omega_{k_1}+\omega_{k_2})t\right)\right] \\ &= \sum_{\omega_n}\sum_{m=0,1,2,3...} f_{mn}\cos\left(m\theta + \omega_n t\right) \qquad \text{with} \quad f_{mn} = \sum_{\substack{|k_1\pm k_2|=m \\ |\omega_{k_1}\pm\omega_{k_2}|=\omega_n}} \frac{b_{k_1}b_{k_2}}{2} \end{aligned} \tag{4.8}$$

in which use was made of $2\cos\alpha\cos\beta = \cos(\alpha-\beta) + \cos(\alpha+\beta)$ and $\cos\alpha = \cos(-\alpha)$.

This means a force harmonic m is generated by the sum of all pairs of flux density harmonics for which hold that $|k_1 \pm k_2| = m$. The frequency of these harmonics, ω_n, results from the sum or difference of the frequencies of the interacting flux harmonics. Three other important observations are made:

- For two flux density harmonics with the same order $k_1 = k_2$, the zeroth force order $m = 0$ with amplitude f_0 is produced. This results in a constant pressure if $\omega_{k_1} = \omega_{k_2}$, and thus does not contribute to vibrations or noise [28]. If $\omega_{k_1} \neq \omega_{k_2}$, a time-varying zeroth order is produced, as will be discussed in Section 4.6.1.
- In the common case that B_1 and B_2 only have odd harmonics ($k = 1, 3, 5...$), $|k_1 \pm k_2|$ is always even and the force only has harmonics at $2k$.
- The same spatial order can in theory occur at different frequencies. However, as will be shown below, only a few time frequencies are usually of interest.

4.5. Magnetic fields in PM machines

In the following sections, the analytical equations for the magnetic fields will be described. First, the rotor and stator fields are analyzed while ignoring the effects of the slots. Afterwards, the effect of the slots will be accounted for by considering the relative permeance due to the slots.

4.5.1. Magnetic fields from the permanent magnets

The magnetic flux density due to the permanent magnets on the rotor have a radial and a tangential component, which in complex notation is expressed as [8]

$$B^{PM}_{slotless} = B^{PM}_{r,slotless} + jB^{PM}_{t,slotless} \tag{4.9}$$

The radial and tangential components are given by Fourier series: [92–94]

$$B^{PM}_{r,slotless}(r,\theta) = \sum_{\mu=1,3,5,...}^{\infty} K_B(\mu) f_{Br}(r) \cos\left(\mu p(\theta - \omega_r t)\right) \tag{4.10}$$

$$B^{PM}_{t,slotless}(r,\theta) = \sum_{\mu=1,3,5,...}^{\infty} K_B(\mu) f_{Bt}(r) \sin\left(\mu p(\theta - \omega_r t)\right) \tag{4.11}$$

with

$$K_B(\mu) = \frac{\mu_0 M_\mu}{\mu_r}\frac{\mu p}{(\mu p)^2-1}\left(\frac{\mu p - 1 + 2\left(\frac{R_{ro}}{R_{PM}}\right)^{\mu p+1} - (\mu p+1)\left(\frac{R_{ro}}{R_{PM}}\right)^{2\mu p}}{\frac{\mu_r+1}{\mu_r}\left[1-\left(\frac{R_{ro}}{R_{si}}\right)^{2\mu p}\right] - \frac{\mu_r-1}{\mu_r}\left[\left(\frac{R_{PM}}{R_{si}}\right)^{2\mu p} - \left(\frac{R_{ro}}{R_{PM}}\right)^{2\mu p}\right]}\right) \tag{4.12}$$

$$M_\mu = 2\frac{B_r}{\mu_0}\alpha_m \frac{\sin\frac{\mu\pi\alpha_m}{2}}{\frac{\mu\pi\alpha_m}{2}} \tag{4.13}$$

$$f_{Br}(r) = \left(\frac{r}{R_{si}}\right)^{\mu p-1}\left(\frac{R_{PM}}{R_{si}}\right)^{\mu p+1} + \left(\frac{R_{PM}}{r}\right)^{\mu p+1} \tag{4.14}$$

$$f_{Bt}(r) = -\left(\frac{r}{R_{si}}\right)^{\mu p-1}\left(\frac{R_{PM}}{R_{si}}\right)^{\mu p+1} + \left(\frac{R_{PM}}{r}\right)^{\mu p+1} \tag{4.15}$$

For geometric parameter K_B, a radial magnetization of M_μ is assumed. Due to the large radius of the considered machine, the difference with parallel magnetization can be assumed to be small. For the forces acting on the stator, the magnetic fields at $r = R_{si}$ are of interest. In this case, the latter two equations reduce to

$$f_{Br}(R_{si}) = 2\left(\frac{R_{PM}}{R_{si}}\right)^{\mu p+1} \tag{4.16}$$

$$f_{Bt}(R_{si}) = 0 \tag{4.17}$$

The tangential component due to the rotor is zero at the inner radius of the slotless stator, because the flux lines are parallel to the stator iron. In a slotted stator, the rotor field will result in a tangential component, as discussed below. Above equations show that the μ^{th} harmonic of the radial flux density is given by

$$B_{m\mu}\cos\left(\mu p(\theta - \omega_r t)\right) \tag{4.18}$$

which has

- a magnitude $B_{m\mu}$, defined by $K_B(\mu) f_{Br}$
- a spatial order μp with $\mu = 1, 3, 5, ...$
- a frequency $\mu p \omega_r$ with $\mu = 1, 3, 5, ...$

and rotates around the machine with a rotating frequency ω_r. Figure 4.3 shows $B^{PM}_{r,slotless}(R_{si}, \theta)$ for this machine as function of θ along the circumference of one segment.

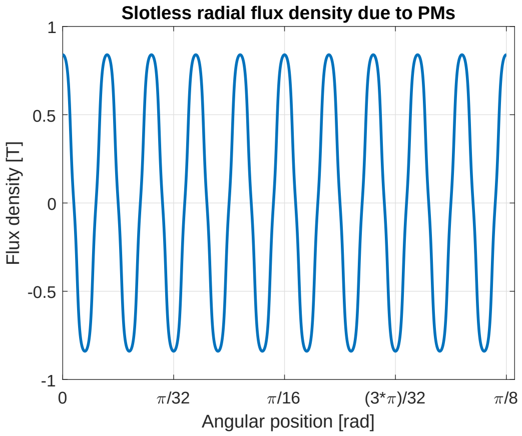

Figure 4.3: Radial magnetic flux density due to permanent magnets along one slotless stator segment at t = 0 s*

4.5.2. Magnetic fields from the windings

For the first part of the analysis, sinusoidal currents are assumed, with only the fundamental current waveform at frequency $\omega_e = p\omega_r$ being present. As discussed in Section 3.3, all current is assumed to be applied in the q-axis, giving

$$\begin{aligned} i_d &= 0 \text{ A} \\ i_q &= -\sqrt{2} i_{RMS} = I_1 \\ i_0 &= 0 \text{ A} \end{aligned} \tag{4.19}$$

The phase currents can then be calculated from the inverse Park transform [35] by aligning the direct axis to the axis of phase a [95]:

$$\begin{bmatrix} i_a \\ i_b \\ i_c \end{bmatrix} = \begin{bmatrix} \cos(p\theta) & -\sin(p\theta) & 1 \\ \cos(p\theta - 2\pi/3) & -\sin(p\theta - 2\pi/3) & 1 \\ \cos(p\theta + 2\pi/3) & -\sin(p\theta + 2\pi/3) & 1 \end{bmatrix} \begin{bmatrix} i_d \\ i_q \\ i_0 \end{bmatrix} \tag{4.20}$$

For a balanced 3-phase system, the phase currents are given by Equation 4.21. In converter-connected machines, the currents will contain time harmonics, which will influence the forces occurring in the machine. This is considered later in Section 4.8.

$$\begin{aligned} i_a &= I_1 \sin(\omega_e t) \\ i_b &= I_1 \sin(\omega_e t - \frac{2\pi}{3}) \\ i_c &= I_1 \sin(\omega_e t + \frac{2\pi}{3}) \end{aligned} \tag{4.21}$$

The currents in the stator coils create a magnetic field as well, the armature reaction. By modeling the currents in the slots as distributed current sheets in the stator slot openings, the resulting flux density is given by [90, 93]

$$B^{arm}_{r,slotless}(r,\theta) = \mu_0 \sum_{v}^{\infty} \frac{3}{2} J_v F_v(r) I_1 \sin(\sigma_v v\theta - p\omega_r t) \tag{4.22}$$

$$B^{arm}_{t,slotless}(r,\theta) = \mu_0 \sum_{v}^{\infty} \frac{3}{2} \sigma_v J_v G_v(r) I_1 \cos(\sigma_v v\theta - p\omega_r t) \tag{4.23}$$

with

$$v = 1 \times F_1, 5 \times F_1, 7 \times F_1, 11 \times F_1 ... \tag{4.24}$$

$$\sigma_v = \text{sgn}(k_{\tau(v+1)} - k_{\tau(v-1)}) \tag{4.25}$$

$$J_v = \frac{2}{\pi} \frac{N_s pq}{R_{si}} k_{sov} k_{wv} \tag{4.26}$$

$$F_v(r) = \frac{1 + \left(\frac{R_{ro}}{r}\right)^{2v}}{1 - \left(\frac{R_{ro}}{R_{si}}\right)^{2v}} \left(\frac{r}{R_{si}}\right)^{v-1} \tag{4.27}$$

$$G_v(r) = \frac{1 - \left(\frac{R_{ro}}{r}\right)^{2v}}{1 - \left(\frac{R_{ro}}{R_{si}}\right)^{2v}} \left(\frac{r}{R_{si}}\right)^{v-1} \tag{4.28}$$

In these equations, $\theta = 0$ refers to the axis of phase A, the middle of the tooth around which phase A is wound. The rotational direction of the harmonic, described in the previous chapter, is taken into account by Equation 4.25, which uses $\sin(-x) = -\sin(x)$ and the fact that the tangential component of the flux density is related to the spatial derivative of the winding MMF [28]. In Equation 4.26, $N_s pq$ refers to the number of turns in series per phase and the slot opening factor K_{sov} is given by Equation 4.29, which is close to unity for lower harmonics but approaches zero for higher harmonics.

$$k_{sov} = \frac{\sin\left(v\frac{\beta_{so}}{2}\right)}{v\frac{\beta_{so}}{2}} \tag{4.29}$$

The winding factor k_{wv} is given by Equation 3.5, and the impact of the segment gaps on the winding factors is neglected. The product of Equation 4.27 and 4.29 is approximately equal to $\frac{R_{si}}{g'}\frac{1}{v}$ for $r = R_{si}$ [90], and thus results in the $1/v$ relation of the vth harmonic discussed in the previous chapter. Furthermore, in combination with the flux density formulas, it shows the term

$$\frac{\mu_0}{g'} = \Lambda_{g0} \tag{4.30}$$

which is the constant component of the air gap permeance for an equivalent air gap width g' [28]. Finally, G_v equals 1 for $r = R_{si}$, and can thus be neglected. It also means that the armature reaction has a tangential component even in the slotless machine, in contrast to the rotor field. Together, the radial and tangential components can be written in complex form

$$B^{arm}_{slotless} = B^{arm}_{r,slotless} + jB^{arm}_{t,slotless} \tag{4.31}$$

This term is only present in the loaded case, i.e. $I_1 \neq 0$. When saturation is neglected, $B_{slotless}$ is the linear superposition of the slotless rotor and stator fields. In contrast to the magnetic field due to the permanent magnets, all space harmonics of the winding field have the same frequency $p\omega_r$, meaning the waveforms can be considered to be rotating around the machine circumference at a frequency of $p\omega_r/v$. The slotless flux densities due to the winding fields are shown in Figure 4.4.

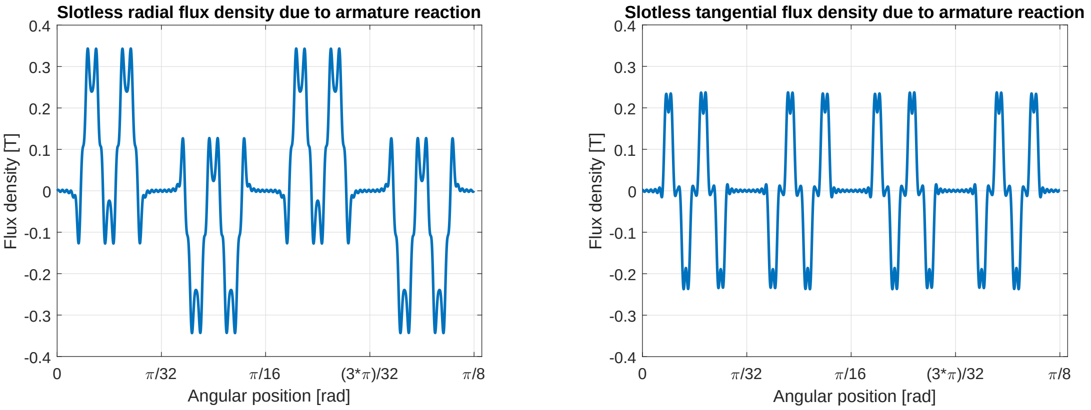

(a) Radial component

(b) Tangential component

Figure 4.4: The magnetic flux density due to the armature reaction along a slotless stator segment at t = 0 s*

4.5.3. Influence of slots and segment gaps

In order to account for the influence of the stator slots, a complex relative air gap permeance $\lambda(\theta)$ can be used [28, 93, 96]. The real and imaginary components of $\lambda_s = \lambda_{a,s} + j\lambda_{b,s}$ are obtained as described in Appendix B, and are expressed as Fourier series:

$$\lambda_{a,s}(\theta) = \lambda_0 + \sum_{i=1}^{N_\lambda} \lambda_{a,si} \cos\left(iN_s\theta\right) \tag{4.32}$$

$$\lambda_{b,s}(\theta) = \sum_{i=1}^{N_\lambda} \lambda_{b,si} \sin\left(iN_s\theta\right) \tag{4.33}$$

The same can be done to analyze the impact of the flux gaps between segments by treating the gap as a slot between very wide teeth. In that case, a second expression for the complex relative permeance λ_{gap} is obtained as shown in Equations 4.34 and 4.35.

$$\lambda_{a,gap}(\theta) = \lambda_0 + \sum_{i=1}^{N_\lambda} \lambda_{a,gapi} \cos\left(iN_{seg}\theta\right) \tag{4.34}$$

$$\lambda_{b,gap}(\theta) = \sum_{i=1}^{N_\lambda} \lambda_{b,gapi} \sin\left(iN_{seg}\theta\right) \tag{4.35}$$

These relative permeances are then superimposed to obtain the total relative permeance $\lambda = \lambda_a + j\lambda_b$, as shown below:

$$\lambda_a(\theta) = \lambda_0 + \sum_{i=1}^{N_\lambda} \lambda_{a,si} \cos\left(iN_s\theta\right) + \sum_{i=1}^{N_\lambda} \lambda_{a,gapi} \cos\left(iN_{seg}\theta\right) \tag{4.36}$$

$$\lambda_b(\theta) = \sum_{i=1}^{N_\lambda} \lambda_{b,si} \sin\left(iN_s\theta\right) + \sum_{i=1}^{N_\lambda} \lambda_{b,gapi} \sin\left(iN_{seg}\theta\right) \tag{4.37}$$

This means the relative permeance for a slotted, segmented stator has spatial orders at both multiples of N_s as well as multiples of N_{seg}. The relative permeance of this machine is shown in Figure 4.5, with the influence of the segment gap visible close to $\theta = 3\pi/32$.

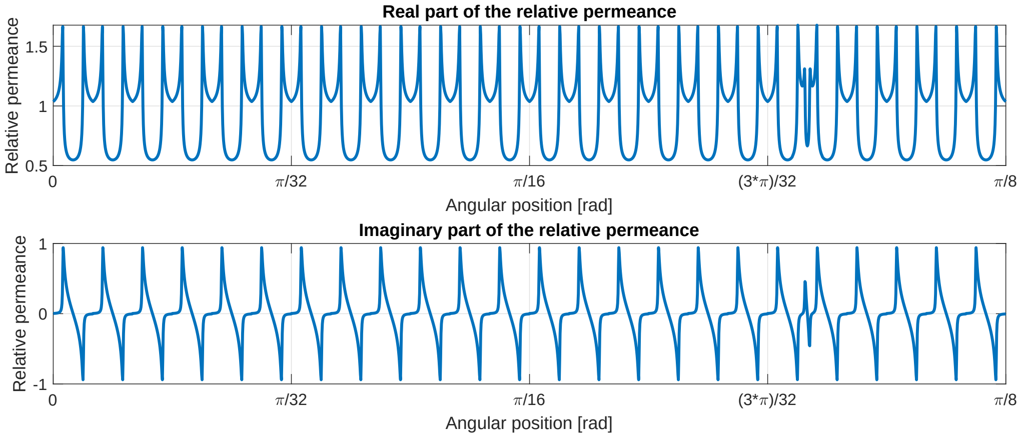

Figure 4.5: The real and imaginary part of the relative permeance for 1 segment, taking both slots and flux gaps into account

The relation between the magnetic flux density in the slotted machine B and the slotless machine $B_{slotless}$ is then given by $B = B_{slotless}\lambda^*$, with the asterisk representing the complex conjugate [96]. As the magnetic flux density due to the permanent magnets in a slotless machine is expressed as a complex value $B_{slotless} = B_{r,slotless} + jB_{t,slotless}$, the flux density in the slotted machine is given by

$$B^{PM} = B^{PM}_{slotless}\lambda^* \tag{4.38}$$

with

$$B^{PM}_r = \Re(B^{PM}_{slotless}\lambda^*) = B^{PM}_{r,slotless}\lambda_a + B^{PM}_{t,slotless}\lambda_b \tag{4.39}$$

$$B^{PM}_t = \Im(B^{PM}_{slotless}\lambda^*) = B^{PM}_{t,slotless}\lambda_a - B^{PM}_{r,slotless}\lambda_b \tag{4.40}$$

A similar expression holds for $B^{arm} = B^{arm}_{slotless}\lambda^*$. In the no-load case, the flux density in the air gap equals B^{PM}, while for the loaded case the total flux density in the air gap (neglecting saturation) equals the linear superposition of the fields due to the permanent magnets and the armature reaction[93]:

$$\begin{aligned} B^{tot} &= B^{PM} + B^{arm} \\ &= (B^{PM}_r + B^{arm}_r) + j(B^{PM}_t + B^{arm}_t) \\ &= (B^{PM}_{slotless} + B^{arm}_{slotless})\lambda^* \end{aligned} \tag{4.41}$$

The resulting flux density is shown in Figure 4.6 and 4.7. The line graphs show the spikes in the flux densities at the edges of each tooth, and apart from the segment gap, shows a flux distribution which repeats twice each segment. A Fast-Fourier Transform is performed on the slotted flux density at $t = 0$ to show the occurring spatial harmonics. The radial no-load case shows the expected slotless harmonics at odd multiples of p, as well as interactions between the slots and poles of spatial order $|\mu p \pm i N_s|$, discussed in Section 4.6.4. In the loaded case, the most important change is the addition of the low F_1 harmonic. In the tangential flux density, only interactions between the slots and poles are observed in the no-load case, as $B^{PM}_{t,slotless} = 0$ close to the stator.

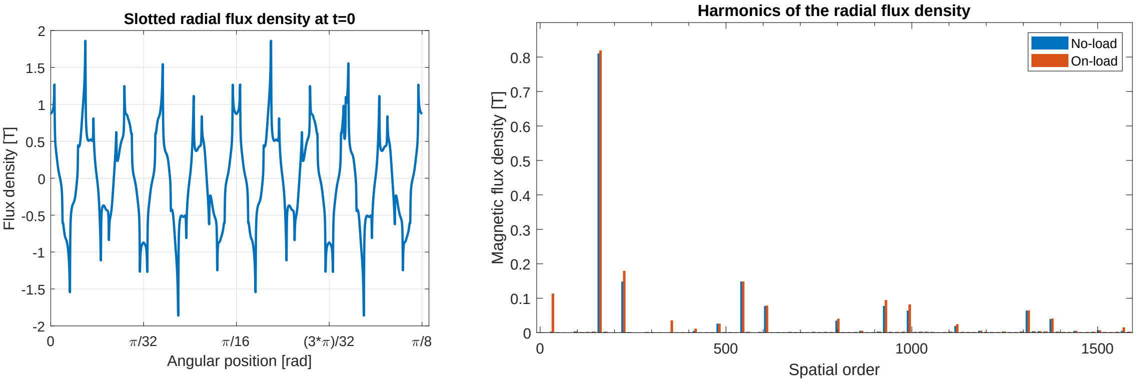

(a) Along the circumference*

(b) The spatial orders

Figure 4.6: The radial flux density for a slotted stator segment

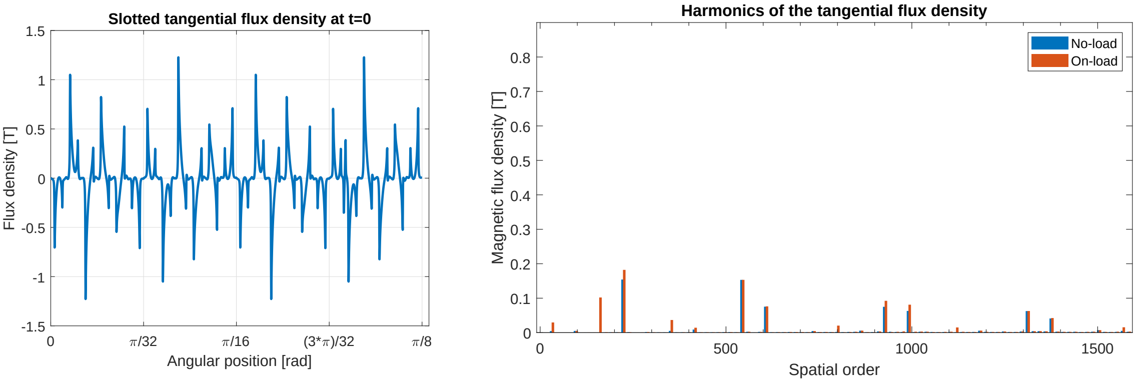

(a) Along the circumference*

(b) The spatial orders

Figure 4.7: The tangential flux density for a slotted stator segment

By calculating the magnetic flux density distribution for different t, and performing a 2D Fast-Fourier Transform to the result, the frequency of the different harmonics can be visualized as well. Figure 4.8 shows the main harmonic at spatial order $p = 160$ and electrical frequency $p\omega_r/(2\pi) = 26.7$ Hz, as well as harmonics of the rotor and stator. The rotor harmonics occur at the diagonal line upwards, while the armature harmonics occurs at the horizontal lines of constant frequency, showing both forward and backward rotating waves.

4.6. Radial forces and vibrations

Based on Equation 4.5, the radial forces resulting from the magnetic flux density can be obtained. For most machines, the contribution of the tangential component of the flux density on the radial forces f_{rt} is neglected[28], but for large, open-slot machines it needs to be taken into account [77]. However, as the radial and tangential flux density distributions have the same spatial orders only the magnitude of the resulting forces changes, while the occurring force harmonics remain the same.

Equations 4.1, 4.5 and 4.8 show that the radial force harmonics with spatial order m result from the interactions of harmonics in the flux density waves of the rotor and stator. Figures 4.9 and 4.10

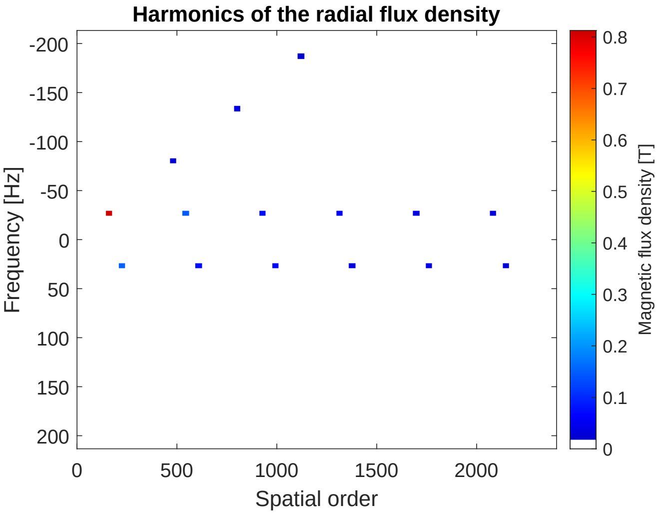

Figure 4.8: The 2D FFT of the radial flux density, showing both spatial orders and the frequencies at which they occur

show the spatial and 2D FFT of the radial force respectively, in which a rich harmonic spectrum can be observed. The different interactions of the harmonics in the magnetic field will be analyzed in the following subsections.

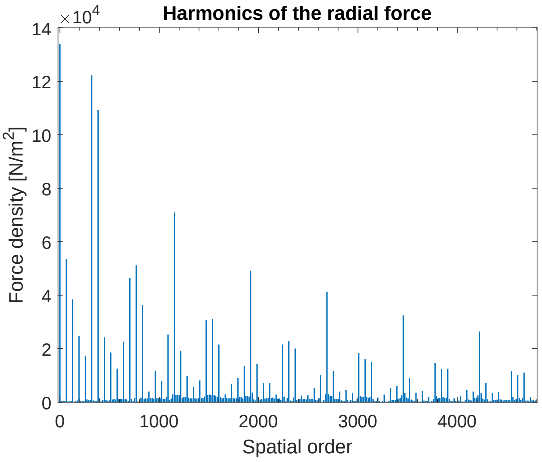

Figure 4.9: The spatial orders of the radial force

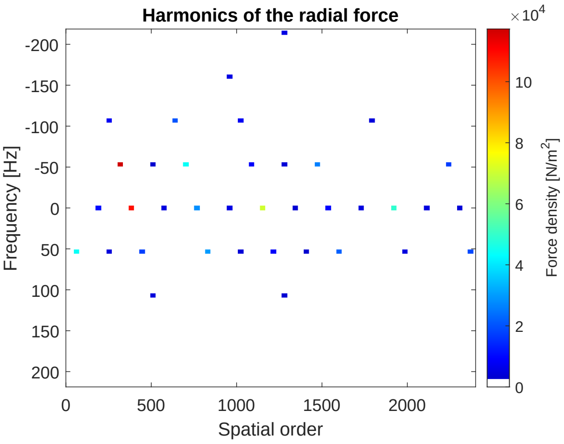

Figure 4.10: The 2D FFT of the radial force, showing both spatial orders and the frequencies at which they occur

4.6.1. Breathing mode

Vibrations with $m = 0$ occur due to the interaction of flux density waves with the same spatial order, but with different frequencies [28]. For synchronous machines driven by balanced, sinusoidal currents, very few time harmonics are present and the breathing mode is usually negligible compared to force harmonics with a higher spatial order [72]. For inverter-fed machines, time harmonics exist in the currents, which will contribute to the zeroth order vibration mode [75]. This will be analyzed in more detail in Section 4.8.

The zeroth spatial order can be analyzed by taking the mean value of the radial force density along the stator circumference. This will have a time-constant component, leading to static deflection of the stator structure, and a time-varying component, leading to the zeroth order vibration mode. As shown in Figure 4.8, all flux density harmonics of a certain spatial order have the same frequency in the case of balanced, sinusoidal currents, which means the zeroth vibration mode is very low. The average radial force is shown in Figure 4.11, which shows a deviation of only 1% of the DC component at a frequency 6 times the electrical frequency [8].

Even though the amplitude of the zeroth order is low, the deformation caused by this vibration mode can still be dominant due to the relatively low stiffness of the structure for this mode shape [72, 75]. This is true particularly for machines without low non-zero force harmonics, which is the case for machines with a high gcd (N_s, p) as will be explained in Section 4.6.4. The deformations will be studied in Chapter 5.

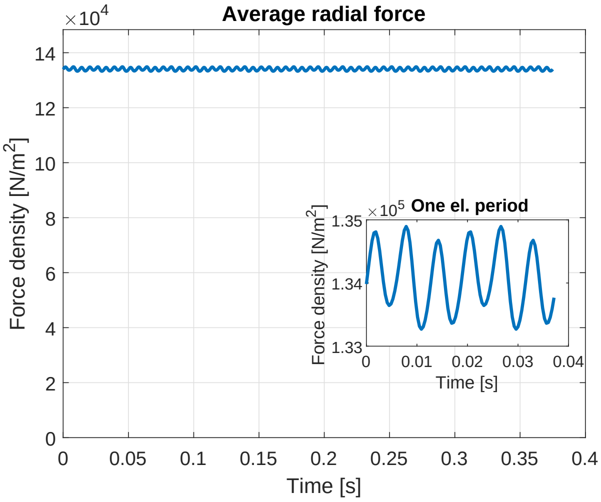

Figure 4.11: The average radial force density over time

4.6.2. Beam bending mode

Vibrations with $m = 1$ occur primarily due to static or dynamic eccentricity of the rotor [28]. Static eccentricity means that the air gap differs over a fixed reference frame, causing an additional non-rotating force. Dynamic eccentricity refers to a difference in air gap which rotates with the rotor frequency ω_r. This mode is mainly caused due to misalignment of the stator and rotor axes, or due to one of them being not perfectly circular. As the stator are assumed to be perfectly aligned and centered, this case is not considered further. If one of the segments would be inoperative, the unbalanced forces also lead to a $m = 1$ force order. This non-nominal case is also not considered in this thesis.

4.6.3. Interactions of the slotless flux densities

Equation 4.5 shows that the radial forces from the slotless flux densities result from the square of four Fourier series, the radial and tangential component of the permanent magnets and the armature reaction. Since the tangential components have the same spatial orders as the radial components, they are neglected in this discussion.

The square of the total radial flux density has three components[19, 28]:

$$f_{rr} = \frac{B^2_{r,slotless}}{2\mu_0} = \frac{(B^{PM}_{r,slotless})^2 + 2B^{PM}_{r,slotless}B^{arm}_{r,slotless} + (B^{arm}_{r,slotless})^2}{2\mu_0} \tag{4.42}$$

- The interaction of rotor harmonics with order $\mu = 1, 3, 5....$ As the magnetic field from the permanent magnets is usually much larger than the armature reaction field, the dominant radial force vibrations come from the spatial harmonics in $B^{PM}_{slotless}$:

$$f_r(\theta, t) \propto \frac{\left[\sum\limits_{\mu=1,3,5...}^{\infty} B_{m\mu} \cos\left(\mu p(\theta - \omega_r t)\right)\right]^2}{2\mu_0} = \sum_{\mu=1,3,5...}^{\infty} \frac{B^2_{m\mu}}{4\mu_0} + \sum_{k=1,2,3...}^{\infty} f_k \cos\left(2kp(\theta - \omega_r t)\right) \tag{4.43}$$

Which uses Equation 4.8, substituting $k = \mu p$, $\omega_k = \mu p \omega_r$ and only considering odd harmonics. The magnitude of force is given by

$$f_k = \sum_{|\mu_1 \pm \mu_2| = k} \frac{B_{m\mu_1} B_{m\mu_2}}{2\mu_0} \tag{4.44}$$

which represents the interacting harmonics μ_1 and μ_2. This means force orders k are produced by the sum of flux harmonic pairs with $|\mu_1 \pm \mu_2| = k$. Furthermore, it shows that the permanent magnets create a radial force with a constant term and terms varying with spatial order $m = 2kp$, integer multiples of the number of poles.

- The interaction of stator harmonics with order $v = 1, 5, 7... \times F_1$:

$$\begin{aligned} f_r(\theta, t) &\propto \frac{\left[\sum\limits_{v=1,5,7...}^{\infty} B_{mv} \cos\left(vF_1\theta - p\omega_r t\right)\right]^2}{2\mu_0} \\ &= \sum_{v=1,5,7...}^{\infty} \frac{B_{mv}^2}{4\mu_0} + \sum_{k=1,2,3}^{\infty} f_{k1} \cos\left(2kF_1\theta\right) + \sum_{k=1,2,3}^{\infty} f_{k2} \cos\left(2kF_1\theta - 2p\omega_r t\right) \end{aligned} \tag{4.45}$$

Which uses Equation 4.8 substituting $k = vF_1$, $\omega_k = p\omega_r$ and only considering odd harmonics. The amplitudes of the forces are given by

$$f_{k1} = \sum_{|v_1 - v_2| = k} \frac{B_{mv_1} B_{mv_2}}{2\mu_0} \tag{4.46}$$

$$f_{k2} = \sum_{|v_1 + v_2| = k} \frac{B_{mv_1} B_{mv_2}}{2\mu_0} \tag{4.47}$$

This means the stator harmonics create a time-constant force consisting of a zeroth order as well as spatial orders $m = 2kF_1$, and a time-varying force with spatial order $m = 2kF_1$ and frequency $2p\omega_r$. The time-varying forces with harmonic k are created by the interaction of flux harmonic pairs with $|v_1 + v_2| = k$.

- The interaction of stator and rotor harmonics:

$$f_r(\theta, t) \propto \frac{2 \times \sum\limits_{\mu=1,3,5...}^{\infty} B_{m\mu} \cos\left(\mu p(\theta - \omega_r t)\right) \times \sum\limits_{v=1,5,7...}^{\infty} B_{mv} \cos\left(vF_1\theta - p\omega_r t\right)}{2\mu_0} \tag{4.48}$$

For a given rotor harmonic μ and a stator harmonic v, this results in force harmonics with

  - an amplitude $B_{m\mu} B_{mv} / 2\mu_0$
  - a spatial harmonic $m = \mu p \pm vF_1$, which, as p is an odd multiple of F_1, gives an integer multiple $m = 2kF_1$
  - a frequency of $\mu p\omega_r \pm p\omega_r = (\mu \pm 1)p\omega_r$, which, as μ is odd, gives a multiple of $2p\omega_r$

A summary of these force harmonics is given at the end of this section in Table 4.1.

4.6.4. Slot harmonics

When slots are taken into account, interactions between the permanent magnet field and the slots occur[28] which are especially strong for large, open-slot machines with fractional windings [71, 77]. Neglecting the influence of the segment gaps at first, Equation 4.39 gives

$$B_r^{PM} \propto \sum_{\mu=1,3,5...}^{\infty} B_{m\mu} \cos\left(\mu p(\theta - \omega_r t)\right) \times \sum_{i=1}^{N_\lambda} \lambda_{a,si} \cos\left(iN_s\theta\right) \tag{4.49}$$

This means the interaction between the permanent magnets and the slots, called the slot harmonics, have spatial harmonic in the magnetic flux density at spatial orders[93]

$$|\mu p \pm i N_s| \qquad \text{for } \mu = 1, 3, 5... \text{ and } i = 1, 2, 3... \tag{4.50}$$

with a frequency of $\mu p \omega_r$. As will be discussed in Chapter 5, the lowest spatial orders create the largest deformations in the stator. From above equation, it follows that the lowest occurring order is the greatest common divisor of the number of pole pairs and the number of slots, gcd (p, N_s), which is often used in literature [8, 13, 74–77]. This coincides with the periodicity of the machine, as discussed in Section 3.2. As the radial force is dependent on the square of the magnetic flux density and N_s and p are both even, the minimum spatial order in the force equals

$$m_{min} = 2 \times \text{gcd}\,(p, N_s) \tag{4.51}$$

For integer slot windings ($q = 1, 2, 3...$), this equals $2p$, meaning the minimum order is not reduced compared to the slotless case. However, for concentrated windings ($q < 0.5$) the greatest common divisor can be as low as 1, leading to a force order $m = 2$. To reduce vibrations, it is beneficial to increase gcd (p, N_s) [76].

These additional flux density harmonics exist in both the radial and the tangential component, and can lead to additional force harmonics through their interactions with other harmonics. As both $B_{m\mu}$ and $\lambda_{a,si}$ in Equation 4.49 decrease quickly with increasing μ and i respectively, the most important added harmonics denoted by Equation 4.50 exist for low values of μ and i. Notably, the fundamental harmonics of the permanent magnet field and the permeance create a harmonic at $|N_s - p|$ with a large amplitude, which interacts again with the fundamental rotor harmonic of order p following Equation 4.8, leading to a force harmonic with order $m = |N_s - 2p|$ at frequency $2p\omega_r$.

As N_s and $2p$ are often close together for machines with concentrated windings[12], this usually leads to vibrations with a low spatial order and a high amplitude [77]. For this machine, $|N_s - 2p| = 2 \times$ gcd $(p, N_s) = 64$, which is visible in Figures 4.9 and 4.10 as the lowest spatial order with a relatively high amplitude.

Other force harmonics resulting from the slot harmonic that can be identified in Figure 4.9 are

- $m = 384$, resulting from interactions between rotor field harmonic $p = 160$ and slot harmonic $N_s - p = 224$
- $m = 704$, resulting from interactions between rotor field harmonic $p = 160$ and slot harmonic $N_s + p = 544$
- $m = 1152$, resulting from interactions between rotor field harmonic $p = 160$ and slot harmonic $3N_s - p = 992$, as well as slot harmonic $N_s - p = 224$ and slot harmonic $2N_s + p = 768$

as well as many others. The strongest occur at odd multiples of 384, coinciding with N_s.

4.6.5. Segment harmonics

Segmenting the stator will influence the force harmonics as well. First of all, if a small air gap exists between the segments, this will act as an extra slot with permeance harmonics of spatial orders equal

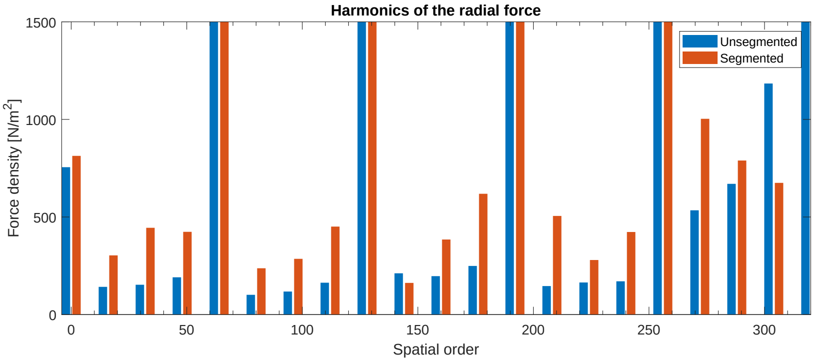

Figure 4.12: Comparison of the lowest spatial orders for a machine with and without a segmented stator

to multiples of N_{seg}. This means that similar to the slot harmonic, segment harmonics occur with flux density harmonics at

$$|\mu p \pm i N_{seg}| \qquad \text{for } \mu = 1,3,5... \text{ and } i = 1,2,3... \tag{4.52}$$

which means the lowest added flux density harmonic occurs at gcd (p, N_{seg}), which is usually equal to N_{seg}. This could be very low if the number of segments is small, but the amplitude will be limited by the small width of the segment gap. The force harmonics are too small to be visible in Figure 4.9, so Figure 4.12 shows a close-up of the lowest spatial orders for both a segmented and an unsegmented machine. The segment gaps are found to increase the amplitude of spatial orders at multiples of $N_{seg} = 16$. Even though the amplitude is still only a few percent of the dominant spatial orders at multiples of $2 \times F_1 = 64$, their impact on the deformation of the stator can be significant, as will be discussed in Chapter 5.

This is however not the only effect of the segment gaps on the magnetic flux density and force harmonics. Besides the effect on the winding factors discussed in Section 2.2, the segment gaps will also influence the magnetic field lines flowing in and out of the stator core. They could have a focusing or defocusing effect on certain spatial orders as observed in other modular machines,[46] but the effect is hard to predict analytically [34]. In particular, spatial orders at multiples of $N_{seg} = 16$ could be increased, due to the prevention of leakage flux out of each segment. Overall, the effect is expected to be small, and neglected in the analytical model.

Table 4.1: Summary of resulting radial force density harmonics

Type	**Spatial order**	**Frequency**	**Comments**
Breathing mode	0	Mainly $6\omega_e$	Low for sinusoidal currents
Due to slotless PM fields	$2kp$	$2k\omega_e$	Dominant in most machines
Due to slotless armature fields	$2kF_1$	$2\omega_e$	Only present in on-load case
Due to interactions of PM harmonic μ and armature harmonic v	$\mu p \pm vF_1$	$(\mu \pm 1)\omega_e$	Only present in on-load case
Slot harmonics	$2kF_1$	Mainly $2\omega_e$	Adds low-order harmonics
Segment harmonics	kN_{seg}	Mainly $2\omega_e$	Creates very low-order harmonics
For $k = 1,2,3...$			

4.7. Tangential force harmonics and torque pulsations

In the tangential forces, similar harmonics occur as in the radial forces. The 'zeroth tangential order' results in the torque of the machine, which can have a time-constant component and a time-varying component. This time-varying component causes torque pulsations, within which two different components can be distinguished[28]:

- The cogging torque, present in the loaded and the no-load case, caused by the interaction of the permanent magnets and the slotted stator
- Other torque harmonics, referred to as the torque ripple, only present in the loaded case, caused by interactions between the rotor and stator fields.

Similar to the zeroth-order radial forces, torque can only be produced by flux density harmonics of the same spatial order, and the torque harmonics are stronger in the case of time harmonics in the currents due to power electronic converters. But unlike zeroth-order radial forces, the torque pulsations can be significant even for sinusoidal currents. This will be analyzed in the subsections below.

Finally, tangential force harmonics with higher spatial orders are produced as well, both in the loaded and the no-load case. As their integral along the air gap circumference is zero, they do not contribute to the overall torque produced by the machine. However, these forces do act on the stator teeth, leading to additional vibrations.

4.7.1. Constant torque

The torque is found by integrating Equation 4.6 along the inner stator surface, multiplied by the radius [28]. Assuming the magnetic fields are constant along the effective machine length, this can be written as a line integral along the inner stator contour l:

$$T = L\left(\frac{1}{\mu_0}\oint_l rB_rB_t\,dl\right) \tag{4.53}$$

This will result in a function dependent on t, and thus on the rotor position.

4.7.2. Cogging torque

Cogging torque occurs due to the variation in air gap permeance as caused by the slotted stator, and is thus present even in the no-load case. It can be analyzed in a similar way as the radial forces by integrating the magnetic forces over the depth of a tooth[88], by applying an energy-based method,[22, 28, 36, 37] or by using Equation 4.53 in the no-load case. The first two methods did not give satisfactory results, so the latter has been employed. To understand which harmonics contribute to the cogging torque, the equation is expanded:

$$\begin{aligned} T_c(\theta_r) &= \frac{LR_{PM}^2}{\mu_0}\int\limits_0^{2\pi} B_r^{PM}B_t^{PM}\,d\theta \\ &= \frac{LR_{PM}^2}{\mu_0}\int\limits_0^{2\pi} B_{r,slotless}^{PM}(\theta,\theta_r)\lambda_a(\theta)\times B_{r,slotless}^{PM}(\theta,\theta_r)\lambda_b(\theta)\,d\theta \end{aligned} \tag{4.54}$$

which uses the fact that the tangential component of $B_{slotless}^{PM}$ is zero close to the stator edge. From Equation 4.43 it is known that the square of the magnetic field due to the permanent magnets can be expressed as

$$(B_{r,slotless}^{PM}(\theta,\theta_r))^2 = \sum_{k=0,1,2\ldots}^{\infty} B_k' \cos\left(2kp(\theta-\theta_r)\right) \tag{4.55}$$

which has a fundamental period of $2\pi/2p$. Similarly, the product of the radial and tangential part of the relative air gap permeance due to the slots equals

$$\lambda_a(\theta)\times\lambda_b(\theta) = \sum_{k=0,1,2\ldots}^{\infty} \lambda_k' \cos\left(kN_s\theta\right) \tag{4.56}$$

which has a fundamental period of $2\pi/N_s$. Using the trigonometric orthogonality

$$\int_0^{2\pi}\cos n\theta\cos m\theta\,d\theta = \begin{cases}\pi, & \text{if } n=m\\ 0 & \text{if } n\neq m\end{cases} \tag{4.57}$$

Equation 4.54 gives

$$T_c(\theta_r) = \frac{L\pi R_{PM}^2}{\mu_0}\sum_{k=1}^{\infty} B_{kN_L}'\lambda_{kN_L}' \sin\left(kN_L\theta_r\right) \tag{4.58}$$

with $N_L = \text{lcm}\,(N_s,2p)$ and B_{kN_L}', λ_{kN_L}' referring to the Fourier coefficients of the squared flux density and the permeance at multiples of N_L. This shows the importance of the lowest common multiple of the number of poles and slots, which is often used as a design parameter for the cogging torque of machines [8, 37, 41, 76, 89]. The higher the LCM, the smaller the cogging torque, as only higher order harmonics of B^2 and λ^2 will play a role. This shows three things:

- There is a trade-off between cogging torque and radial vibrations resulting from the slot harmonics. As mentioned in section 4.6.4, increasing the GCD of the number of poles and slots reduces the radial vibrations, but the GCD and LCM cannot be changed independently as

  $$\text{lcm}\,(a,b)\times\text{gcd}\,(a,b) = a\times b \tag{4.59}$$

  This also explains why gcd $(N_s,2p)$ is sometimes used as ”goodness factor” for the cogging torque [89].

- Equation 4.58 shows that the cogging torque has a fundamental period of $2\pi/N_L$ along the machine circumference. This can be very small for machines with concentrated windings, due to gcd (N_s, p) being very small as discussed before. This is partially explained by the fact that for concentrated windings, the permanent magnets do not face the slot openings simultaneously, as is the case for machines with distributed windings [89].
- This explains why the cogging torque for open-slot machines is more pronounced: their effect on the relative permeance is much stronger than that of (semi-)closed slots.

In practice, especially for machine with a high lcm $(N_s, 2p)$, the cogging torque is dominated by the fundamental harmonic of Equation 4.58 with spatial order N_L. From Equation 4.8 it can be concluded that the determining harmonics in $(B^{PM}_{r,slotless})^2$ come from flux harmonic pairs for which holds that $|\mu_1 p \pm \mu_2 p| = N_L$. The same holds for harmonic pairs in in λ^2. For this machine, $N_L = 1920$, which is equal to $12p$. Figure 4.13 shows the cogging torque with a fundamental period of $2\pi/1920 \approx 0.003$ and an amplitude of 10 kNm, or 0.1% of the nominal torque.

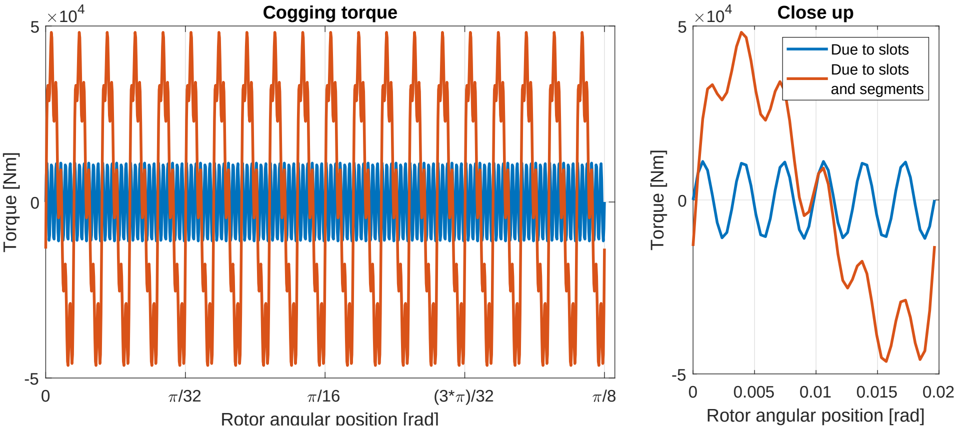

Figure 4.13: The cogging torque as function of the rotor position

The same formula holds for the cogging torque due to the flux gaps, replacing λ with the segment permeance Fourier series and using $N_L =$ lcm $(N_{seg}, 2p)$. As N_s is an integer multiple of N_{seg}, the fundamental order of the resulting cogging torque is lower [34, 46]. In fact, as N_{seg} is usually chosen as an integer fraction of $2p$ to ensure symmetry, N_L equals $2p$. This means the addition of flux gaps can lead to a significantly higher cogging torque, as the fundamental waveform of $B^{PM}_{r,slotless}$ will interact with the flux gaps between the segments [86]. Figure 4.13 shows a segment cogging torque of 47 kNm (0.5% of the nominal torque) with a period of $2\pi/2p = 0.02$, significantly slower and stronger than the cogging torque due to the slots.

Even very small segment gaps can increase the cogging torque, due to the change in the tangential flux density in the air gap [86, 87]. As the influence of the segment gaps on the armature reaction is not considered, this effect is neglected in the analytical model.

4.7.3. Torque ripple

Besides the cogging torque, interactions between the harmonics in the permanent magnet and armature field of the same spatial order can create additional pulsations in the torque. This can again be analyzed using Equation 4.53. Figure 4.14 shows the torque calculated from the magnetic fields of the rotor and the segmented stator. The unsegmented stator gave very similar results, meaning the stator segments do not have a significant effect on the torque ripple. The figure shows a constant torque of 8.6 MNm, 10% lower than the design torque, and a torque ripple of 200 kNm, 2% of the nominal torque. The torque ripple occurs at 6 times the electrical frequency as expected from theory[48, 76], due to the interaction of the 5th and 7th rotor harmonic with stator harmonics at the same spatial order.

4.7.4. Higher spatial orders in the tangential forces

As the tangential component of the flux density has the same harmonics as the radial component, similar harmonics will also be present in the tangential force as the ones discussed in the sections on the radial forces. Figure 4.15 shows these spatial orders, with peaks at odd multiples of N_s and $m_{min} = 64$. These higher harmonics do not result in useful torque, but will act as vibrations on the stator teeth.

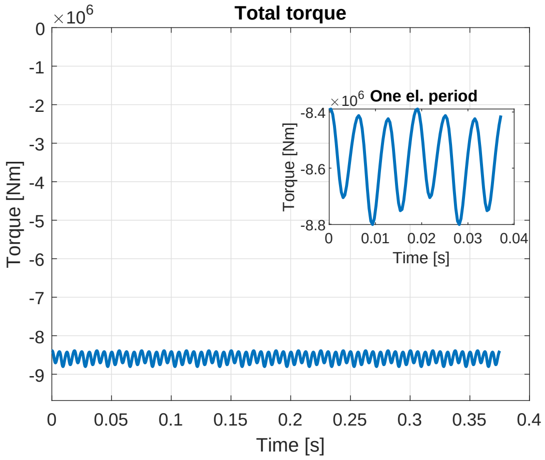

Figure 4.14: An example of the total torque over time

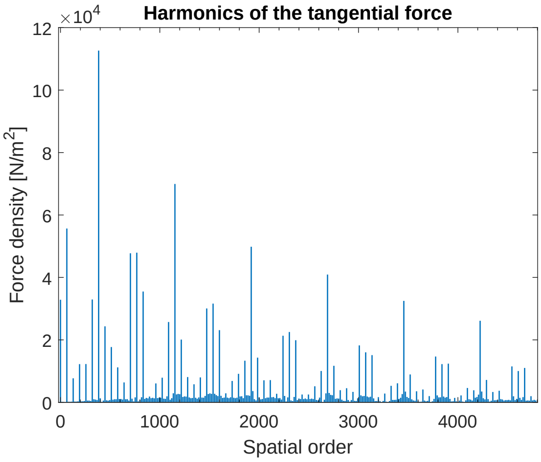

Figure 4.15: Spatial orders in the tangential force

4.8. Influence of Power Electronic Converters

While until this point sinusoidal currents were assumed, in reality the segments are connected to a Power Electronic (PE) Converter, which causes time harmonics in the phase currents. These time harmonics lead to additional vibrations and noise in the electric machine [28]. To study the effect of this accurately, a converter model with current control should be simulated in order to obtain the phase currents. This was outside the scope of this thesis, so only the effect of arbitrary higher time harmonics is demonstrated.

In previous work, different converter topologies for the ModHVDC Generator have been studied, and a switching frequency of 1 kHz has been selected [25]. In this thesis, a Two-Level Voltage Source Converter (2L-VSC) will be considered. The ratio between the switching frequency f_s and the fundamental frequency f_e is set to 39, an odd multiple of 3, to prevent low subharmonics [51]. This gives a switching frequency of $f_s = 1040$ Hz.

The most important time harmonics coming from a 2L-VSC with PWM control occur at $f_s \pm 2f_e$ [28, 75]. This means that on top of the fundamental current $h = 1$, two harmonics are superimposed, at $h = 37$ and $h = 41$. As example, the amplitude of both these harmonics is estimated at 2% of the fundamental harmonic [25, 75], which results in the phase currents shown in Figure 4.16.

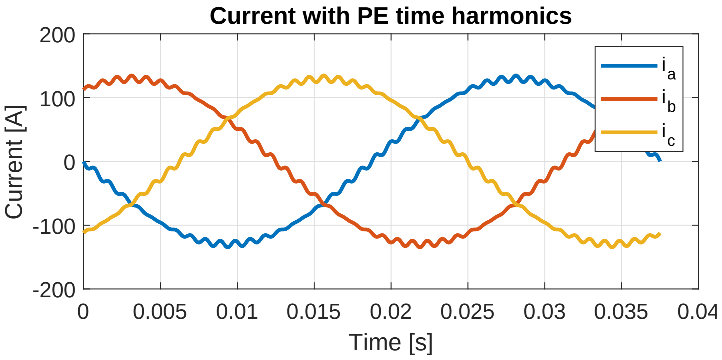

Figure 4.16: The phase currents with harmonics from the Power Electronic Converter

When time harmonics are considered, Equation 4.22 for the magnetic flux density of the armature reaction becomes: [93]

$$B^{arm}_{r,slotless}(r,\theta) = \mu_0 \sum_{v}^{\infty}\sum_{h}^{\infty} \frac{3}{2} J_v F_v(r) I_h \sin\left(\sigma_v v\theta - hp\omega_r t\right) \tag{4.60}$$

$$B^{arm}_{t,slotless}(r,\theta) = \mu_0 \sum_{v}^{\infty}\sum_{h}^{\infty} \frac{3}{2} \sigma_v J_v G_v(r) I_h \cos\left(\sigma_v v\theta - hp\omega_r t\right) \tag{4.61}$$

with the same parameters as the original equations. This shows that for higher time harmonics in the current I_h, magnetic flux density harmonics are produced at the same spatial orders as for the fundamental current I_1, but at higher frequencies. From Equation 4.8 it was noted that the interaction of magnetic flux density harmonics with the same spatial order but different frequencies produce time variations in the zeroth force order. For the radial forces, this leads to the breathing mode, and for the tangential forces, this leads to a torque ripple. This interaction will also lead to high frequency harmonics at twice the spatial order of the flux density harmonics; most importantly at the fundamental harmonic F_1 and main harmonic p [10].

As expected, the main difference in the results caused by the PE converter was found in the breathing mode and the torque ripple, shown in Figures 4.17 and 4.18. The figures show that for two higher time harmonics at an amplitude of only 2% of the nominal current, the peak-to-peak ripple in both forces is tripled. The added ripple in the breathing mode and torque occurs at frequencies close to the switching frequency of 1 kHz. A similar time harmonic will be added to the $2F_1$ and $2p$ force orders.

The strong increase of these ripples due to the PE converter is in agreement with literature [72, 75]. It will be important to consider the harmonics coming from the PE converter when determining the mechanical response, especially on the breathing mode, and the forces orders $2F_1$ and $2p$ [10]. This will be discussed in the next chapter.

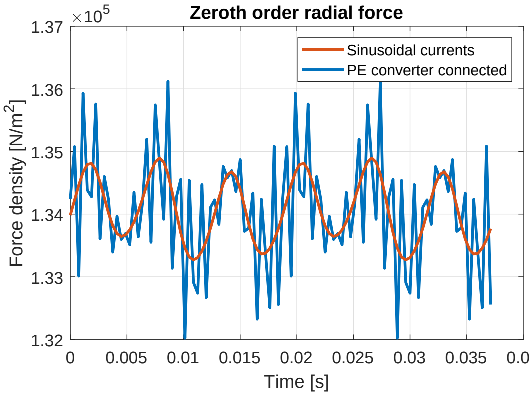

Figure 4.17: Influence of the current harmonics on the 0th order

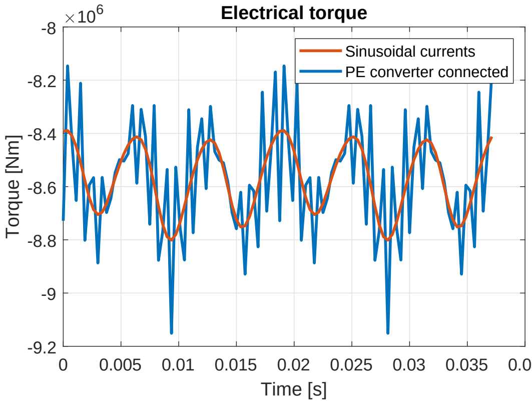

Figure 4.18: Influence of the current harmonics on the torque

4.9. Summary

An analytical model to predict the electromagnetic fields and the resulting forces has been set up. The most important forces are:

- The breathing mode at $6\omega_e = 160$ Hz
- The slot harmonics at multiples of $m = 2F_1 = 64$, mainly occurring at $2\omega_e = 53.3$ Hz
- The segment harmonics at multiples of $m = N_{seg} = 16$, mainly occurring at $2\omega_e = 53.3$ Hz
- The main radial harmonic at $2p$ and a frequency of $2\omega_e = 53.3$ Hz
- The torque ripple at $6\omega_e = 160$ Hz

Overall, most force harmonic with a higher spatial order occur at $2\omega_e = 53.3$ Hz, and a few at $4\omega_e = 106.7$ Hz and $6\omega_e = 160$ Hz.

The main impact of segmentation was found to be twofold: an increase in the cogging torque and the addition of segment harmonics at low spatial orders. Finally, the impact of the switching frequency of the PE converter was studied, and found to add harmonics in the radial breathing mode and the torque at $f_s = 1040$ Hz.

5

Mechanical model

This chapter describes the model used to estimate the mechanical response to the forces calculated in the previous chapter. The focus lies on the radial forces on the segmented stator and the support frame, but other vibrations are discussed in Section 5.4. As will be discussed below, a fundamental aspect of calculating the mechanical response is to determine the eigenmodes of the system, with their corresponding eigenfrequencies. These eigenmodes are used to perform a modal analysis, as is commonly used for electrical machines [7, 26]. A simplified analytical method is used to give an estimate of these eigenfrequencies, but as these models are generally inaccurate for complex structures [28], they will be verified with a Finite Element Model in Section 6.3.

5.1. Forced vibrations and modal superposition

Vibrational analysis is based on the generalization of the analysis of a simple mass-damper-spring system [13, 28, 70]. A mass m connected to a spring with stiffness k and a damper with damping coefficient c, excited by a force $F(t)$ has the following Equation of Motion for displacement $x(t)$:

$$mx''(t) + cx'(t) + kx(t) = F(t) \tag{5.1}$$

In the undamped case $c = 0$, the equation has a homogeneous solution of the form

$$x(t) = A \cos \omega^* t \tag{5.2}$$

with the natural frequency or eigenfrequency defined as

$$\omega^* = \sqrt{\frac{k}{m}} \tag{5.3}$$

This is the frequency at which the mass vibrates if it is released without external excitation. Taking into account damping again and assuming a sinusoidal excitation force $F(t) = F_0 \cos \omega t$, the solution has both a homogeneous solution, which consists of a vibration that dies out over time depending on the level of damping, and a particular solution, which is of interest here:

$$x(t) = \frac{F}{m} \frac{1}{\sqrt{((\omega^*)^2 - \omega^2)^2 + (2\zeta\omega\omega^*)^2}} \cos \omega t \tag{5.4}$$

with the damping coefficient given by

$$\zeta = \frac{c}{2\sqrt{mk}} \tag{5.5}$$

This shows that an oscillation will occur at the same frequency as the excitation force, with an amplitude that is dependent on both the undamped natural frequency and the excitation frequency. In particular, if the excitation frequency is close to the natural frequency, resonance occurs and the amplitude is only bounded by the damping coefficient.

For a system with multiple Degrees of Freedom, the same Equation of Motion is used in matrix form for a displacement **u**:

$$\mathbf{M}\mathbf{u}''(t) + \mathbf{C}\mathbf{u}'(t) + \mathbf{K}\mathbf{u}(t) = \mathbf{F}(t) \tag{5.6}$$

When used in a Finite Element Analysis, the matrices represent the parameters of the discretized system. Using the same analysis as before, a list of eigenfrequencies is found, with corresponding mode shapes $\mathbf{u}_m$. The fact that these eigenmodes are orthogonal with respect to the mass and stiffness matrix is used when performing a modal analysis. In this analysis, the mode shapes are considered separately, instead of each individual Degree of Freedom. The assumption of performing a modal analysis is that the total displacement of the structure equals the linear superposition of the eigenmodes:

$$\mathbf{u}(t) \approx \sum_{i}^{k} q_k(t)\mathbf{u}_k \tag{5.7}$$

with q_k representing the modal amplitudes. This assumption holds true if the eigenmodes are decoupled, which in reality only holds if the modal damping matrix **C** is diagonal. In general, modal analysis assumes damping to be small for each mode, as it neglects coupling between the different mode shapes [13]. The simplest damping model, modal damping, assumes that each eigenmode m has its own damping ratio ζ_m. Finally, the excitation force needs to be projected on the different eigenmodes. For radial vibrations, this is similar to what was already done in Chapter 4 by decomposing the forces in spatial orders.

This thus means that an important aspect of the mechanical analysis consists of finding the relevant eigenmodes and their corresponding eigenfrequencies. For complex shapes, these need to be determined using a numerical solver, but for simple shapes such as plates, beams or thin shells, they can be described explicitly. By simplifying the stator core and frame to thin cylinders, their eigenmodes can be described by a radial and an axial order. The radial vibration order is defined in a similar way as the radial force orders, based on the number of peaks along the circumference.

Vibration modes are excited by forces with the same order m [28]. By decomposing the force into the orders that excite each eigenmode, a Frequency-Response Function (FRF) can be derived [13, 24, 75]. Besides a radial order, eigenmodes also have an axial order n defined by the number of peaks along the axial length, as shown in Figure 5.1. Assuming that the ends of the cylinder are constrained, the axial 'breathing mode' $n = 0$ does not exist. Due to this interaction between radial and axial deformations, a 3D model is required to analyze the mechanical aspects of an electrical machine.

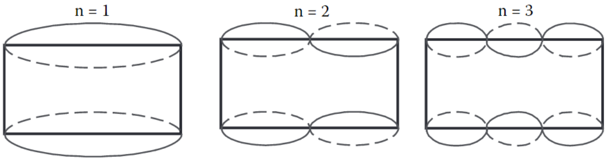

Figure 5.1: The axial modes occurring in a thin cylinder with clamped ends [28].

5.2. Model description

The geometry used for the mechanical analysis is described by the parameters of Table 3.2, and the material parameters are given in Table 5.1. The laminated core of the stator is modeled as a transversely isotropic material, as will be described in Section 5.2.1. For the frame, isotropic steel is assumed, and the windings are modeled as a combination of copper and insulation material.

It is assumed that the ends of the cylindrical frame are clamped, either by the attachment to the nacelle structure or by two endbells. Other attachment methods can be analyzed by changing the boundary conditions of the model. The stator core segments are assumed to be constrained by the frame only, in one of two ways:

- In case of an interference fit, the frame inner radius is slightly smaller than the stator outer radius. Once the segment is inserted, both components are deformed, resulting in a radial force on both components. Due to the resulting friction, the stator segments are held in position.
- In the second model, the stator segments are held in position by means of 2 or 3 mounting beams.

Table 5.1: Mechanical parameters

Stator core parameters	
Core density ρ_c	7700 kg/m^3
Stacking factor k_{st}	0.96
In-pane Young's modulus E_p	180 GPa
Out-of-plane Young's modulus E_z	100 GPa
In-plane Poisson ratio ν_p	0.2
Out-of-plane Poisson ratio ν_{zp}	0.1
In-plane Shear modulus G_p	75 GPa
Out-of-plane Shear modulus G_{zp}	15 GPa
Frame parameters	
Steel density ρ_f	7850 kg/m^3
Young's modulus E_f	200 GPa
Poisson ratio ν_f	0.3
Winding parameters	
Winding density ρ_w	8890 kg/m^3
Young's modulus E_w	10 GPa
Poisson ratio ν_w	0.34
Assumed values for press fit	
Interference δ	0.1% of R_{so}, 5 mm
Contact pressure penalty factor f_p	1
Static friction coefficient μ_s	0.2

5.2.1. Properties of laminations

Modeling laminations of electrical steel requires special attention, as they are transversely isotropic: they have different material properties in-plane than out-of-plane. While the in-plane properties are similar to isotropic electrical steel, the out-of-plane properties are very different. The exact mechanical properties, including the Young's modulus and the Poisson ratio, are usually hard to obtain, which leads to considerable uncertainty in the mechanical models of electrical machines [29, 60]. Numerically modeling the individual laminations would be computationally complex, which is why equivalent properties are generally used. A basic analytical way to obtain the equivalent properties of the compound material, consisting of sheets of electrical steel and an insulating resin, is applying the Rule of Mixtures with the properties of both raw materials. The resulting properties are only an approximation, but can serve as verification of other methods for determining the equivalent properties. This is partially caused by the fact that both the shaping method of the steel (punching, lasering) as well as the attachment method of the laminates (welding, bonding, fastening) influence the resulting material properties [6, 44, 56, 80, 83]. Large, modern machines usually employ laser cutting for shaping the laminations, and welding to stack the core [70].

A more accurate method is by determining the relevant parameters empirically. Static tests are not sufficient due to the non-linear behavior of the compound material, while ultrasonic tests determining the speed of sound in various directions within the material have proved more successful [29]. The most accurate method is using parameter fitting on a numerical modal analysis [29, 41, 60]. This method can be thought of as 'reverse modeling': both a Finite Element model as well as an experimental model is created, and the parameters of the FEM model are adjusted to fit the experimental results.

The properties shown in Table 5.1 are obtained from literature, including both reference parameters and experimentally determined parameters [29, 60, 75]. While it is certain that the out-of-plane stiffness is reduced, other parameters are harder to determine accurately. Especially ν_{zp} and G_{zp} vary significantly among different estimation methods, and the specific values are thus considered uncertain.

5.3. Analytical model

An analytical model to predict the structural response of the stator-frame system is unlikely to produce accurate results, which is why Finite Element Methods are usually employed [28]. This section describes two models that represent upper and lower bounds, to obtain rough estimates of the structural deflection.

5.3.1. Simple ring model

The simplest model neglects the impact of the frame, and holds only for the non-segmented case. In that case, the stator core can be approximated by a ring model with free-free boundary conditions [9, 28]. For large machines, this assumption can usually be made as the manufacturing tolerances are larger than the deflection of the stator, which means the mechanical coupling between the frame and stator is low [28]. Using this model, the quasi-static deflections due to forces of magnitude f_m with mode m are given by [9, 14]

$$Y_{0s} = \frac{R_{si} R_y f_0}{E_p h_{bi}} \tag{5.8}$$

$$Y_{ms} = \frac{12 R_{si} R_y^3 f_m}{E_p h_{bi}^3 (m^2-1)^2} \qquad \text{for } m \geq 2 \tag{5.9}$$

Quasi-static means that only the time-varying forces are considered, but that the effect of resonance is neglected. The latter equation shows that $Y \propto m^{-4}$, which indicates that the deflection decreases rapidly for increasing spatial orders. To find the dynamic deflections, an amplification factor is used, which amplifies the deflection when the excitation frequency ω is close to the natural frequency ω^*_{mn} of the m^{th} vibration mode:

$$\eta_m = \left[\left(1 - \left(\frac{\omega}{\omega^*_{mn}} \right)^2 \right)^2 + 4\zeta_m^2 \left(\frac{\omega}{\omega^*_{mn}} \right)^2 \right]^{-1/2} \tag{5.10}$$

This equation also shows that excitation frequencies below the eigenfrequency will result in a deflection close to the quasi-static deflection ($\eta_m \to 1$ for $\omega \ll \omega^*_{mn}$) while high excitation frequencies will not result in any deflections ($\eta_m \to 0$ for $\omega \gg \omega^*_{mn}$). It is thus preferable to increase the excitation frequencies to reduce deformations and noise [14].

There are several methods of calculating the natural frequencies, as discussed below. The modal damping coefficient ζ_m is generally hard to find[28] Empirical analysis shows that low damping can usually be assumed [29], and it is common to use a constant damping coefficient for all modes in the range of 2% [64, 75]. Some empirical estimates for a variable modal damping coefficient exist as well[84], such as Equation 5.11. This estimate agrees with $\zeta_m \approx 1-2$%.

$$4\pi^2 \zeta_m = 2.76 \times 10^{-5} \omega^*_m + 0.39 \tag{5.11}$$

The quasi-static deflection of the unsegmented stator core according to this method is shown in Figure 5.2, using the radial force harmonics found in Section 4.6. Even though this method is very simple, several observations can be made. Firstly, it shows the importance of the zeroth spatial order: while the amplitude of the time-varying component of the zeroth order is small compared to the other force harmonic, the deflection due to this mode is still dominant [72, 75]. Furthermore, due to $Y \propto m^{-4}$, only the lowest non-zero spatial harmonics play a considerable role in the deflection of the structure. For the unsegmented machine, this holds in particular for the slot harmonic at $m = 64$. The figure also shows the importance of the segment harmonic $m = 16$, as this becomes dominant for the segmented machine. Finally, it becomes clear that even though $m = 320$ and $m = 384$ are the strongest force harmonics, their impact on the deflection of the machine is minimal due to their high spatial order.

The assumption of a low coupling between stator and frame is likely to be invalid for a machine with stator segments pressed into the frame. It can be expected that most stiffness will come from the frame, while the stator segments mainly act as a distributed mass. In that case, a more accurate estimate of the structural response is given by the general expression of the deflection amplitude for mode m [28], rewritten from Equation 5.4:

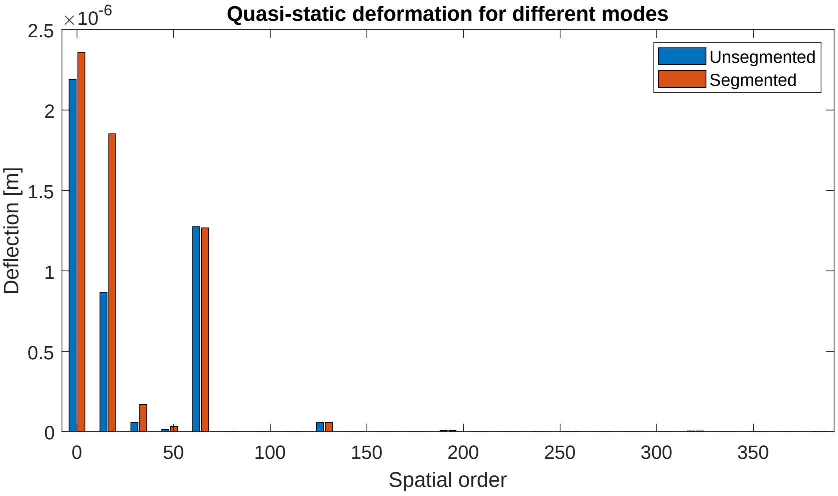

Figure 5.2: Quasi-static deformation due to force modes occurring

$$A_m = \frac{2\pi R_{si} L}{M(\omega^*_{mn})^2} f_{mn} \eta_m \tag{5.12}$$

which uses the same amplification factor η_m as given above. It is based on the total mass M and the natural frequency ω^*_{mn} of the stator-frame system. This natural frequency can be calculated with or without taking into consideration the stiffness of the stator. For the design using supports to constrain the stator segments, no analytical method has been found.

5.3.2. Eigenfrequency analysis

The eigenfrequencies of the stator can be found for only the stator core, or for the stator-frame system taking into account the support frame and the insulated windings [28]. When the stator is simplified to its back iron or yoke, the following equations for a long thin shell hold:

$$\omega^*_{mn} = \sqrt{\frac{K_{sm}}{M_s}} \tag{5.13}$$

$$K_{sm} = \frac{2\Omega_m^2}{R_y} \frac{\pi L h_{bi} E_p}{1-\nu_p^2} \tag{5.14}$$

$$M_s = k_{md} M_c \tag{5.15}$$

The frequency parameter Ω_m is found using Donnel-Mushtari's theory for the second-order equations of motion, dependent on the non-dimensional thickness parameter κ:

$$\Omega_m = \begin{cases} \frac{1}{2}\sqrt{(1+m^2+\kappa^2 m^4) \pm \sqrt{(1+m^2+\kappa^2 m^4)^2 - 4\kappa^2 m^6}}, & \text{if } m \geq 1 \\ 1 & \text{if } m = 0 \end{cases} \tag{5.16}$$

$$\kappa^2 = \frac{h_{bi}^2}{3(2R_y)^2} \tag{5.17}$$

The mass addition factor for displacement k_{md} takes into account the additional mass connected to the stator yoke with core mass M_c. If this is not taken into account, k_{md} is simply one. If the teeth mass M_t and insulated winding mass M_{wi} are included, this becomes

$$k_{md} = 1 + \frac{M_t + M_{wi}}{M_c} \tag{5.18}$$

The added stiffness of the teeth and windings is assumed to be small and thus neglected. The influence of the frame on the natural frequency of the stator-frame system depends on the coupling between the laminated core and the frame. If this is strong, for instance in the case of a press fit, the stiffness and mass of the stator and frame can be considered to be in parallel [28]:

$$\omega_{mn}^{*} = \sqrt{\frac{K_{sm} + K_{fmn}}{M_s + M_f}} \tag{5.19}$$

In this case, the assumption of analyzing the segments as a ring is expected to be more accurate, as the segments are tightly held in position. On the other hand, if the coupling is not rigid, either due to the mounting method or due to the deflections being small compared to the manufacturing tolerances of the stator-frame connection, the impact of the stator stiffness K_{sm} on the natural frequency of the system will be limited.

The stiffness of the frame is found using Equations 5.13 and 5.14 for the mean frame radius R_f, frame thickness h_f, frame length L_f and the Poisson ratio of the frame material ν_f, but in this case the nondimensional frequency parameter Ω_{mn} is found using the Donnell-Mushtari theory for the third-order equations of motion, to take into account the axial modes $n = 1, 2, 3$ [28]. For the characteristic equation (Equation 5.20), the constants are given by Equation 5.21, and it is solved using a numeric solver for Ω_{mn}^2.

$$\Omega_{mn}^6 - C_2\Omega_{mn}^4 + C_1\Omega_{mn}^2 - C_0 = 0 \tag{5.20}$$

$$\begin{aligned} C_2 &= 1 + \frac{1}{2}(3-\nu_f)(m^2+\lambda^2) + \kappa_f^2(m^2+\lambda^2)^2 \\ C_1 &= \frac{1}{2}(1-\nu_f)\left[(3+2\nu_f)\lambda^2 + m^2 + (m^2+\lambda^2)^2 + \frac{3-\nu_f}{1-\nu_f}\kappa_f^2(m^2+\lambda^2)^2\right] \\ C_0 &= \frac{1}{2}(1-\nu_f)\left[(1-\nu_f^2)\lambda^4 + \kappa_f^2(m^2+\lambda^2)^4\right] \end{aligned} \tag{5.21}$$

In these equations, the non-dimensional frame thickness κ_f^2 is calculated using Equation 5.17, and the parameter λ depends on the boundary conditions of the axial ends of the frame. If these are simply supported, λ is calculated for different axial orders n using Equation 5.22. If they are both clamped, λ is replaced by Equation 5.23 which takes into account the “effective length”.

$$\lambda = n\pi\frac{R_f}{L_f} \tag{5.22}$$

$$\lambda_e = n\pi\frac{R_f}{L_f - L_0} \qquad \text{with} \qquad L_0 = L_f\frac{0.3}{n+0.3} \tag{5.23}$$

The relevant resulting natural frequencies are shown in Table 5.2. As discussed above, the deflection of mode m is strongly increased if the excitation frequency of the radial force f_{mn}, discussed in Chapter 4, is close to the corresponding natural frequency. As the excitation frequencies were calculated for the nominal rotational speed, the force orders can occur at all frequencies below the given values. This means that if the natural frequency is below or close to the frequencies presented in Chapter 4, the system is at risk of resonance. From these results presented in the table, several points can be observed:

- According to this simplified analysis, the stator core does not contribute significantly to the stiffness of the structure, except for the stiffness of the breathing mode.
- The breathing mode and the 16th radial order are at risk of excitation, as the natural frequencies are close to $6\omega_e = 160$ Hz and $2\omega_e = 53$ Hz respectively.
- Although the force harmonics $m = 320$ and $m = 384$ are the strongest in this machine, they are unlikely to cause any significant deformation in the structure due to their small quasi-static deflection and the high natural frequency of the corresponding mechanical modes.
- The breathing mode is not at risk of excitation by the time harmonics of the Power Electronic Converter, due to the relatively high switching frequency. The $2p$ force order is also not at risk of excitation, due to the very high natural frequency. The $2F_1 = 64$ force harmonic is relatively close to the switching frequency, and should be studied in more detail.

Table 5.2: Analytical natural frequencies of the stator system in Hz

Mode (m,n)	Unsegmented core	Frame	Coupled core and frame	System, neglecting core stiffness
$(0,1)$	126	168	128	99
$(1,1)$	0.17	167	98	98
$(2,1)$	0.86	163	96	96
$(16,1)$	62	181	114	106
$(32,1)$	247	554	363	326
$(48,1)$	555	1211	799	713
$(64,1)$	986	2304	1447	1297
$(320,1)$	25×10^3	78×10^3	48×10^3	46×10^3
$(384,1)$	34×10^3	102×10^3	64×10^3	60×10^3
$(0,2)$	126	226	156	133
$(1,2)$	0.17	226	133	133
$(2,2)$	0.86	226	133	133
$(16,2)$	62	298	180	176
$(32,2)$	247	668	424	393
$(48,2)$	555	1330	862	783
$(64,2)$	986	2335	1516	1374
$(320,2)$	25×10^3	78×10^3	48×10^3	46×10^3
$(384,2)$	34×10^3	102×10^3	64×10^3	60×10^3
$(0,3)$	126	368	231	216
$(1,3)$	0.17	368	217	216
$(2,3)$	0.86	369	217	217
$(16,3)$	62	298	180	176
$(32,3)$	247	846	523	498
$(48,3)$	555	1518	964	984
$(64,3)$	986	2545	1630	1499
$(320,3)$	25×10^3	78×10^3	49×10^3	46×10^3
$(384,3)$	34×10^3	102×10^3	64×10^3	60×10^3

Using these eigenvalues, the quasi-static defection according to Equation 5.12 can be calculated. This is shown in Figure 5.3, including a representation of the deflection along the circumference, magnified a million times. The figure again shows the dominance of the breathing mode, as well as the 16th and 64th deflection mode.

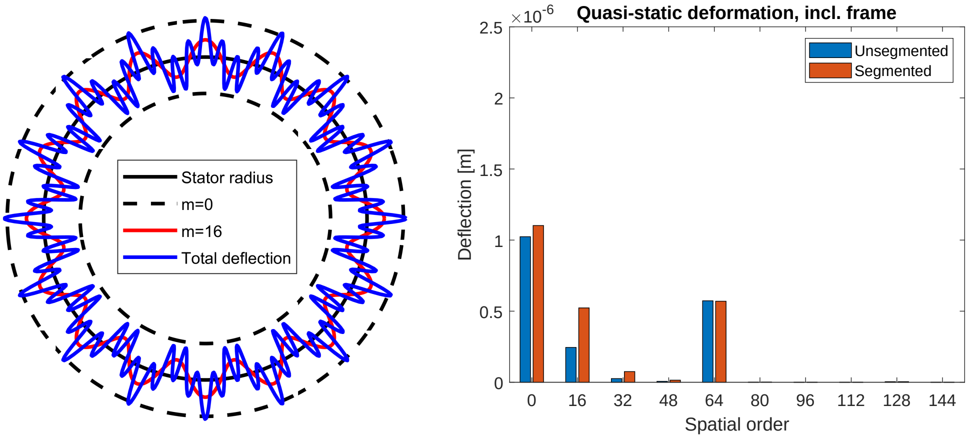

(a) The deflection of the stator system, magnified 10^6x

(b) Contribution of different modes

Figure 5.3: Quasi-static deflection according to Equation 5.12

5.4. Other vibrations modes

As discussed in Section 2.3, this analysis focuses on the vibrations resulting from the electromagnetic fields, while vibrations resulting from other mechanical components and the load are neglected. Two other types of vibrations caused by the force harmonics have been neglected as well: tangential modes and rotor modes.

So far, all considered vibrations are caused by the radial force harmonics. The most important vibration caused by the tangential force harmonics, besides torque pulsations, is tooth rocking. In this vibration mode, primarily caused by the $m = N_s/2 = 192^{th}$ harmonic, causes teeth to be moving back and forth tangentially [13]. As these vibrations occur at a very high frequency, and are expected to be damped by the insulated windings inside the slots, they are neglected in this analysis.

Furthermore, the calculated forces lead to different vibrations modes in the rotor structure as well. As the focus of this thesis is on the stator structure, and the coupling between the rotor and stator vibrations is small [41], these modes have not been studied in this thesis.

5.5. Summary

An analytical model for the eigenfrequencies of the structure has been set up by simplifying the stator and frame to simple ring structures. The stator core has relatively low eigenfrequencies, and most stiffness is expected to come from the frame. Based on this initial analysis, it was found that a few forces and vibrations dominate the mechanical response:

- The breathing has significant deflections even for a very low force amplitude, and is at risk of resonance due to the natural frequency being close to the $6\omega_e = 160$ Hz, the predicted excitation frequency
- The 16th vibration mode is important, as deflections with the lowest spatial order lead to larger deflections ($Y \propto m^{-4}$). It is at some risk of resonance, especially for the frameless case.
- The 64th vibration mode is important, due to the combination of a large force amplitude and a relatively low spatial order. It is at some risk of resonance due to the switching frequency of the PE converters at $f_s = 1040$ Hz.

It was also found that the mechanical analysis faces considerable uncertainty, especially regarding the modeling of the laminated cores and the estimate of the damping coefficients.

6

Numerical analysis

In order to verify the analytical approach that was set up in Chapters 4 and 5, a numerical analysis is performed in COMSOL, a multiphysics Finite Element tool. In reality, the electromagnetic and mechanical are coupled in two directions. Electromagnetic effects change the mechanical properties of the structure, as the change in air gap reluctance affects the stiffness and eddy currents affect the damping coefficients due to energy dissipation [41]. At the same time, the magnetic field distribution is changed by the deformation of the rotor and stator.

Because the overall effect of this coupling is limited, the electromagnetic and mechanical simulations are separated, and a staggered analysis approach is taken [41]. The electromagnetic analysis is performed in 2D, assuming the magnetic forces are constant along the axial length of the machine, and the resulting forces on the inner stator radius are exported. These forces are then applied to a mechanical 3D model to take into account the coupling of radial and axial vibration modes [28].

6.1. Electromagnetic model in COMSOL

The generator is modeled in COMSOL using the “Rotating Machinery, Magnetic” module to verify the analytical design discussed in Chapter 3 and the field and force models of Chapter 4. The machine is modeled in 2D, which assumes a constant magnetic field along the axis of the machine and neglects certain 3D effects, such as the end winding losses and the impact of skewing.

There are two main ways of analyzing the input and output of an electrical machine: one involves modeling an external electrical circuit, the other supplies the windings with a voltage or current directly. In the first case, the circuit can be modeled using the Electric Circuit module of COMSOL, which uses a lumped parameter model defined by a Spice-like node list. The advantage of this approach is that the impact of the end winding inductance (L_e) can be included, and that different load types can be analyzed. Resistive, capacitive or inductive loads have different effects on the resulting vibrations in the machine [73, 76]. Furthermore, the current harmonics resulting from the harmonics in the induced voltage can be analyzed.

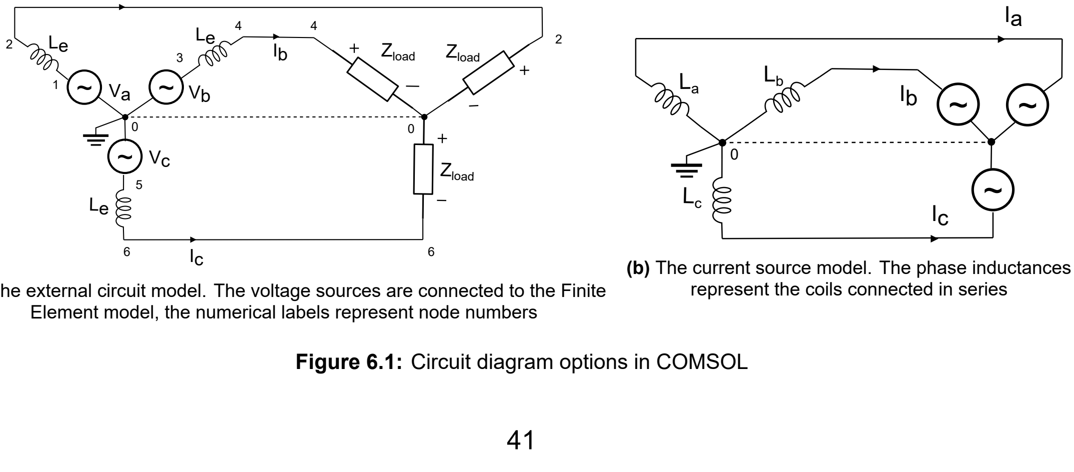

(a) The external circuit model. The voltage sources are connected to the Finite Element model, the numerical labels represent node numbers

(b) The current source model. The phase inductances represent the coils connected in series

Figure 6.1: Circuit diagram options in COMSOL

The downside of this approach is that there is no direct control over the current, if the controller of the converter is not modeled. For simplicity, the current in the coils is set directly, in order to apply zero d-axis current control in a simple way. This model is used to perform a time-stepping Finite Element Analysis over one electrical period. By running over a longer time-span, initialization errors that generally occur [2] are mitigated, at the expense of a longer computation time.

6.1.1. Modeling approach

The same dimensions as shown in Table 3.2 are used. Using periodic conditions, only one section needs to be modeled to analyze the entire machine. In this specific case, that would mean modeling a sections with 12 slots and 10 poles, corresponding to half a segment. However, in order to be able to model the gaps between the segments, one full segment is modeled, with a periodicity condition equal to $N_{seg} = 16$. The segment is divided in 4 domains, as shown in Figure 6.2, which are modeled using the methods presented in Table 6.1.

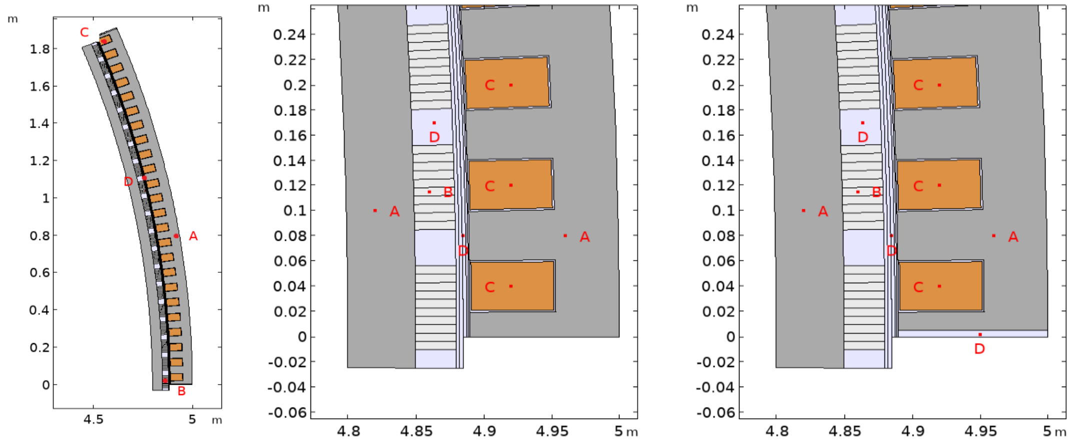

(a) Overview

(b) Close up of the usegmented machine

(c) Close up of the segmented machine

Figure 6.2: Modeling domains used in COMSOL

Based on this geometry, a triangular mesh is built. Special attention is paid to the mesh in the air gap: firstly, an equidistant distribution is defined on one of the edges of the identity boundary pair, and copied to the other edge. This aligns the nodes of the rotating and stationary domain at their intersection. In the time-stepping analysis, the time step is defined in such a way that a node on the rotor edge always aligns with a node on the stator edge, creating a clean mesh for each time instant. Secondly, the same edge is copied to the other edges in the air gap, to create a regular mesh as shown in Figure 6.4.

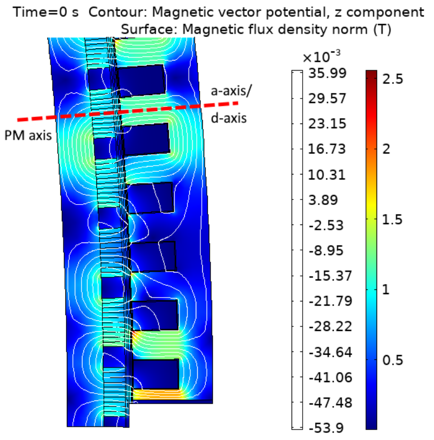

Figure 6.3: Alignment of axes at $t = 0\ s$

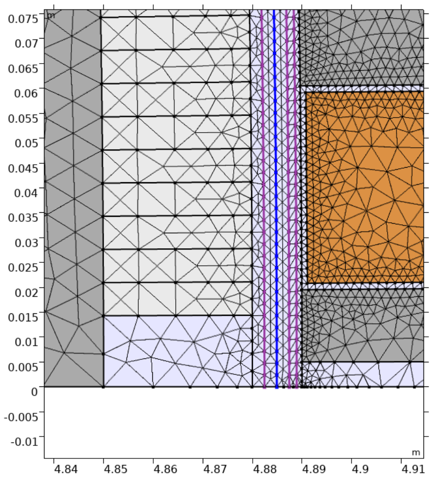

Figure 6.4: Close-up of mesh in the air gap

Table 6.1: The domains and edges used in COMSOL

Label	Domain	Modeling approach
A	Laminated steel	The stator and rotor cores are modeled as electrical steel, with its electrical conductivity assumed to be 0 S/m. A B-H curve is defined to simulate saturation in the core, a shown in the figure below. 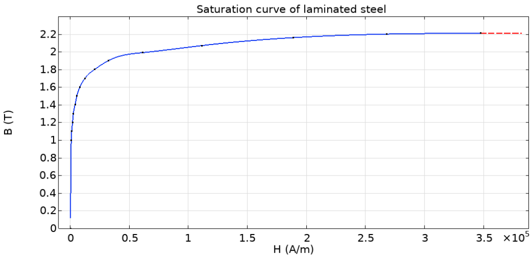
B	Permanent magnets	The magnets are defined by means of their remanent flux density of 1.2 T in either positive or negative radial direction. Losses caused by eddy currents are neglected by setting the conductivity to zero. To model the losses more accurately, they should be modeled as segmented magnets which are insulated from each other [50].
C	Copper windings	The coils are modeled as three coil group of homogenized multiturn conductors, with the winding pattern as defined in Table 3.3 repeating twice. The conductivity of the copper is set to 3.8×10^7 S/m. The d and q currents are defined as input variables, and transformed to phase currents using the Park transformation (Equation 4.20) with the convention that $i_a = 0$ at $t = 0$.
D	Air gap & insulation	The insulation between the coils and the core, the air gap and the gap between the segments is modeled as air. The air gap is split in multiple layers, to analyze the flux and force densities at different radial positions. The layers include one line in the middle of the air gap, and one very close to the stator teeth to analyze the impact of slots on the magnetic flux density.
	Boundaries	• The inner circumference of the rotor and the outer one of the stator are modeled as magnetically insulated boundaries, as well as the stator boundaries next to the segment gap. • A periodic continuity condition is applied to the radial edges of both the stator and rotor • An Identity Boundary Pair is defined in the center of the air gap, an interface between the stationary and the rotating domain. This applies a continuity condition to the magnetic field, coupling the two domains. Furthermore, a Sector Symmetry continuity is defined on this identity boundary pair, with a periodicity equal to the number of segments.
	Rotating domain	A moving mesh is applied to the rotor and the inner half of the air gap. A rotating domain with a fixed rotational velocity is specified, with an initial position chosen such that a north pole aligns with the axis of phase A. Together with the definition of the phase currents, this aligns the rotor with the d-axis of the machine, as shown in Figure 6.3.

6.2. Numerical analysis of fields and forces

The numerical models are used to analyze the machine performance and find the resulting force harmonics. In the following section, the results obtained from the segmented and non-segmented model are compared to each other and to the analytical model presented before.

6.2.1. Machine parameters

The coil resistance calculated by COMSOL is $0.165\ \Omega$ for the segmented and unsegmented machine, which agrees well with the analytical slot resistance calculated in Chapter 3. As the machine is modeled in 2D, the end-winding resistance is not taken into account by the numerical model, underestimating the coil resistance by at least 15%. The machine inductance is calculated by setting a DC current to one phase only, and by disabling the permanent magnets. The inductance of phase i is then calculated by dividing the flux linkage by the current of the same phase:

$$L_{ph,i} = \frac{\lambda_i}{I_i} = 1.6\ H \tag{6.1}$$

This value is calculated for the entire machine and is the same for both the unsegmented and the segmented machine, which thus has an inductance of $0.1\ H$ per segment, 10% lower than the analytical value. The mutual inductance between phase i and j is calculated by dividing the flux linkage of phase j by the current applied to phase i:

$$M_{ij} = \frac{\lambda_j}{I_i} \tag{6.2}$$

For the unsegmented machine, all mutual inductances are $1.2\ mH$, equal to $75\ \mu H$ per segment. This is very low, as expected from a machine with non-overlapping windings. For the segmented machine, the mutual inductances per segment are different:

$$\begin{bmatrix} L_a & M_{ab} & M_{ac} \\ M_{ba} & L_b & M_{bc} \\ M_{ca} & M_{cb} & L_c \end{bmatrix} = \begin{bmatrix} 0.1\ H & -19\ \mu H & 169\ \mu H \\ -19\ \mu H & 0.1\ H & 169\ \mu H \\ 169\ \mu H & 169\ \mu H & 0.1\ H \end{bmatrix} \tag{6.3}$$

In this specific design, the segment gap is located between a coil of phase a and a coil of phase b, which explains the reduction of the mutual inductance between these two phases. Due to the change in the flux path of the armature reaction, shown in Figure 6.5, the other mutual inductances are increased.

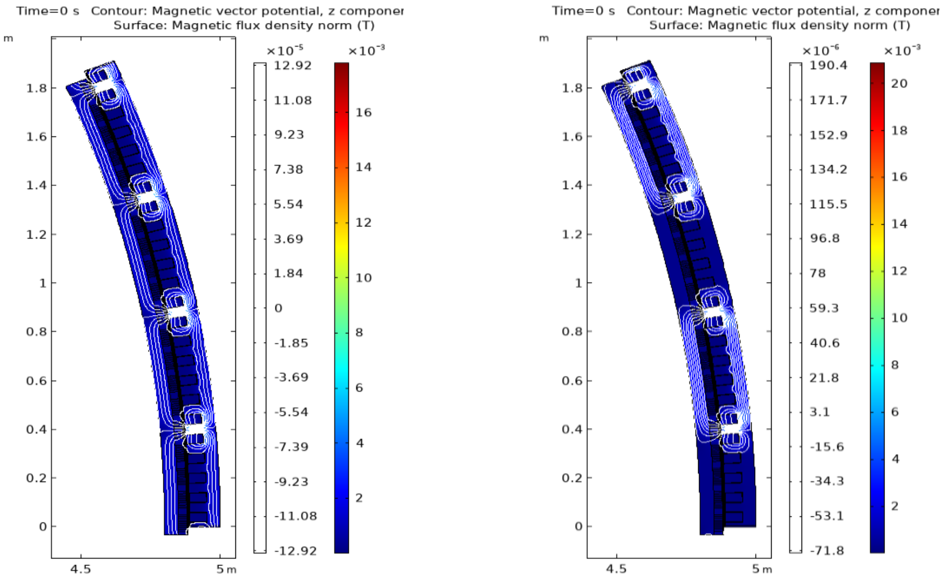

(a) The unsegmented model

(b) The segmented model

Figure 6.5: The flux pattern of the armature reaction when a current is applied to phase a

6.2.2. Flux density and induced voltage

The model is then used to analyze the magnetic flux density in the no-load and loaded case. The radial and tangential component are calculated from the Cartesian components at an edge in the air gap, very close to the inner stator radius:

$$\begin{aligned} B_r &= B_x \cos\theta + B_y \sin\theta \\ B_t &= -B_x \sin\theta + B_y \cos\theta \end{aligned} \tag{6.4}$$

The results of the segmented machine, including their spatial FFT, are shown in Figure 6.6 and 6.7. The x-axis is shifted such that the line graphs start at the axis of phase a, in order to make the comparison with the analytical results easier. The results of the unsegmented machine are nearly identical.

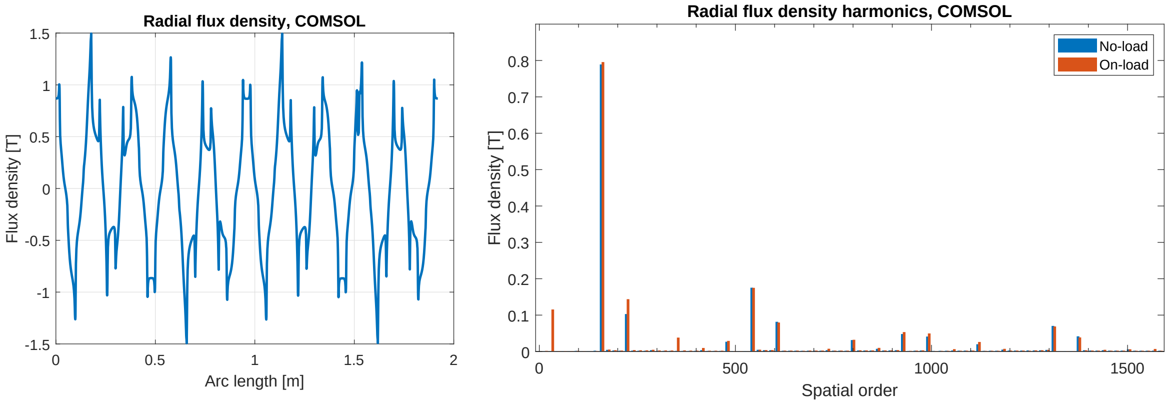

(a) Along the circumference, $t = 0\ s$

(b) The spatial orders

Figure 6.6: The radial flux density for a slotted stator segment, obtained from COMSOL

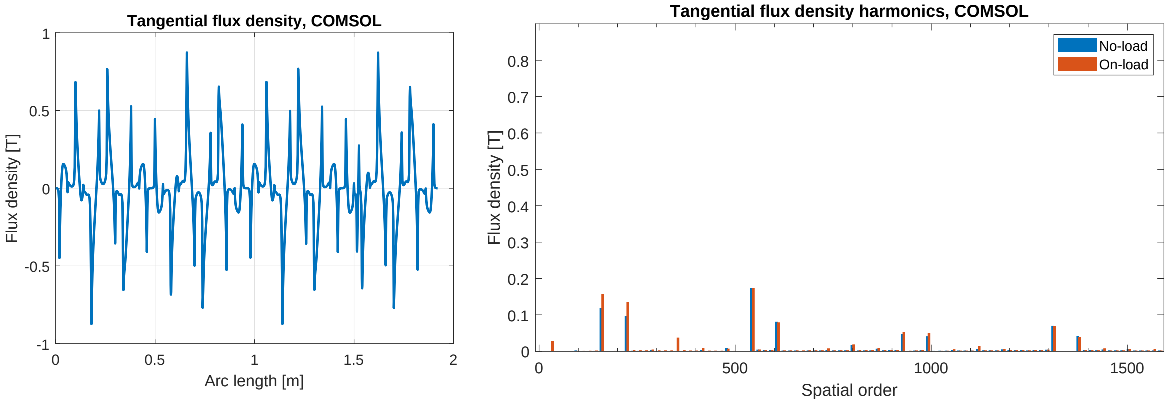

(a) Along the circumference, $t = 0\ s$

(b) The spatial orders

Figure 6.7: The tangential flux density for a slotted stator segment, obtained from COMSOL

The numerical results agree well with the analytical results. The dominant flux harmonics occur at odd multiples of $p = 160$, with additional harmonics occurring at $|\mu p \pm iN_s|$ due to the slots. The armature reaction adds a low subharmonic at $F_1 = 32$ as expected. The main difference is that the tangential flux density shows a spatial harmonic at $p = 160$ even in the no-load case, which is not predicted by the analytical model. This can be explained by the fact that the flux densities are obtained just below that stator edge, while the analytical method predicts $B^{PM}_{t,slotless}(R_{si}, \theta) = 0$ at exactly the stator edge.

The resulting induced voltage in the no-load case is shown in Figure 6.8. It shows a sinusoidal voltage with an RMS value of 2.5 kV per segment, close to the expected value from the analytical model.

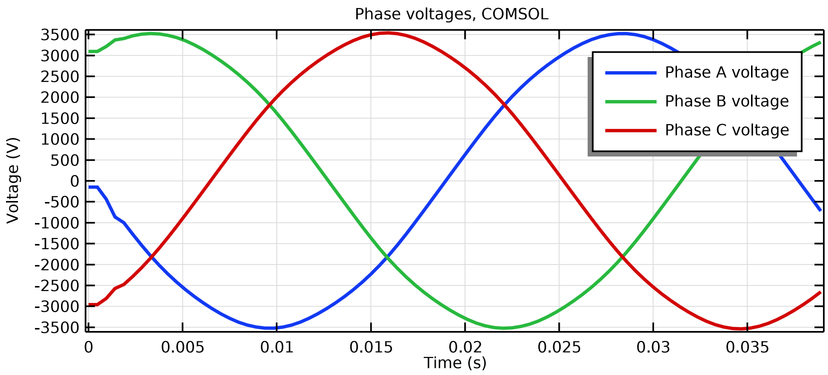

Figure 6.8: Induced voltage obtained from COMSOL

6.2.3. Torque and power

In theory, the 2D torque of an electrical machine could be calculated in the same way as described in the analytical method, by directly integrating the tangential force times the radius (the arm of the moment) along a line in the air gap. Using the tangential force from Maxwell's stress tensor, this gives:

$$T_e = \frac{L}{\mu_0} \int_0^{2\pi} r^2 B_r B_t \, d\theta_s \tag{6.5}$$

However, when using finite element analysis, this often proves inaccurate due to approximation errors. An improved equation can be derived, based on the knowledge that the torque should be independent of the radius r chosen between the inner and outer air gap radius in the above equation [3]. This leads to a surface integral, often referred to as Arkkio's method:

$$T_e(r_{out} - r_{in}) = \int_{r_{in}}^{r_{out}} T_e \, dr = \frac{L}{\mu_0} \int_{r_{in}}^{r_{out}} \left(\int_0^{2\pi} r^2 B_r B_t \, d\theta_s \right) dr \tag{6.6}$$

$$T_e = \frac{L}{\mu_0 (r_{out} - r_{in})} \int_S r B_r B_t \, dS \tag{6.7}$$

Where S represents (a part of) the cross-sectional area of the air gap. This method has been applied in COMSOL, with the only difference to Arkkio's original method being the integration boundaries of r [54]. Instead of integrating over the entire air gap, the torque is only integrated over the inner half of the air gap, and thus over the rotating part of the mesh.

The cogging torque is calculated by using Arkkio's method in the no-load case, and shown in Figure 6.9. The unsegmented models shows a cogging torque of 4 kN at 12 times the electrical frequency,

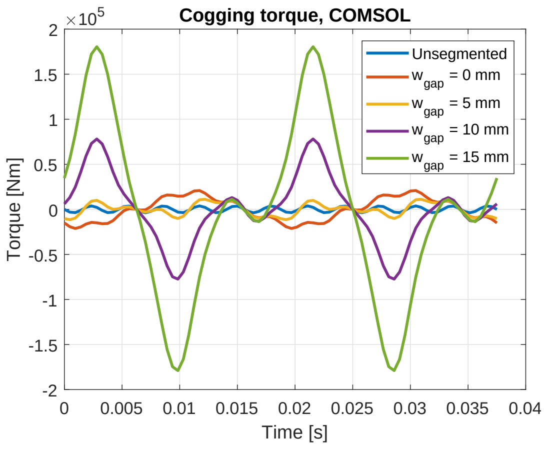

Figure 6.9: The cogging torque as obtained from COMSOL

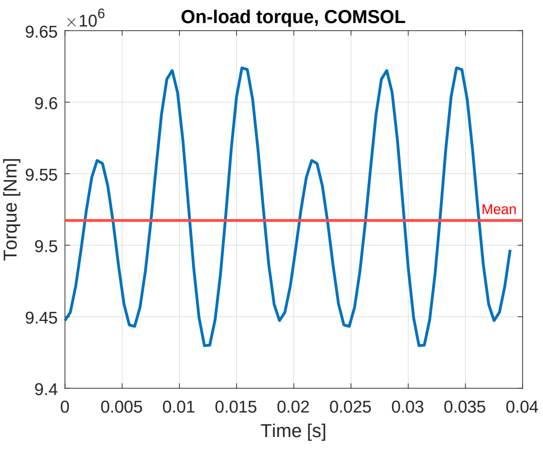

Figure 6.10: The on-load torque as obtained from COMSOL

which is 50% lower than predicted by the analytical model. As the cogging torque was the main force affected by the segment gap, it is plotted for multiple gap widths in Figure 6.9. It shows that the cogging torque is significantly increased due to segmentation, but two different effects can be observed. First of all, even for an infinitesimally small gap, the cogging torque is increased due to the insulated flux barrier. Secondly, the cogging effect becomes stronger for wider gaps as predicted by the analytical model, but this produces torque in the opposite direction than the first effect. This explain why the cogging torque is very small for $w_{gap} = 5$ mm, as the two effects counteract each other. Both effects occur at twice the electrical frequency, as predicted by the analytical model.

The on-load torque is shown in Figure 6.10. It shows a constant torque of 9.52 MNm, almost the same as the design torque of 9.55 MNm. The torque ripple occurs at 6 times the electrical frequency, as predicted by the analytical model, and has an amplitude of 100 kNm, 1% of the nominal torque.

The power of one segment is shown in Figure 6.11. The mechanical power refers to the torque multiplied by the rotational speed, while the segment power refers to the sum of the power generated by the three phases. It shows that the mechanical power is close to the design power of 10 MW divided over 16 segments. The model shows losses of 35 kW per segment, resulting in a total output power of 9.4 MW. This only includes the 2D resistive losses, and neglects end winding losses. The electrical power of the machine is produced with a power factor of 0.85, as expected from the calculations in Section 3.3. Finally, w_{gap} was not found to influence the output power of the machine.

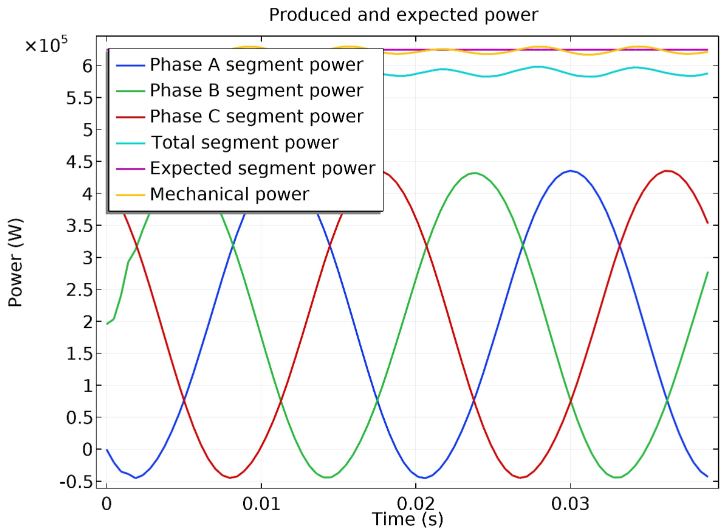

Figure 6.11: The power per segment as obtained from COMSOL

6.2.4. Force harmonics

The resulting instantaneous forces are calculated using Maxwell's Stress Tensor in COMSOL, and the FFT of the radial and tangential components are shown in Figures 6.12 and 6.13. The results agree well with those obtained from the analytical method, and show a rich harmonic spectrum with peaks at the spatial orders equal to the pole number and odd multiples of N_s, the slot harmonics. The variation in the average radial force, the zeroth radial order, has also been confirmed to be less than 2 kN/m^2, similar to the analytical result.

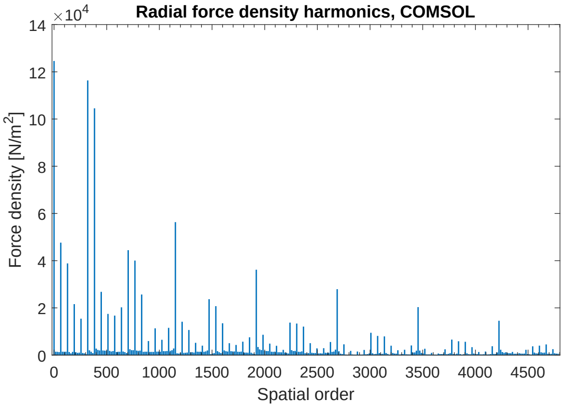

Figure 6.12: The harmonics of the radial force, obtained from COMSOL

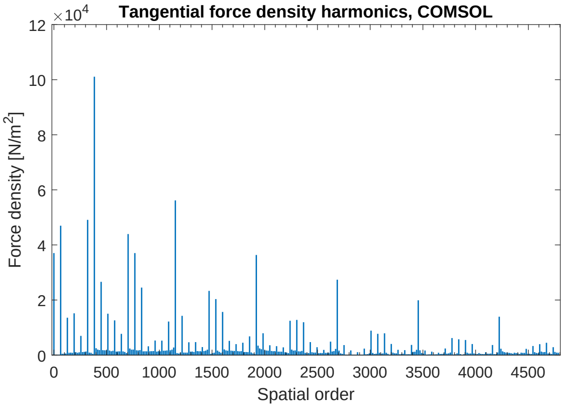

Figure 6.13: The harmonics of the tangential force, obtained from COMSOL

The effect of segmenting the stator on the force harmonics is shown in Figure 6.14. It confirms the increase of force orders at multiples of $N_{seg} = 16$, the segment harmonics, but shows a significantly stronger effect than predicted by the analytical method. Upon closer analysis, it was found that the armature reaction increased several low spatial orders in the magnetic flux density at multiples of 16 more strongly than predicted by the analytical model.

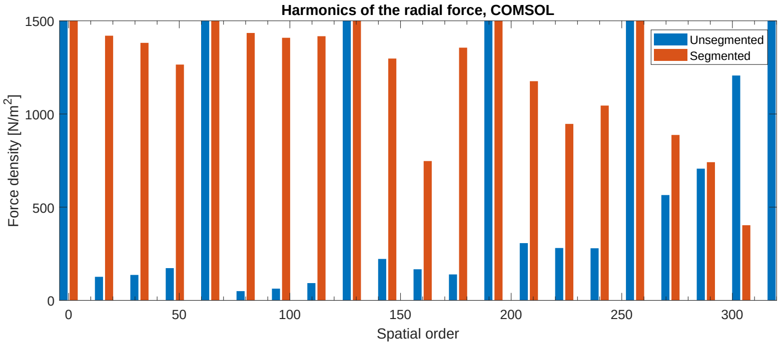

Figure 6.14: The lower orders in the radial force

6.3. Mechanical 3D model

As a next step, the structure of the generator is modeled in 3D, and its eigenmodes are studied numerically. Estimating the eigenfrequencies and the mechanical deflections are the hardest steps in analyzing vibrations and noise in electrical machines [28]. Finite Element Analysis can take more complex shapes and anisotropic materials into account, but many uncertainties remain. Especially damping parameters are hard to determine, while they have an important impact on the resulting vibrations and noise. The accuracy of numerical models can be improved by validating these uncertain parameters with experimental models, as will be described in Chapter 7.

In this section, a numerical model of the structure will be described, using the same parameters as in Chapter 5 given in Table 5.1. It is analyzed in COMSOL, using the Structural Mechanics Module in 3D to take into account axial deformation. Using this module, transverse isotropic materials can be modeled as orthotropic materials, which have different properties in 3 orthogonal directions [16].

By defining the z-axis as the axial direction of the machine, the following material properties can be defined:

Orthotropic	Transverse isotropic
E_x, E_y	E_p
E_z	E_z
ν_{xy}, G_{xy}	ν_p
$\nu_{yz}, \nu_{xz}, G_{yz}, G_{xz}$	ν_{zp}, G_{zp}

By using orthotropic materials and non-linear connections between components in 3D, the numerical models become large and computationally complex. Using symmetry, it is possible to analyze only a section of the model, in one of two ways:

- By using plane symmetry, a quarter of a full circle can be analyzed, corresponding to 4 segments. By combining symmetric and anti-symmetric boundary conditions, all eigenmodes of the full model can be found. Figure 6.15 shows two examples: $m = 8$ can be found by using symmetric-symmetric boundary conditions on the quarter-circle, while $m = 5$ can be found by using symmetric-asymmetric boundary conditions.
- By using cyclic periodicity conditions, one segment can be analyzed. This will only provide eigenmodes which repeat every segment, or in other words, only radial modes m at multiples of N_{seg} are found. As these are the most important due to the force orders occurring at multiples of N_{seg} as well, this method is still useful.

Both types of symmetry have been used in the following analysis, and have been verified with a full model.

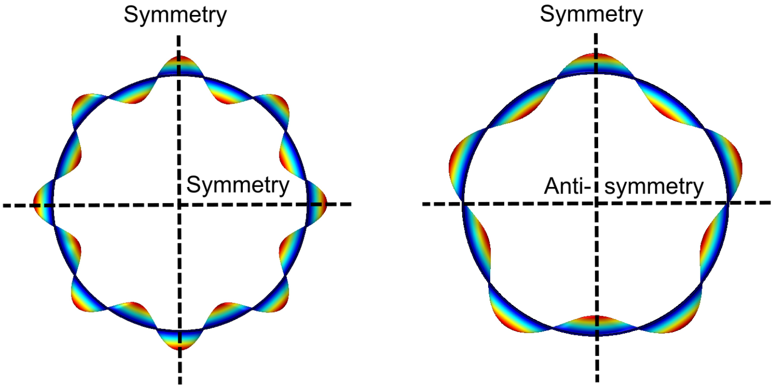

Figure 6.15: Two types of plane symmetry used to find all eigenmodes of the full ring

6.3.1. Ring models

To verify the analytical and numerical approach, first two simple models are analyzed in COMSOL. The first one is the simplest, and represents the frame with clamped ends and an isotropic material. The results are shown in Table 6.2, at the end of this section. The found eigenfrequencies are 5-10% higher than those predicted by the analytical model, but overall agree well. The breathing mode has a similar eigenfrequency as the first, second and 16th mode, and the eigenfrequencies of other modes increase with their axial and radial order.

Secondly, the unsegmented stator core with an orthotropic material model and free-free boundary conditions is analyzed. The results agree with the analytical model regarding the breathing mode, the very low eigenfrequencies for the second radial order, and the overall low eigenfrequencies compared to the frame. However, the analytical model appears to underestimate the stiffness of the stator core, and thus its eigenfrequencies. This is possibly caused by neglecting the added stiffness of the teeth in the analytical model.

Due to the simplicity of the two models, all observed eigenmodes were clearly recognizable, as shown in Figure 6.16. However, several modes were not observed in the results, and were left open in Table 6.2. Especially the high spatial orders could not be recognized.

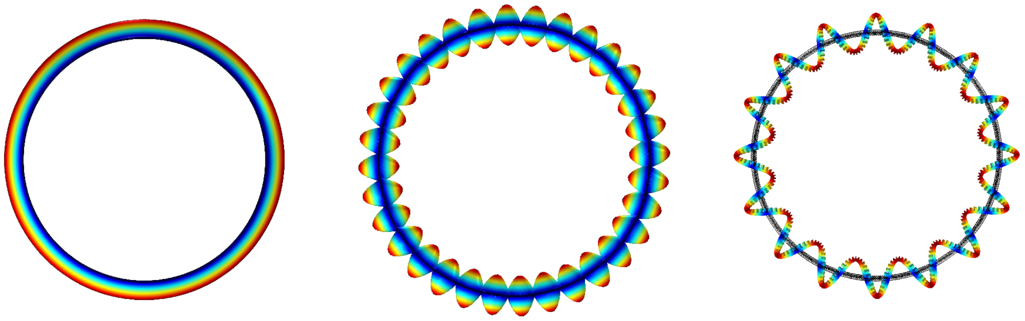

Figure 6.16: Examples of eigenmodes: (0,1) for the frame, (16,2) for the frame and (16,1) for the core.

6.3.2. Interference fit

The interference fit design is modeled in COMSOL using a contact pair with friction. The stator core and the frame are first modeled with a small overlap, the interference δ. The contact surfaces are then defined as Contact Pair, with the frame as source and the core segment as destination, to which a Contact condition with friction is applied. The contact stiffness is defined by an automatic penalty factor f_p[16], and the friction force by a static friction coefficient μ_s. The assumed values for δ, f_p and μ_s are given in Table 5.1, and the effect of changing these values will be discussed in Section 6.3.4.

When the geometry and physics are defined, a static analysis is performed while setting the 'previous state' to 'in contact'. This calculates the required static deformation of both components and the resulting reaction forces, shown in Figure 6.17. Then, this deformed state is used as initialization point for the eigenfrequency study. Due to the non-linearity of the contact analysis, the computational complexity is significantly increased compared to the simple numerical ring models. This makes the use of symmetry and periodicity a necessity.

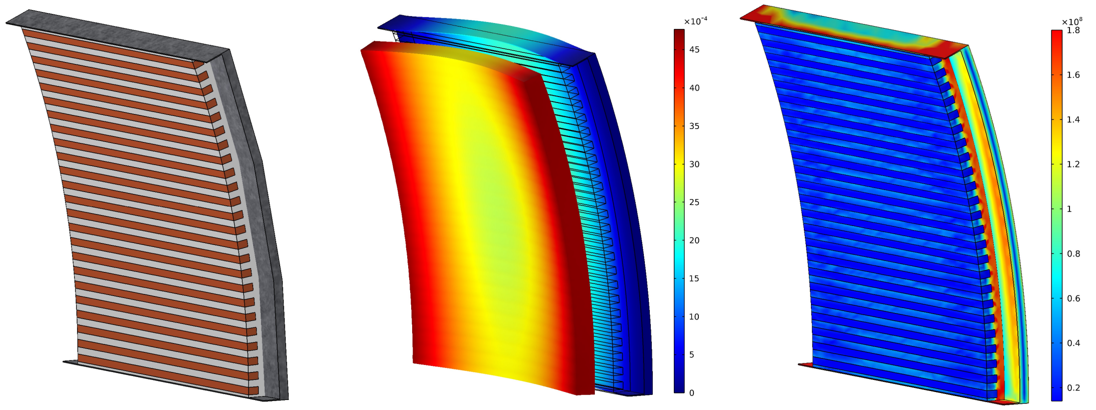

(a) Overview **(b)** Static deformation, magnified [m] **(c)** Von Mises Stress [Pa]

Figure 6.17: Modeling of a press fit, using periodicity constraints

Figure 6.17 shows the static analysis: the structure bulges outward, and experiences a stress in the order of 100 MPa. Results of the eigenfrequency analysis are shown in Table 6.2, and again the high spatial orders were not observed. The eigenfrequencies are close to those found for the support frame alone, suggesting the design obtains most of its stiffness from the frame. It also means the much simpler frame model is sufficient to obtain an accurate estimate of the eigenfrequencies of the stator-frame system. The numerical eigenfrequencies are higher than the analytical results obtained for the coupled core and frame, which can be explained by the underestimation of the stator core stiffness.

6.3.3. Supported segments

To study the second design, in which there is an air gap between the stator segments and the support frame, three different models are considered: a free-floating segment, a segment with two supporting beams, and a segment with 3 supporting beams, all with copper windings attached to them. The models are shown in Figure 6.18. The beams are placed in the back iron in between two coils to reduce the effect on the magnetic fields, and are assumed to be fixed and rigid. The results are again shown in Table 6.2. For this design, only modes at multiples of N_{seg} are defined.

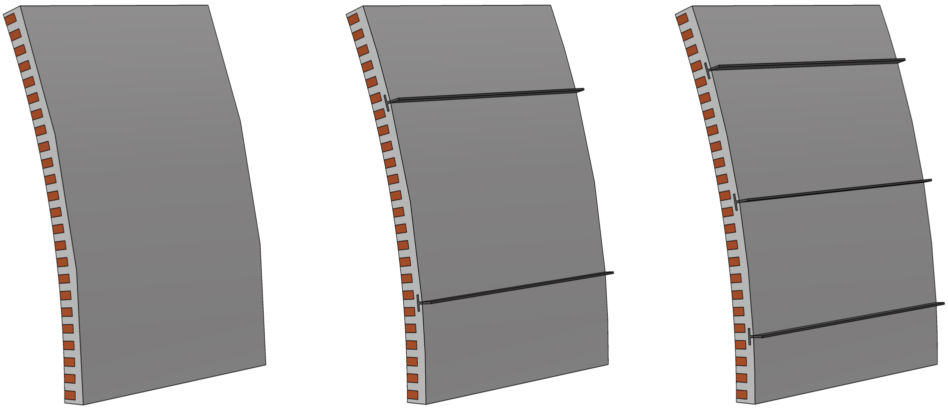

(a) Free-floating **(b)** 2 support beams **(c)** 3 support beams

Figure 6.18: Models of the supported segment design

A few conclusions can be drawn from these calculations:

- Overall, the found eigenfrequencies of the supported segments were lower than those found for the press fit, due to the low stiffness of the stator core. However, the eigenfrequencies are not below the excitation frequencies, and thus do not make the design infeasible
- By using a supporting beam along the axial length of the segment, the mechanical breathing mode is eliminated
- Due to the spacing of the supporting beams, some eigenmodes are magnified while others are reduced. For example, the 2-beam design has a very low eigenfrequency for the 16th order, as the beams are placed exactly at the neutral points of the deformation, as shown in Figure 6.19.

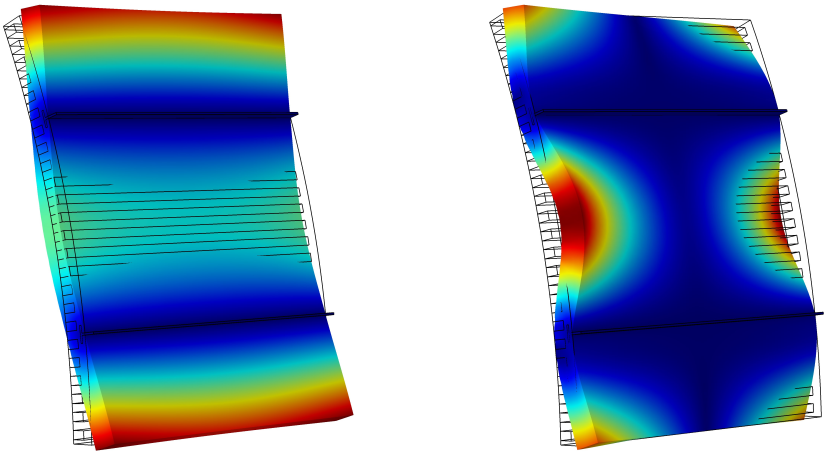

(a) $m = 16, n = 1$ **(b)** $m = 32, n = 2$

Figure 6.19: Examples of eigenmodes of the segment supported by 2 beams

Table 6.2: Numerical natural frequencies of the stator system in Hz

Mode (m, n)	Unsegmented core	Frame	Press fit	Segment incl. windings	Segment, 2 beams	Segment, 3 beams
$(0, 1)$	127	182	147	108		
$(1, 1)$		179	140	Not defined	Not defined	Not defined
$(2, 1)$	1	171	127	Not defined	Not defined	Not defined
$(16, 1)$	95	194	178	74	90	238
$(32, 1)$	372		573	366	235	397
$(48, 1)$	804	1229	1276	787	745	589
$(64, 1)$	1353	2120	1880	1211	976	1072
$(0, 2)$	127		239	273		
$(1, 2)$	119		236	Not defined	Not defined	Not defined
$(2, 2)$	108	263		Not defined	Not defined	Not defined
$(16, 2)$	104	328	283	95	105	244
$(32, 2)$	380	665	625	371	232	395
$(48, 2)$	811	1336	1212	763	742	
$(64, 2)$	1359		1891	1215	951	
$(0, 3)$	188	434	394	504		
$(1, 3)$		434	395	Not defined	Not defined	Not defined
$(2, 3)$		434		Not defined	Not defined	Not defined
$(16, 3)$		527	451	180	186	306
$(32, 3)$	429	886	756	451	288	
$(48, 3)$	847	1514	1280	960	916	
$(64, 3)$	1387		1955	1279	1228	1148

6.3.4. Sensitivity analysis

As several parameters are hard to determine without experimental validation, a sensitivity analysis is performed to estimate the uncertainty of the models. The considered parameters include the axial material properties of the laminated steel, G_{zp} and ν_{zp}, the press fit interference δ, and the press fit modeling parameters μ_s and f_p. The sensitivity analysis is performed for the press fit model by doubling or halving one of the parameters, and calculating the average change in eigenfrequencies. The results are shown in Table 6.3, in which a positive percentage indicates an increase in eigenfrequencies when the studied parameter is doubled.

Parameter	Average change	Comments
G_{zp}	1%	Uncertainty range: [5 - 30 GPa]
ν_{zp}	0%	Uncertainty range: [0.05 - 0.15]
δ	3%	Design range: 0.05% to 0.2% of R_{so}
μ_s	2%	Steel-steel friction range: [0.2 - 0.8]
f_p	1%	Model becomes unstable outside of [0.5 - 2]

Table 6.3: The sensitivity of the eigenfrequencies to doubling/halving one of the model parameters

Based on these results, the cumulative uncertainty of the found eigenfrequencies is in the range of 10%. Especially the amount of interference of the press fit and the friction coefficient increase the stiffness of the system, as expected.

6.4. Deflection caused by the forces

The mechanical response of the stator system is analyzed by applying the calculated forces to the numerical 3D model. The effect of the Power Electronic Converters has been neglected. In order to speed up the calculations, a frequency domain analysis is used. The complex force is transformed to the frequency domain by using a Fast-Fourier Transform in the time dimension, obtaining a magnitude and phase for each harmonic. By assuming the forces to be equal along the axial length of the stator core, and by fixing the radial position to the inner stator radius R_{si}, the force distribution can be described by the angular position along the stator and the frequency:

$$f(r,\theta,z,t) \rightarrow f(\theta,\omega) \tag{6.8}$$

6.4.1. Load application in COMSOL

The magnitude and phase for both the radial and tangential force are imported into COMSOL and interpolated [66]. These are then used to define a Boundary Load on the stator teeth, as shown in Figure 6.20 for the radial force [13]. It can be seen that the forces are the strongest at the edges of the teeth, as expected from the slot harmonics. Furthermore, the figure shows that the forces are approximately constant along the axial length; the deviations are caused by the discretization of the structure.

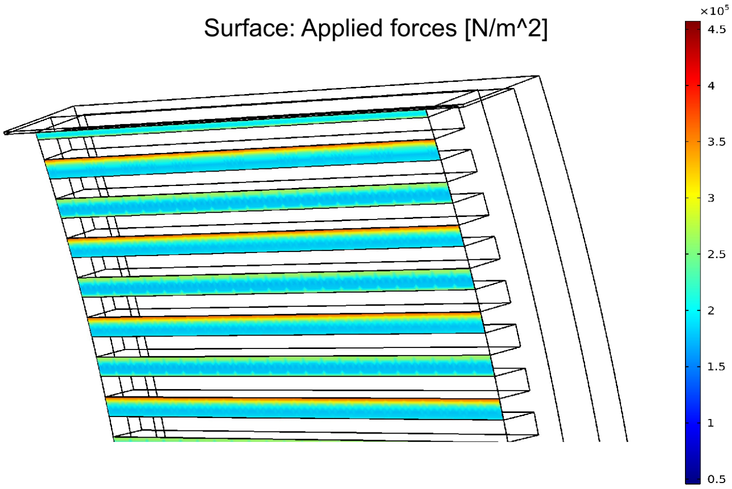

Figure 6.20: Application of a boundary load to the stator teeth in COMSOL

6.4.2. Modal analysis in the frequency domain

To study the resulting deflection, the 'Frequency Domain, Modal' study step is used in COMSOL. In this step, the previously calculated static deformation is used as linearization point, and the numerical eigenmodes are used to create a reduced-order system. The mechanical response can be calculated for a specified range of frequencies, which ideally includes the entire frequency spectrum of interest. In this case, it is known that the force harmonics primarily occur at multiples of $2\omega_e$, as was shown in Figure 4.10. In order to reduce the computation time, only these frequencies are included in the analysis. The modal solver also allows specifying modal damping factors, but these are neglected in this analysis.

After solving the deflection for different frequencies, the results are superimposed by summing the solutions. The results for the press fit design are shown in Figure 6.21. The total deflection includes all the static loads, including the strong constant radial pressure. This causes a large zeroth order deflection, shown in Figure 6.21a. Filtering out this mode results in Figure 6.21b, which consists primarily of the solutions for $2\omega_e$ and $4\omega_e$. In this solution, the 16th and 64th spatial order can be recognized, with a displacement in the same order of magnitude as predicted by the analytical method. It is also observed that the impact of the tangential force is negligible in this model.

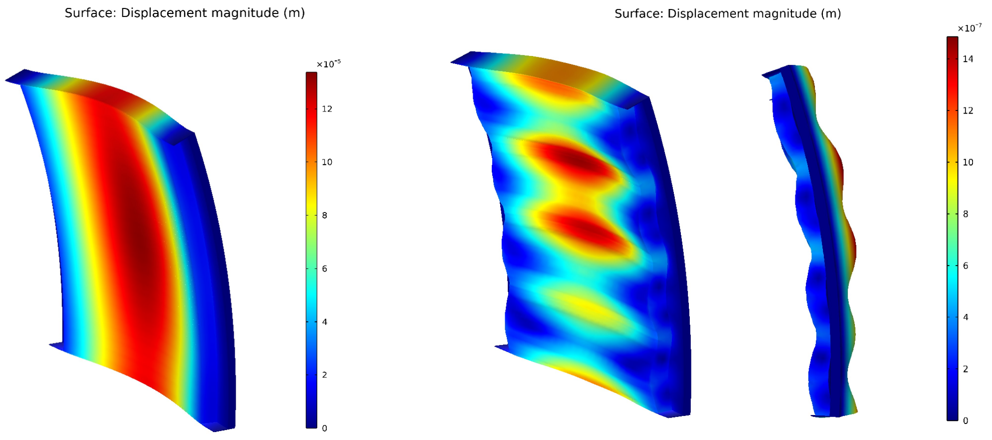

(a) Total deflection

(b) Filtering out the 0 Hz component

Figure 6.21: Deflection of the press fit model

The same forces have been applied to the design using support beams to constrain the segments, and the resulting deflection is shown in Figure 6.22. Again, the deflection is mainly caused by the constant pressure, which results in a displacement of 0.2 mm at the edges of the segment, shown in Figure 6.22a. In the other subfigures, the constant pressure is filtered out. The 16th and 64th mode can be recognized in Figure 6.22c, but it is clear that most of the deflection occurs at the unconstrained ends of the segment. This deflection is approximately an order of magnitude larger compared to the press fit model.

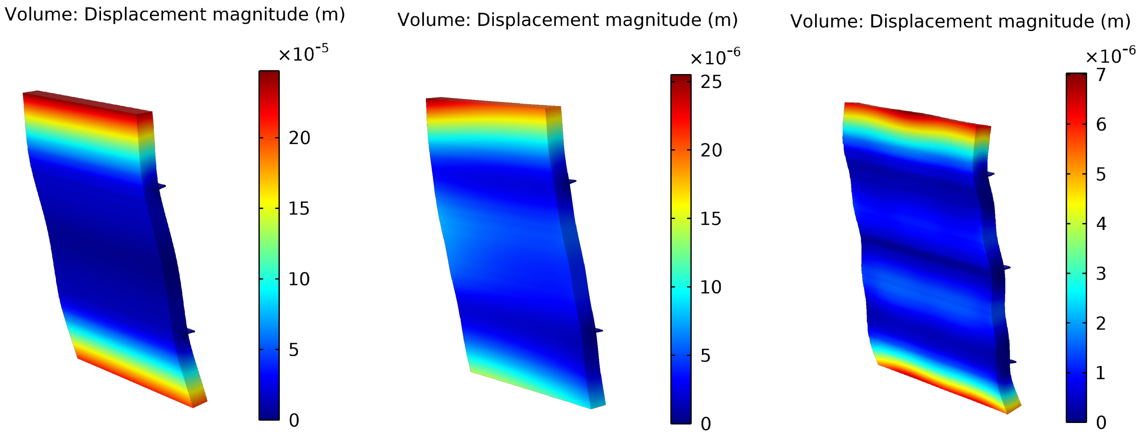

(a) Total deflection, 2 supports

(b) 2 supports, no 0 Hz component

(c) 3 supports, no 0 Hz component

Figure 6.22: Deflection of the supported segment designs

6.5. Summary

An electromagnetic and a mechanical analysis has been performed in COMSOL. The design from Chapter 3 has been verified, and most of the forces found agreed with the analytical model. Segmentation has been confirmed to mainly affect the cogging torque and the addition of forces with a low spatial order.

The mechanical analysis showed the importance of the breathing mode, the segment harmonic at $m = 16$ and the slot harmonic at $m = 64$. The tangential forces were found to have a negligible effect on the deflection of the structure.

7

Experimental approach

As discussed in the previous chapter, the mechanical model contains several uncertainties, which could lead to an inaccurate prediction of the mechanical response. This is the case for many vibration analyses, which is why numerical models are often combined with experimental models. The most common approach to combining numerical and experimental analyses is called ‘modal analysis’ [4, 24], which is based on the modal superposition method discussed in Section 5.1.

Several mechanical parameters can only be accurately determined by conducting vibration tests, such as the modal damping coefficients and the properties of the laminated core, as mentioned in the previous chapter. As the required parameters cannot be extracted directly from the experimental model, the observed vibrations are usually linked to a numerical model. By updating the parameters used in this model, the calculated eigenmodes and their corresponding frequencies can be fit to the observed vibrations. The goals of a modal analysis thus include conducting a representative vibration tests, obtain accurate data about the occurring vibrations, and linking this data to the existing numerical model.

7.1. Test setup

Figure 7.1 shows a schematic layout of a vibration test setup [2, 24, 29].

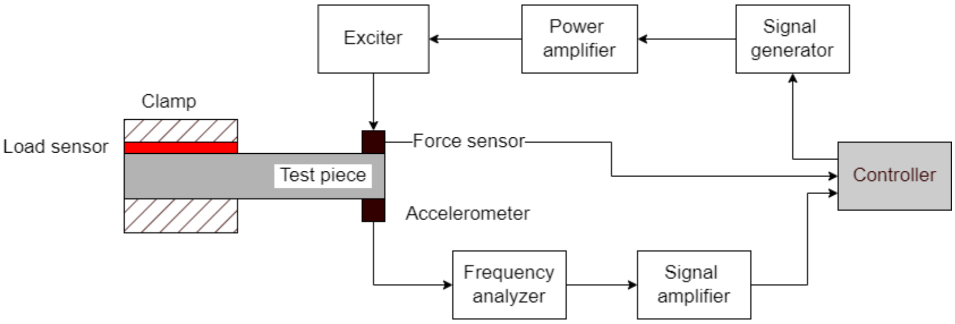

Figure 7.1: Example of a vibration test setup, based on [24, 29]

The test setup contains the following components:

- A test piece: ideally, the test piece is as close to the real generator as possible, and at least equal to the numerical model to which it will be compared. However, it is also possible to use a downscaled model while keeping material properties the same, as the forces per unit area will remain the same. Furthermore, it will also be useful to test simplified components to focus on one parameter at the time, as will be discussed in Section 7.2.
- A clamp: either a clamp to hold the test piece, or an object that represents the press fit. It is important to measure the clamping force, as this will influence the vibration response [24, 29].

- Response transducers: piezoelectric accelerometers are most commonly used to measure vibrations of the expected frequencies [28]. Multiple sensors will have to be placed on the test piece positioned such that different vibrations modes can be distinguished. Ideally, the accelerometers are placed at the peaks of the different eigenmodes predicted by the numerical model, as described in Chapter 5.
- A frequency analyzer: used to extract the vibration frequencies from the time-signal of the mechanical response.
- An exciter: the test piece can be moved by either a mechanical shaker, using an unbalanced rotating mass, or by (electro)magnets, which is similar to the operating conditions of the generator. Often, these approaches are combined to create an electrodynamic shaker, in which an alternating magnetic field is used to drive a magnet connected to the test piece [24]. Alternatively, an impact excitation could be used, such as a hammer with a force gauge. Depending on the location of impact, different modes can be excited.
- A controller: usually a computer or an embedded controller, which determines the excitation signal. Usually, a feedback loop from the vibration response is required, for example to limit the excitation amplitude when the excitation frequency is close to one of the resonance frequencies of the test piece.
- A power amplifier: the signal from the controller needs to be amplified to drive the exciter.

7.2. Test approach

Using this test setup, a modal analysis can be performed. By using a known excitation, the Frequency-Response Function of the test piece can be determined [24]. This represents the amplitude and vibration mode of the test piece depending on the frequency and location of the excitation. This vibration modes then needs to be linked to the predicted eigenmodes of the numerical model, which can be done either by hand or by using the Modal Assurance Criterion (MAC) [4]. This method calculates the correlation between eigenmodes found from different models, based on the deflection of multiple points on the test piece. For experimental results, these points refer to the locations of the response transducers.

In COMSOL, there is no built-in way to implement the MAC directly, so linking numerical and experimental eigenmodes will have to happen manually. However, COMSOL does enable parameter fitting to reference results, which can be used to find the best fit for several of the mechanical parameters [32]. As only one parameter can be varied at the time, the following order of experiments is proposed:

- As first test, use only a clamped laminated core segment to determine its orthotropic material parameters [29].
- If a press fit design is used, use a clamp that is representative of the way the core segments are clamped in the generator: pressing on the tangential ends, and constraining the outer radius. For a known clamping force, the numerical contact coefficients can be determined.
- By varying the clamping force, the impact of varying the interference δ and thus the normal force can be studied
- If the design using beams to support the core segments is used, the numerical model contains fewer uncertainties, and the numerical and experimental results can be compared more easily

Once the numerical model is updated, the Frequency-Response Function can be derived. Using this, in combination with the predicted operating forces, the expected vibrations can be calculated. As a final experiment, the in-operation vibrations of a full model can be measured, and compared to the vibrations predicted by the numerical model. This method has been used for full-scale wind turbines as well [41].

8

Discussion and conclusions

Based on the analytical and numerical models of the electromagnetic fields and the mechanical system, several conclusions can be drawn about the accuracy of the analytical models and the influence of segmentation on the vibrations occurring in a large direct-drive generator. Based on these conclusions, a few design rules can be derived.

8.1. Comparison of analytical and numerical results

An improved machine model for the ModHVDC generator has been designed, which takes into account current loading limits, saturation and the power factor of the machine. The new model has a diameter of 10 m, which is similar to other 10 MW Direct-Drive wind turbine generators. The numerical model in COMSOL verifies the analytical design of Chapter 3, as the machine shows the expected induced voltage and power level, without resulting in strong saturation in the stator teeth. This convergence in results gives confidence in the accuracy of the electromagnetic design of the generator.

Using this updated model, the electromagnetic flux density and the resulting forces were found to be accurately predicted by the analytical model for the unsegmented machine. Segmentation of the stator was found to have two important effects which were both only partially predicted by the analytical model: the addition of low-spatial order forces and an increase in the cogging torque. Both will be discussed in the next section.

In the mechanical analysis, the analytical ring models were found to provide a good first-order estimate of the eigenfrequencies for the stator core and frame. For the press fit design, the mechanical response was found to be close to that of the frame alone, and thus the analytical ring model could be used to analyze the press fit design as well. This cancels the need for complex contact analyses as performed in Chapter 6. For the design using beam-supported segments, no analytical model was found, and numerical analyses are always recommended due to the strong dependence on boundary conditions such as the location and size of the beams.

8.2. Conclusions

With the analytical and numerical analysis described in the previous chapters, the research questions posed in the introduction can be answered.

8.2.1. Resulting forces

A large part of the forces occurring in the ModHVDC generator are coming from sources that are not directly related to the segmentation of the stator. First of all, the fractional-slot concentrated windings that are required to disconnect the segments lead to large forces at a low spatial order both due to the subharmonics in the stator field and due to the slot harmonics. Both of these forces have a fundamental spatial order of $2F_1 = 2\,\mathrm{gcd}\,(N_s, p)$. Secondly, the open slots that are required for a high-voltage machine result in strong changes in the relative air gap permeance, increasing the slot harmonic amplitude. These two aspects of the design lead to a rich harmonic spectrum in both the radial and tangential forces.

8.2.2. Influence of segmentation on the forces

Segmentation of the stator was found to have two important effects: it causes a change in relative permeance in the same way slots do, and acts as flux barrier to the magnetic fields inside the stator. This leads to two main changes in the forces occurring in the machine:

- The gaps between the segment produce additional harmonics, with spatial orders at multiples of the number of segments. The numerical model shows a stronger effect than predicted by the analytical model. Upon inspection, it was found that these additional segment harmonics were partially caused by the armature reaction flux density harmonics, while the analytical model predicts they are primarily caused by the interaction of the permanent magnet field and the change in permeance at the segment gap. It is expected that this is caused by the change of the flux path in the back iron, which was not taken into account by the analytical method.
- Segmentation leads to an increase in cogging torque, and increases further with a larger gap between the segments. However, the cogging torque is increased even for an infinitesimally narrow gap, which cannot be predicted from the analytical model.

Increasing the width of the gap between the segments was found to primarily increase the cogging torque, but did not affect other aspects such as the output power.

The flux barrier between the segments was found to affect the mutual inductances between phases as well. While the mutual inductances between segments is reduced, the mutual inductance of some phases within one segment is increased. This means that for multi-phase segments, the fault tolerance to winding failures is not improved for each individual phase, as is the case for segments with only one coil [46]. Overall, the mutual inductance remains very low due to the use of non-overlapping windings.

8.2.3. Influence of power converters

An initial analysis showed the importance of taking into account the time harmonics in the current resulting from the use of Power Electronic converters. Even with a small amplitude, current harmonics lead to a significant increase in the breathing mode and torque ripple. The use of multiple smaller converters in the case of a modular machine helps to select a higher switching frequency and thus prevent resonance of the mechanical breathing mode.

8.2.4. Mechanical response

The mechanical analysis of the machine showed considerable uncertainty, due to unknown parameters and a strong dependency on the exact boundary conditions used. In general, it was found that segmentation reduces the stiffness of the stator system, as expected. This reduction is limited in the case of a press fit, as the frame and stator core still act as a single component and the segments are tightly held in position. For a design using beams to support the segments, the stiffness is reduced further, leading to lower eigenfrequencies and larger deflections.

The most important vibrations for this machine are the breathing mode, the 16th radial order, caused by segmentation, and the 64th radial order, caused by the slotting effect. The first two vibrations are important due to the risk of resonance, as the excitation frequency is close to the natural frequency of the system, while the latter is important due to the large amplitude of the slot harmonic for open-slot concentrated windings. Although the deflection caused by these modes is larger for the beam-supported segments than for the press fit, neither design has been found to be prohibitive. This will need validation from experimental analyses due to the uncertainty of the mechanical models. Finally, the tangential forces were found to have a minor influence on the vibration of the stator.

8.3. Design recommendations

Based on the analysis performed in this thesis, several design recommendations can be derived for further development of the ModHVDC generator:

- Both the press fit design as well as the beam-supported segments were found to be feasible designs. The choice of one over the other will depend on the required amount of cooling, the possibility of insulating the stator-frame interface, and the feasibility of building a press fit at the required scale.

- Although the cogging torque is increased by segmenting the stator, it remains below 1% of the nominal torque. No skewing is required to reduce the cogging torque.
- As the 16th radial force order is increased by segmentation and can lead to large deflections, it is recommended to choose a design that has a high stiffness in this mode. For the considered cases this rules out the 2-beam design, while the 3-beam design is preferred.
- The switching frequency of the PE converters should be selected while taking into account the natural frequency of the breathing mode and the spatial orders $2F_1$ and $2p$. The best strategy is to choose a switching frequency much larger than the natural frequency of the breathing mode, and far below the $2F_1$ and $2p$ modes.

8.4. Future work

First of all, the analytical model can be improved by computing the winding factors of the segmented stator core numerically, as has been done for other unconventional stators [34]. This can also include the change in flux pattern in the stator core, including the focusing or defocusing effects of the flux barriers between the segments [20, 46].

The analytical model can also be improved by linking a Power Electronic converter model to the magnetic field calculations, including a PWM current controller. This will give a more realistic analysis of the impact of the time harmonics in the current on the breathing mode and torque pulsation. A PE converter model has already been developed for the ModHVDC machine [25]. When such a PE converter model is implemented, it could also be interesting to research active noise control by injecting currents that cancel out dominant vibrations modes [28]. For the ModHVDC Generator in particular, this could be done by phase-shifting the carrier signals of the modules in order to reduce the ripple in the torque and thus DC output [23].

The mechanical models can be improved by updating the uncertain parameters as discussed in Chapter 7. This can validate the eigenfrequencies of especially the 0th, 16th and 64th radial modes, which are at risk of excitation. The experiments are also required to determine modal damping factors in the COMSOL models, as these are uncertain for the laminated cores and the interference fit.

Apart from improvements to the used models, there are also several aspects that are interesting to research, which fell outside of the scope of this thesis:

- Add a more detailed model of the beams. In the case of beams supporting the segments, a more elaborate model of these beams needs to be included in the vibration analysis. While the tangential forces have a limited influence on ring-shaped structures, they could result in tangential vibrations in the beams, moving the segments towards each other.
- Research the influence of unequal gaps between the segments. Even though manufacturing tolerances of laminations are below 0.1 mm [70], small asymmetries in w_{gap} for different segments can lead to an increased cogging torque at a lower frequency [87].
- Analyze non-nominal cases. If one module fails, and the ModHVDC generator continues to operate with one or two modules inoperative, strong $m = 1$ or $m = 2$ forces will be created in the machine.

References

[1] Alpogiannis, G. and Polinder, H. “Modeling and topology investigation of modular machines for wind generator systems”. Delft University of Technology, Oct. 2016. URL: `http://resolver.tudelft.nl/uuid:3d088772-b776-49b8-ac7e-fc196783180e`.

[2] Andersson, A. “Electric machine control for energy efficient electric drive systems”. Charlmers University of Technology, 2018. ISBN: 9789175977928.

[3] Arkkio, A. “Analysis of Induction Motors based on the Numerical Solution of the Magnetic Field and Circuit Equations”. Helsinki University of Technology, 1987. ISBN: 951-666-250-1.

[4] Avitabile, P. *Modal testing: a Practitioner’s Guide*. John Wiley & Sons, 2017. ISBN: 9781119222897.

[5] Bak, C. et al. *The DTU 10-MW Reference Wind Turbine. Sound/Visual production (digital)*. 2013.

[6] Bali, M. and Muetze, A. “The influence of cutting on the magnetic properties of electrical steel sheets and its modeling in electric machine design”. In: *Elektrotechnik und Informationstechnik* 134 (2 Apr. 2017), pp. 185–190. ISSN: 0932383X. DOI: `10.1007/s00502-017-0495-1`.

[7] Besnerais, J. L. et al. “Analysis of noise reduction in a low speed and high torque PMSM with tooth concentrated windings”. In: *2016 11th International Conference on Ecological Vehicles and Renewable Energies, EVER 2016* (May 2016). DOI: `10.1109/EVER.2016.7476351`.

[8] Besnerais, J. L. “Vibroacoustic analysis of radial and tangential air-gap magnetic forces in permanent magnet synchronous machines”. In: *IEEE Transactions on Magnetics* 51 (6 June 2015). ISSN: 00189464. DOI: `10.1109/TMAG.2015.2388613`.

[9] Besnerais, J. L. et al. “Acoustic noise of electromagnetic origin in a fractional-slot induction machine”. In: *COMPEL - The International Journal for Computation and Mathematics in Electrical and Electronic Engineering* 27 (5 2008), pp. 1033–1052. ISSN: 03321649. DOI: `10.1108/03321640810890753`.

[10] Besnerais, J. L. et al. “Characterization and reduction of audible magnetic noise due to PWM supply in induction machines”. In: *IEEE Transactions on Industrial Electronics* 57 (4 Apr. 2010), pp. 1288–1295. ISSN: 02780046. DOI: `10.1109/TIE.2009.2029529`.

[11] Bianchi, N. and Pré, M. D. “Use of the star of slots in designing fractional-slot single-layer synchronous motors”. In: *IEE Proceedings: Electric Power Applications* 153 (3 2006), pp. 459–466. ISSN: 13502352. DOI: `10.1049/ip-epa:20050284`.

[12] Bianchi, N. et al. “Design considerations for fractional-slot winding configurations of synchronous machines”. In: *IEEE Transactions on Industry Applications* 42 (4 July 2006), pp. 997–1006. ISSN: 00939994. DOI: `10.1109/TIA.2006.876070`.

[13] Bösing, M. “Acoustic Modeling of Electrical Drives”. RWTH Aachen, Sept. 2013. ISBN: 978-3-8440-2752-5.

[14] Cassoret, B., Lecointe, J.-P., and Brudny, J.-F. *Noise and Vibrations of Electrical Rotating Machines*. Ed. by B. M. Wilamowski and J. D. Irwin. 2011.

[15] Chen, Z and Spooner, E. “A modular, permanent-magnet generator for variable speed wind turbines”. In: *Seventh International Conference on Electrical Machines and Drives* (1995), pp. 453–457. ISSN: 0537-9989. DOI: `10.1049/cp:19950913`.

[16] COMSOL. *Structural Mechanics Module User’s Guide*. 2017. URL: `https://doc.comsol.com/`.

[17] Dajaku, G. and Gerling, D. “Analysis of different PM machines with concentrated windings and flux barriers in stator core”. In: *Proceedings - 2014 International Conference on Electrical Machines, ICEM 2014* (Nov. 2014), pp. 375–384. DOI: `10.1109/ICELMACH.2014.6960208`.

[18] Dajaku, G. and Gerling, D. “Low costs and high-efficiency electric machines”. In: *2012 2nd International Electric Drives Production Conference, EDPC 2012 - Proceedings* (2012). DOI: `10.1109/EDPC.2012.6425093`.

[19] Dajaku, G. and Gerling, D. “Magnetic radial force density of the PM machine with 12-teeth/10-poles winding topology”. In: *2009 IEEE International Electric Machines and Drives Conference, IEMDC ’09* (2009), pp. 1715–1720. DOI: `10.1109/IEMDC.2009.5075434`.

[20] Dajaku, G., Xie, W., and Gerling, D. “Reduction of low space harmonics for the fractional slot concentrated windings using a novel stator design”. In: *IEEE Transactions on Magnetics* 50 (5 2014). ISSN: 00189464. DOI: `10.1109/TMAG.2013.2294754`.

[21] EL-Refaie, A. M. “Fractional-slot concentrated-windings synchronous permanent magnet machines: Opportunities and challenges”. In: *IEEE Transactions on Industrial Electronics* 57 (1 Jan. 2010), pp. 107–121. ISSN: 02780046. DOI: `10.1109/TIE.2009.2030211`.

[22] El-Refaie, A. M., Jahns, T. M., and Novotny, D. W. “Analysis of surface permanent magnet machines with fractional-slot concentrated windings”. In: *IEEE Transactions on Energy Conversion* 21 (1 Mar. 2006), pp. 34–43. ISSN: 08858969. DOI: `10.1109/TEC.2005.858094`.

[23] ElShawarby, K. et al. “DC Voltage and Torque Ripple Mitigation in Modular PMSG Drives for Off-Shore Multi-MW WECSs with Linear SPWM modulation”. In: *21st European Conference on Power Electronics and Applications* (2019).

[24] Ewins, D. J. *Modal Testing: Theory, Practice and Application*. John Wiley & Sons, 2009. ISBN: 9780863802188.

[25] Faraasen, H. A. *Power Electronic Converters for Efficient Operation of the Modular HVDC Generator for Offshore Wind Power Comparison of DC-bus voltage balancing, IGBT module losses and performance gains with the 3L-NPC converter*. 2020.

[26] Fiedler, J. O., Kasper, K. A., and Doncker, R. W. D. “Calculation of the acoustic noise spectrum of SRM using modal superposition”. In: *IEEE Transactions on Industrial Electronics* 57 (9 Sept. 2010), pp. 2939–2945. ISSN: 02780046. DOI: `10.1109/TIE.2010.2046573`.

[27] Geng, G and Spooner, E. “Cancellation of Noise and Vibration in Modular Permanent-Magnet Wind Turbine Generators”. In: *1995 Seventh International Conference on Electrical Machines and Drives* (412 1995), pp. 467–471. ISSN: 0537-9989. DOI: `10.1049/cp:19950916`.

[28] Gieras, J. F., Wang, C., and Lai, J. C. *Noise of Polyphase Electric Motors*. CRC Press, Oct. 2018. ISBN: 9781420027730. DOI: `10.1201/9781420027730`.

[29] Giet, M. et al. “Material parameters for the structural dynamic simulation of electrical machines”. In: *20th International Conference on Electrical Machines, ICEM 2012* (2012), pp. 2994–3000. DOI: `10.1109/ICElMach.2012.6350314`.

[30] Gjerde, S. S., Olsen, P. K., and Undeland, T. M. “A Transformerless Generator-Converter Concept making feasible a 100 kV Low Weight Offshore Wind Turbine Part II - The Converter”. In: *2012 IEEE Energy Conversion Congress and Exposition, ECCE 2012* (2012), pp. 253–260. DOI: `10.1109/ECCE.2012.6342815`.

[31] Gjerde, S. S. et al. “Control and fault handling in a modular series-connected converter for a transformerless 100 kv low-weight offshore wind turbine”. In: *IEEE Transactions on Industry Applications* 50 (2 2014), pp. 1094–1105. ISSN: 00939994. DOI: `10.1109/TIA.2013.2272032`.

[32] Halliday, A. *How to Use the Parameter Estimation Study Step for Inverse Modeling*. 2018. URL: `https://www.comsol.com/blogs/how-to-use-the-parameter-estimation-study-step-for-inverse-modeling/` (visited on 06/23/2022).

[33] Hanselman, D. C. *Brushless Permanent Magnet Motor Design*. McGraw-Hill Inc., 2006.

[34] Heins, G., Ionel, D. M., and Thiele, M. “Winding Factors and Magnetic Fields in Permanent-Magnet Brushless Machines With Concentrated Windings and Modular Stator Cores”. In: *IEEE Transactions on Industry Applications* 51 (4 July 2015), pp. 2924–2932. ISSN: 00939994. DOI: `10.1109/TIA.2015.2394444`.

[35] Hoeijmakers, M. J. *Modelling of AC machines*. TU Delft, 2004.

[36] Hwang, S. M. et al. “Cogging torque and acoustic noise reduction in permanent magnet motors by teeth pairing”. In: *IEEE Transactions on Magnetics* 36 (5 I Sept. 2000), pp. 3144–3146. ISSN: 00189464. DOI: `10.1109/20.908714`.

[37] Hwang, S. M. et al. “Various design techniques to reduce cogging torque by controlling energy variation in permanent magnet motors”. In: *IEEE Transactions on Magnetics* 37 (4 I July 2001), pp. 2806–2809. ISSN: 00189464. DOI: `10.1109/20.951313`.

[38] IEA. *Offshore Wind Outlook 2019: World Energy Outlook Special Report*. International Energy Agency, 2019.

[39] IPCC. *Sixth Assessment Report - Working Group III: Mitigation of Climate Change*. 2022.

[40] Jackson, J. D. *Classical Electrodynamics*. 1st ed. John Wiley & Sons, 1962. ISBN: 0-471-43131-1.

[41] Kirschneck, M. “Mastering Electro-Mechanical Dynamics of Large Off-Shore Direct-Drive Wind Turbine Generators”. Delft University of Technology, Mar. 2016. ISBN: 9789462993235. DOI: `https://doi.org/10.4233/uuid:e8e70eac-b6b1-4561-8eee-5b03013c4680`.

[42] Klop, C. *Initial Design and Sizing of a 10 MW PMSM Wind Turbine Generator*. 2021.

[43] Kooloos, W. *Limiting mechanisms for the torque density of wind turbine drivetrains*. Delft University of Technology, July 2019. URL: `http://resolver.tudelft.nl/uuid:0c3ba0e4-0bf8-4fdb-b55f-afbba70f8e68`.

[44] Korzunin, G. S. et al. “Developing Techniques for Testing Magnetic Properties of Electric Steels. III. Apparatus for Sheet Steel (Review Article)”. In: *Russian Journal of Nondestructive Testing* 37 (6 2001), pp. 397–421.

[45] Krøvel, O. *Design of Large Permanent Magnetized Synchronous Electric Machines*. 2011. URL: `http://hdl.handle.net/11250/256994`.

[46] Li, G. J. et al. “Influence of flux gaps on electromagnetic performance of novel modular pm machines”. In: *IEEE Transactions on Energy Conversion* 29 (3 2014), pp. 716–726. ISSN: 08858969. DOI: `10.1109/TEC.2014.2312429`.

[47] Lyngved, K. H. and Olsen, P. K. *Investigating Thermal Management Solutions in a Modular High Voltage Machine for Offshore Wind Application*. NTNU, 2021. URL: `https://hdl.handle.net/11250/2824803`.

[48] Magnussen, F. and Lendenmann, H. “Parasitic effects in PM machines with concentrated windings”. In: *IEEE Transactions on Industry Applications* 43 (5 Sept. 2007), pp. 1223–1232. ISSN: 00939994. DOI: `10.1109/TIA.2007.904400`.

[49] Mecrow, B. C. et al. “Design and testing of a four-phase fault-tolerant permanent-magnet machine for an engine fuel pump”. In: *IEEE Transactions on Energy Conversion* 19 (4 Dec. 2004), pp. 671–678. ISSN: 08858969. DOI: `10.1109/TEC.2004.832074`.

[50] Mellerud, R. “Analysis of Losses and Radial Vibration in a PM Synchronous Machine with Physical Modularity”. NTNU, 2021.

[51] Mohan, N., Undeland, T. M., and Robbins, W. *Power Electronics*. 2nd. John Wiley & Sons, Inc, 1995. ISBN: 0471584088.

[52] Olsen, P. K. et al. “A Transformerless Generator-Converter Concept making feasible a 100 kV Low Weight Offshore Wind Turbine Part I - The Generator”. In: *IEEE Energy Conversion Congress and Exposition* (2012), pp. 247–252. DOI: `10.1109/ECCE.2012.6342816`.

[53] Olsen, P. K. “Energy Conversion System”. Pat. 2012.

[54] Paudel, N. *How to Analyze an Induction Motor: A TEAM Benchmark Model*. 2016. URL: `https://www.comsol.com/blogs/how-to-analyze-an-induction-motor-a-team-benchmark-model/` (visited on 10/21/2021).

[55] Pedersen, E. and Waye, K. P. “Perception and annoyance due to wind turbine noise—a dose–response relationship”. In: *The Journal of the Acoustical Society of America* 116 (6 Dec. 2004), pp. 3460–3470. ISSN: 0001-4966. DOI: `10.1121/1.1815091`.

[56] Pfingsten, G. V., Hameyer, K., and Paul, D. “Influence of axial mechanical stress on the magnetic properties of non-oriented electrical steel”. In: *2016 6th International Electric Drives Production Conference, EDPC 2016 - Proceedings* (2016), pp. 193–200. DOI: `10.1109/EDPC.2016.7851333`.

[57] Polinder, H. et al. “10 MW wind turbine direct-drive generator design with pitch or active speed stall control”. In: *Proceedings of IEEE International Electric Machines and Drives Conference, IEMDC 2007* 2 (2007), pp. 1390–1395. DOI: `10.1109/IEMDC.2007.383632`.

[58] Polinder, H. et al. “Fault tolerant generator systems for wind turbines”. In: *IEEE International Electric Machines and Drives Conference* (2009), pp. 675–681. DOI: `10.1109/IEMDC.2009.5075278`.

[59] Polinder, H. *Principles of electrical design of permanent magnet generators for direct drive renewable energy systems*. 2013. DOI: `10.1533/9780857097491.1.30`.

[60] Saito, A. et al. “Equivalent orthotropic elastic moduli identification method for laminated electrical steel sheets”. In: *Mechanical Systems and Signal Processing* 72-73 (May 2016), pp. 607–628. ISSN: 10961216. DOI: `10.1016/j.ymssp.2015.10.027`.

[61] Sethuraman, L., Maness, M., and Dykes, K. *Optimized Generator Designs for the DTU 10-MW Offshore Wind Turbine using GeneratorSE*. NREL, 2017.

[62] Shen, J. et al. “Analysis and optimization of a modular stator core with segmental teeth and solid back iron for pm electric machines”. In: *IEEE International Electric Machines and Drives Conference, IEMDC 2011* (2011), pp. 1270–1275. DOI: `10.1109/IEMDC.2011.5994787`.

[63] Shipurkar, U., Polinder, H., and Ferreira, J. A. *Modularity in Wind Turbine Generator Systems-Opportunities and Challenges*. 2016.

[64] Shipurkar, U. et al. “Comparison of Modular Wind Turbine Generators Considering Structural Aspects”. In: *IECON 2017 - 43rd Annual Conference of the IEEE Industrial Electronics Society* (2017), pp. 3707–3712. DOI: `10.1109/IECON.2017.8216630`.

[65] Skaar, S., Krøvel, O, and Nilssen, R. “Distribution, coil-span and winding factors for PM machines with concentrated windings”. In: *ICEM 2006* (2006).

[66] Son, C. *Noise Modelling and Reduction of Permanet Magnet Motor in EV*. Delft University of Technology, Aug. 2018. URL: `http://resolver.tudelft.nl/uuid:67325401-d045-4d2c-85e2-dd01a9f8642e`.

[67] Spooner, E. and Williamson, A. “Modular, permanent-magnet wind-turbine generators”. In: *Conference Record - IAS Annual Meeting (IEEE Industry Applications Society)* 1 (1996), pp. 497–502. ISSN: 01972618. DOI: `10.1109/ias.1996.557073`.

[68] Strand, S. S. *Electromagnetic Design of Modular Generators for Offshore Wind Power Applications*. 2020.

[69] Timár, P. L. *Noise and vibration of electrical machines*. Elsevier, 1989. ISBN: 9780444417138.

[70] Tong, W. *Mechanical Design of Electric Motors*. CRC press, 2014. ISBN: 978-1-4200-9144-1.

[71] Valavi, M. “Magnetic Forces and Vibration in Wind Power Generators”. NTNU, 2015. ISBN: 9788232610648.

[72] Valavi, M., Besnerais, J. L., and Nysveen, A. “An Investigation of Zeroth-Order Radial Magnetic Forces in Low-Speed Surface-Mounted Permanent Magnet Machines”. In: *IEEE Transactions on Magnetics* 52 (8 Aug. 2016). ISSN: 00189464. DOI: `10.1109/TMAG.2016.2553642`.

[73] Valavi, M., Nysveen, A., and Nilssen, R. “Effects of Loading and Slot Harmonic on Radial Magnetic Forces in Low-Speed Permanent Magnet Machine with Concentrated Windings”. In: *IEEE Transactions on Magnetics* 51 (6 June 2015). ISSN: 00189464. DOI: `10.1109/TMAG.2014.2377014`.

[74] Valavi, M., Nysveen, A., and Nilssen, R. “Magnetic forces and vibration in permanent magnet machines with non-overlapping concentrated windings: A review”. In: *2012 IEEE International Conference on Industrial Technology* (2012). DOI: `10.1109/ICIT.2012.6210066`.

[75] Valavi, M. et al. “Influence of Converter Topology and Carrier Frequency on Airgap Field Harmonics, Magnetic Forces, and Vibrations in Converter-Fed Hydropower Generator”. In: *IEEE Transactions on Industry Applications* 54 (3 May 2018), pp. 2202–2214. ISSN: 00939994. DOI: `10.1109/TIA.2018.2801859`.

[76] Valavi, M. et al. “Influence of pole and slot combinations on magnetic forces and vibration in low-speed PM wind generators”. In: *IEEE Transactions on Magnetics* 50 (5 2014). ISSN: 00189464. DOI: `10.1109/TMAG.2013.2293124`.

[77] Valavi, M. et al. “Slot harmonic effect on magnetic forces and vibration in low-speed permanent-magnet machine with concentrated windings”. In: *IEEE Transactions on Industry Applications* 50 (5 Sept. 2014), pp. 3304–3313. ISSN: 00939994. DOI: `10.1109/TIA.2014.2309717`.

[78] Vaschetto, S., Tenconi, A., and Bramerdorfer, G. “Sizing Procedure of Surface Mounted PM Machines for Fast Analytical Evaluations”. In: *IEEE International Electric Machines and Drives Conference (IEMDC)* (2017), pp. 1–8.

[79] Wang, J. et al. “Vibration characteristics of modular permanent magnet brushless AC machines”. In: *Conference Record - IAS Annual Meeting (IEEE Industry Applications Society)* 3 (2006), pp. 1501–1506. ISSN: 01972618. DOI: `10.1109/IAS.2006.256728`.

[80] Weiss, H. A. et al. “Impact of Punching Parameter Variations on Magnetic Properties of Nongrain-Oriented Electrical Steel”. In: *IEEE Transactions on Industry Applications* 54 (6 Nov. 2018), pp. 5869–5878. ISSN: 00939994. DOI: `10.1109/TIA.2018.2853133`.

[81] WindEurope. *North Sea offshore wind to help repower the EU*. May 2022. URL: `https://windeurope.org/newsroom/press-releases/north-sea-offshore-wind-to-help-repower-the-eu/`.

[82] Wolmarans, J. et al. “A 50kW Integrated Fault Tolerant Permanent Magnet Machine and Motor Drive”. In: *2008 IEEE Power Electronics Specialists Conference* (2008), pp. 345–351. DOI: `10.1109/PESC.2008.4591953`.

[83] Xia, C. et al. “Joining of the laminated electrical steels in motor manufacturing: A review”. In: *Materials* 13 (20 Oct. 2020), pp. 1–21. ISSN: 19961944. DOI: `10.3390/ma13204583`.

[84] Yang, S. *Low-Noise Electrical Motors*. Clarendon Press, 1981. ISBN: 9780198593324.

[85] Yokoi, Y., Higuchi, T., and Miyamoto, Y. “General Formulation of Winding Factor for Fractional-Slot Concentrated Winding Design”. In: *IET Electric Power Applications* 10 (4 2016), pp. 231–239.

[86] Yuan, J., Shi, C. W., and Shen, J. X. “Analysis of cogging torque in surface-mounted permanent magnet machines with segmented stators”. In: *2014 17th International Conference on Electrical Machines and Systems, ICEMS 2014* (2014), pp. 2513–2516. DOI: `10.1109/ICEMS.2014.7013924`.

[87] Zhu, Z. Q., Azar, Z., and Ombach, G. “Influence of additional air gaps between stator segments on cogging torque of permanent-magnet machines having modular stators”. In: *IEEE Transactions on Magnetics* 48 (6 2012), pp. 2049–2055. ISSN: 00189464. DOI: `10.1109/TMAG.2011.2179667`.

[88] Zhu, Z. Q. and Howe, D. “Analytical Prediction of the Cogging Torque in Radial-field Permanent Magnet Brushless Motors”. In: *IEEE Transactions on Magnetics* 28 (2 1992), pp. 1371–1374. ISSN: 19410069. DOI: `10.1109/20.123947`.

[89] Zhu, Z. Q. and Howe, D. “Influence of design parameters on cogging torque in permanent magnet machines”. In: *IEEE Transactions on Energy Conversion* 15 (4 Dec. 2000), pp. 407–412. ISSN: 08858969. DOI: `10.1109/60.900501`.

[90] Zhu, Z. Q. and Howe, D. “Instantaneous Magnetic Field Distribution in Brushless Permanent Magnet DC Motors, Part II: Armature-Reaction Field”. In: *IEEE Transactions on Magnetics* 29 (1 1993), pp. 136–142. ISSN: 19410069. DOI: `10.1109/20.195558`.

[91] Zhu, Z. Q. and Howe, D. “Instantaneous Magnetic Field Distribution in Brushless Permanent Magnet DC Motors, Part III: Effect of stator slotting”. In: *IEEE Transactions on Magnetics* 29 (1 1993), pp. 143–151. ISSN: 19410069. DOI: `10.1109/20.195559`.

[92] Zhu, Z. Q., Howe, D., and Chan, C. C. “Improved analytical model for predicting the magnetic field distribution in brushless permanent-magnet machines”. In: *IEEE Transactions on Magnetics* 38 (1 II Jan. 2002), pp. 229–238. ISSN: 00189464. DOI: `10.1109/20.990112`.

[93] Zhu, Z. Q. et al. “Analytical modeling and finite-element computation of radial vibration force in fractional-slot permanent-magnet brushless machines”. In: *IEEE Transactions on Industry Applications* 46 (5 Sept. 2010), pp. 1908–1918. ISSN: 00939994. DOI: `10.1109/TIA.2010.2058078`.

[94] Zhu, Z. Q. et al. "Instantaneous Magnetic Field Distribution in Brushless Permanent Magnet DC Motors, Part I: Open-Circuit Field". In: *IEEE Transactions on Magnetics* 29 (1 1993), pp. 124–135. ISSN: 19410069. DOI: `10.1109/20.195557`.

[95] Zhu, Z. Q. et al. "Instantaneous Magnetic Field Distribution in Permanent Magnet Brushless DC Motors, Part IV: Magnetic field on load". In: *IEEE Transactions on Magnetics* 29 (1 1993), pp. 152–158. ISSN: 19410069. DOI: `10.1109/20.195560`.

[96] Žarko, D., Ban, D., and Lipo, T. A. "Analytical calculation of magnetic field distribution in the slotted air gap of a surface permanent-magnet motor using complex relative air-gap permeance". In: *IEEE Transactions on Magnetics* 42 (7 July 2006), pp. 1828–1837. ISSN: 00189464. DOI: `10.1109/TMAG.2006.874594`.

A

Explanation of Maxwell’s stress tensor

The Maxwell stress tensor is a key aspect of the research conducted in this thesis. Its derivation is shown here, including a brief explanation of tensor notation.[1]

A.1. Motivation

As is well known, electromagnetic fields can be described by 4 laws: Maxwell’s equations, shown in Table A.1.

Table A.1: Maxwell’s equations in differential form

Gauss’s law	$\nabla \cdot \mathbf{E} = \frac{\rho}{\epsilon_0}$	Relates the electric field to the electric charge distribution
Gauss’s law for magnetism	$\nabla \cdot \mathbf{B} = 0$	States that magnetic monopoles do not exist
Faraday’s law of induction	$\nabla \times \mathbf{E} = -\frac{\partial \mathbf{B}}{\partial t}$	Relates the induced electrical field to the time derivative of the magnetic field
Ampère circuit law	$\nabla \times \mathbf{B} = \mu_0 \mathbf{J} + \mu_0 \epsilon_0 \frac{\partial \mathbf{E}}{\partial t}$	Relates the magnetic field to the electric current

Maxwell’s stress tensor combines these equations into one tensor equation, which can be used to calculate the normal and shear stresses in a field. Tensor notation is well suited to include many different quantities in a field in a very concise manner.

A.2. Introduction to tensor notation

Tensors can be considered as indexed objects, mapping scalars and vectors. In fact, scalars and vectors are the simplest examples of a tensor. Many well-known concepts from calculus and linear algebra are included in tensor algebra, but are written in a different way, the index notation, by the conventions of *Ricci calculus*. In the field of engineering, the main focus is on *tensor fields*, which are often simply referred to as tensors. In a tensor field, a tensor is assigned to each point in space.

The number of indices indicates the *order* of the tensor; a vector **a** has order 1, as it can be represented as a 1-dimensional array, while a matrix B has order 2. In tensor notation, this becomes

$$a_i \qquad \wedge \qquad A_{ij}$$

The power of the tensor notation is that each entry of a tensor in an equation is considered simultaneously, in order to represent systems of equations with a single tensor equation. Furthermore, several shorthand notations exist for complex operations. For example, by the Einstein summation convention, each repeated index is implicitly summed over:

---

[1] Relevant sections from `https://www.continuummechanics.org/tensornotationbasic.html` are used to explain tensor notation. The reader is referred to this page for more information.

$$a_i b_i = a_1 b_1 + a_2 b_2 + a_3 b_3 \tag{A.1}$$

Which represents the inner product of a and b.

The *Kronecker Delta* δ_{ij} serves a similar purpose as the identity matrix **I**, because it equals 1 when $i = j$ and is 0 otherwise. It can be thought of as a single entry of the identity matrix, as it takes a scalar value depending on its indices.

The *alternating tensor* ϵ_{ijk} is used to represent cross products. Its components are

$$\epsilon_{123} = \epsilon_{231} = \epsilon_{312} = 1 \qquad \wedge \qquad \epsilon_{321} = \epsilon_{213} = \epsilon_{132} = -1$$

With all other components zero. The cross product $\mathbf{c} = \mathbf{a} \times \mathbf{b}$ corresponds to $c_i = \epsilon_{ijk} a_j b_k$, which is expanded below to give an example of a tensor equation and its power. Because j and k are repeated, they are summed over. This leads to

$$\begin{aligned} c_i = \epsilon_{ijk} a_j b_k = {} & \epsilon_{i11} a_1 b_1 + \epsilon_{i12} a_1 b_2 + \epsilon_{i13} a_1 b_3 + \\ & \epsilon_{i21} a_2 b_1 + \epsilon_{i22} a_2 b_2 + \epsilon_{i23} a_2 b_3 + \\ & \epsilon_{i31} a_3 b_1 + \epsilon_{i32} a_3 b_2 + \epsilon_{i33} a_3 b_3 \end{aligned} \tag{A.2}$$

This still holds true for all i. Setting $i = 2$ as example, many terms equal zero and the equation yields

$$c_2 = \epsilon_{2jk} a_j b_k = a_3 b_1 - a_1 b_3 \tag{A.3}$$

which is the expected value of the second term of the cross product (and similar for the other values of i). This shows how a single tensor equation can contain a significant amount of information.

Second-order tensors are common in physics and engineering, and can be represented in the more recognizable form of matrices. This is called a *dyadic*, and can be considered as the expanded form of a tensor. It is represented by a double arrow accent, such as the *unit dyadic* below:

$$\overleftrightarrow{\boldsymbol{I}} = \begin{pmatrix} 1 & 0 & 0 \\ 0 & 1 & 0 \\ 0 & 0 & 1 \end{pmatrix} \tag{A.4}$$

The *dyadic product* (or outer/tensor product) of two vectors is defined as

$$\overleftrightarrow{\mathbf{c}} = \mathbf{a} \otimes \mathbf{b} \equiv \mathbf{a}\mathbf{b}^{\mathsf{T}} = \begin{pmatrix} a_1 \\ a_2 \\ a_3 \end{pmatrix} \begin{pmatrix} b_1 & b_2 & b_3 \end{pmatrix} = \begin{pmatrix} a_1 b_1 & a_1 b_2 & a_1 b_3 \\ a_2 b_1 & a_2 b_2 & a_2 b_3 \\ a_3 b_1 & a_3 b_2 & a_3 b_3 \end{pmatrix} \tag{A.5}$$

In tensor notation, the dyadic product is written as

$$c_{ij} = a_i b_j \tag{A.6}$$

As a last part of the introduction to tensor notation, partial derivatives of a tensor are often represented by *comma notation*. The vector derivative $\frac{\partial \mathbf{v}}{\partial x_j}$ is represented by $v_{i,j}$, and the tensor derivative $\frac{\partial \sigma}{\partial x_k}$ by $\sigma_{ij,k}$. The divergence of a vector is a scalar, and is written as

$$v_{i,i} = \frac{\partial v_1}{\partial x_1} + \frac{\partial v_2}{\partial x_2} + \frac{\partial v_3}{\partial x_3} \tag{A.7}$$

The sum over the derived components is implicit in the above notation, as i was repeated as subscript. Finally, the *divergence of a tensor field* is used in the force equation that will be derived later. For a symmetric second-order tensor **A** (such as Maxwell's stress tensor), the divergence is defined as

$$\operatorname{div} \mathbf{A} = \nabla \cdot \mathbf{A} = A_{ik,k} \mathbf{e}_i = \begin{pmatrix} \frac{\partial A_{11}}{\partial x_1} + \frac{\partial A_{12}}{\partial x_2} + \frac{\partial A_{13}}{\partial x_3} \\ \frac{\partial A_{21}}{\partial x_1} + \frac{\partial A_{22}}{\partial x_2} + \frac{\partial A_{23}}{\partial x_3} \\ \frac{\partial A_{31}}{\partial x_1} + \frac{\partial A_{32}}{\partial x_2} + \frac{\partial A_{33}}{\partial x_3} \end{pmatrix} \tag{A.8}$$

Which thus results in a vector with three components. This concludes the discussion on the required concepts of tensors and their notation, which can now be applied to Maxwell's equations.

A.3. Derivation of the conservation laws

This derivation is based on the one found in Classical Electrodynamics by J. Jackson [40].

Starting from the Lorentz force law

$$\mathbf{F} = q\left(\mathbf{E} + \mathbf{v} \times \mathbf{B}\right) \tag{A.9}$$

The force per unit volume equals

$$\mathbf{f} = \rho\mathbf{E} + \mathbf{J} \times \mathbf{B} \tag{A.10}$$

Using Gauss's law and Ampère's law to write the force entirely in terms of fields:

$$\mathbf{f} = \epsilon_0(\nabla \cdot \mathbf{E})\mathbf{E} + \frac{1}{\mu_0}(\nabla \times \mathbf{B}) \times \mathbf{B} - \epsilon_0\frac{\partial \mathbf{E}}{\partial t} \times \mathbf{B} \tag{A.11}$$

The time derivative of the electric field is than rewritten in terms of the Poynting vector, $\mathbf{S} = \frac{1}{\mu_0}\mathbf{E} \times \mathbf{B}$. The Poynting vector represents the energy flux (energy transfer per unit area per unit time) of the electromagnetic field. It is found in Poynting's theorem, an energy-conservation law, which states that within a volume the negative time rate of change of electromagnetic energy density equals the energy flowing out its surface plus the work done by the electric field [40]:

$$\boxed{-\frac{\partial u}{\partial t} = \nabla \cdot \mathbf{S} + \mathbf{J} \cdot \mathbf{E}} \tag{A.12}$$

This equation does not take into account non-linear effects such as hysteresis.

Returning to Poynting's vector, its time derivative can be written out and combined with Faraday's law of induction as

$$\frac{\partial}{\partial t}(\mathbf{E} \times \mathbf{B}) = \frac{\partial \mathbf{E}}{\partial t} \times \mathbf{B} + \mathbf{E} \times \frac{\partial \mathbf{B}}{\partial t} = \frac{\partial \mathbf{E}}{\partial t} \times \mathbf{B} - \mathbf{E} \times (\nabla \times \mathbf{E}) \tag{A.13}$$

which can be substituted into the equation for the force

$$\mathbf{f} = \epsilon_0(\nabla \cdot \mathbf{E})\mathbf{E} + \frac{1}{\mu_0}(\nabla \times \mathbf{B}) \times \mathbf{B} - \epsilon_0\frac{\partial}{\partial t}(\mathbf{E} \times \mathbf{B}) - \epsilon_0\mathbf{E} \times (\nabla \times \mathbf{E}) \tag{A.14}$$

Gathering terms with **E** and **B** shows that the equation is not entirely symmetric, as is desired when writing the equations in tensor notation. As Gauss's law for magnetism states $\nabla \cdot \mathbf{B} = 0$, the term making the equation symmetric can be inserted

$$\mathbf{f} = \epsilon_0\left[(\nabla \cdot \mathbf{E})\mathbf{E} - \mathbf{E} \times (\nabla \times \mathbf{E})\right] + \frac{1}{\mu_0}\left[-\mathbf{B} \times (\nabla \times \mathbf{B})\right] - \epsilon_0\frac{\partial}{\partial t}(\mathbf{E} \times \mathbf{B}) \tag{A.15}$$

$$\mathbf{f} = \epsilon_0\left[(\nabla \cdot \mathbf{E})\mathbf{E} - \mathbf{E} \times (\nabla \times \mathbf{E})\right] + \frac{1}{\mu_0}\left[(\nabla \cdot \mathbf{B})\mathbf{B} - \mathbf{B} \times (\nabla \times \mathbf{B})\right] - \epsilon_0\frac{\partial}{\partial t}(\mathbf{E} \times \mathbf{B}) \tag{A.16}$$

Using the vector calculus identity $\frac{1}{2}\nabla(\mathbf{A} \cdot \mathbf{A}) = \mathbf{A} \times (\nabla \times \mathbf{A}) + (\mathbf{A} \cdot \nabla)\mathbf{A}$ to remove the curls gives

$$\mathbf{f} = \epsilon_0\left[(\nabla \cdot \mathbf{E})\mathbf{E} + (\mathbf{E} \cdot \nabla)\mathbf{E}\right] + \frac{1}{\mu_0}\left[(\nabla \cdot \mathbf{B})\mathbf{B} + (\mathbf{B} \cdot \nabla)\mathbf{B}\right] - \frac{1}{2}\nabla\left(\epsilon_0 E^2 + \frac{1}{\mu_0}B^2\right) - \epsilon_0\frac{\partial}{\partial t}(\mathbf{E} \times \mathbf{B}) \tag{A.17}$$

This now contains all information to calculate the force at any location, but the equation is lengthy. The Maxwell stress tensor is introduced here as

$$\sigma_{ij} \equiv \epsilon_0\left(E_iE_j - \frac{1}{2}\delta_{ij}E^2\right) + \frac{1}{\mu_0}\left(B_iB_j - \frac{1}{2}\delta_{ij}B^2\right) \tag{A.18}$$

With its dyadic

$$\overleftrightarrow{\boldsymbol{\sigma}} = \epsilon_0\mathbf{E} \otimes \mathbf{E} + \frac{1}{\mu_0}\mathbf{B} \otimes \mathbf{B} - \frac{\epsilon_0 E^2 + \frac{1}{\mu_0}B^2}{2}\overleftrightarrow{\boldsymbol{I}} \tag{A.19}$$

Using the Maxwell stress tensor and the definition of the Poynting vector then makes it possible to write Eq. A.17 in a very concise way:

$$\boxed{\nabla \cdot \overleftrightarrow{\boldsymbol{\sigma}} = \mathbf{f} + \epsilon_0 \mu_0 \frac{\partial \mathbf{S}}{\partial t}} \tag{A.20}$$

Eq. A.8 showed that the divergence of a second order tensor is a vector; the above equation is thus a vector equation. It is a statement about the conservation of momentum:

- From Newton's second law, **f** is the time rate of change in momentum density
- The second term on the right-hand side represents the change in electromagnetic momentum of the field, which is proportional to the energy-flux density **S** [40]
- Finally, the divergence of Maxwell's stress tensor thus represents the momentum flux density. The tensor itself represents the force per unit area, which is mechanically equivalent to pressure or stress

The implications of this equation become clearer when written in integral form for the force **F**, and when the time derivative of the Poynting vector is assumed to equal 0:

$$\mathbf{F} = \iiint_V \mathbf{f}\, dV = \iiint_V \nabla \cdot \overleftrightarrow{\boldsymbol{\sigma}}\, dV = \oiint_S \overleftrightarrow{\boldsymbol{\sigma}} \cdot d\mathbf{S} \tag{A.21}$$

Where in the final step, the divergence theorem was used. In other words, the *force per unit area* (pressure, or stress) resulting from the electromagnetic field equals the relevant component of the Maxwell stress tensor.

A.4. Applications

In motors and generators, the following simplifications are often used:

- The time derivative of the Poynting vector is neglected, as mentioned before
- The electric field is neglected
- Radial coordinates are used

Neglecting the electric fields gives

$$\sigma_{ij} = \frac{1}{\mu_0}\left(B_i B_j - \frac{1}{2}\delta_{ij} B^2\right) \tag{A.22}$$

And using radial coordinates (radial and tangential) simplifies this further to

$$\sigma_{rt} = \frac{1}{\mu_0}\left(B_r B_t - \frac{1}{2}\delta_{rt} B^2\right) \tag{A.23}$$

Now, the force per unit area dF in the radial and tangential (shear) direction can be derived. The radial force components correspond to the *normal* components of the force, and thus the diagonal components of $\overleftrightarrow{\boldsymbol{\sigma}}$

$$dF_r = \frac{1}{\mu_0}\left(B_r^2 - \frac{1}{2} \cdot 1 \cdot B^2\right) = \frac{1}{\mu_0}\left(B_r^2 - \frac{1}{2}B_r^2 - \frac{1}{2}B_t^2\right) = \frac{1}{2\mu_0}\left(B_r^2 - B_t^2\right) \tag{A.24}$$

Similarly, the tangential or *shear* forces equal the off-diagonal components of $\overleftrightarrow{\boldsymbol{\sigma}}$

$$dF_t = \frac{1}{\mu_0}\left(B_r B_t - \frac{1}{2} \cdot 0 \cdot B^2\right) = \frac{1}{\mu_0} B_r B_t \tag{A.25}$$

These two final results are often used in the analysis of forces inside a motor or generator.

B

Relative permeance due to slots

The procedure for introducing the effect of the stator slots into the magnetic flux density calculations is described in [96]. It consists of introducing a relative permeance which modulates the nominal air gap permeance, which is calculated by a conformal transformation of the slotted stator to an equivalent slotless stator. In this way, the tangential component of the flux density at the stator teeth and the change of the radial permeance at the slots can be taken into account.

By means of 4 conformal transformations, the set of equations as shown below is obtained, which uses the geometric parameters for a slot as shown in Figure B.1. For a given radial coordinate $s(r,\theta) = re^{j\theta}$, Equation B.1 is solved numerically for w. To avoid singularities, the complex permeance is calculated for $r = R_s - \epsilon$, a position just below the stator inner radius. When w is found, λ can be found using Equation B.8 and B.9.

$$z = \ln s = j\frac{g'}{\pi}\left[\ln|\frac{1+p}{1-p}| - \ln|\frac{b+p}{b-p}| - 2\frac{b-1}{\sqrt{b}}\arctan\frac{p}{\sqrt{b}}\right] + C \tag{B.1}$$

$$p = \frac{w-b}{w-a} \tag{B.2}$$

$$C = \ln R_s + j\theta_2 \tag{B.3}$$

$$b = \left[\frac{b'_o}{2g'} + \sqrt{\left(\frac{b'_o}{2g'}\right)^2 + 1}\right]^2 \tag{B.4}$$

$$a = \frac{1}{b} \tag{B.5}$$

$$g' = \ln\frac{R_s}{R_r} \tag{B.6}$$

$$b'_o = \theta_2 - \theta_1 \tag{B.7}$$

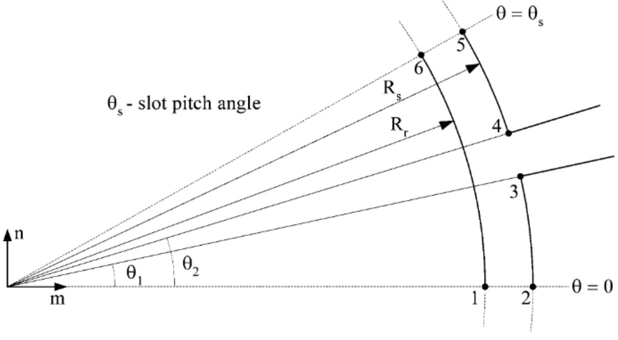

Figure B.1: The geometric parameters used to calculate the relative permeance[96]

$$\lambda = \frac{k}{s}\frac{w-1}{\sqrt{w-a}\sqrt{w-b}} \tag{B.8}$$

$$k = R_s e^{j\left(\frac{g'}{\pi}\ln w + \frac{\theta_s}{2}\right)} \tag{B.9}$$

As λ is a complex value, it can be written as

$$\lambda = \lambda_a + j\lambda_b \tag{B.10}$$

By calculating λ for a range of angles θ over the period of 1 slot pitch θ_s, the complex function $\lambda(\theta)$ is found. This function can then be expressed as a Fourier series using a discrete Fourier transform:

$$\lambda_a = \lambda_0 + \sum_{i=1}^{N_\lambda} \lambda_{ai} \cos\left(iN_s\theta\right) \tag{B.11}$$

$$\lambda_b = \sum_{i=1}^{N_\lambda} \lambda_{bi} \sin\left(iN_s\theta\right) \tag{B.12}$$

In which N_λ is the number of terms considered in the Fourier series. The solution has been verified with other available methods.[28] It was found that in the MATLAB implementation the easiest way to obtain λ_{ai} and λ_{bi} was to take the real part of the Fourier transform of λ_a and the negative imaginary part of the Fourier transform of λ_b respectively, resulting in the solutions shown in Figure B.2.

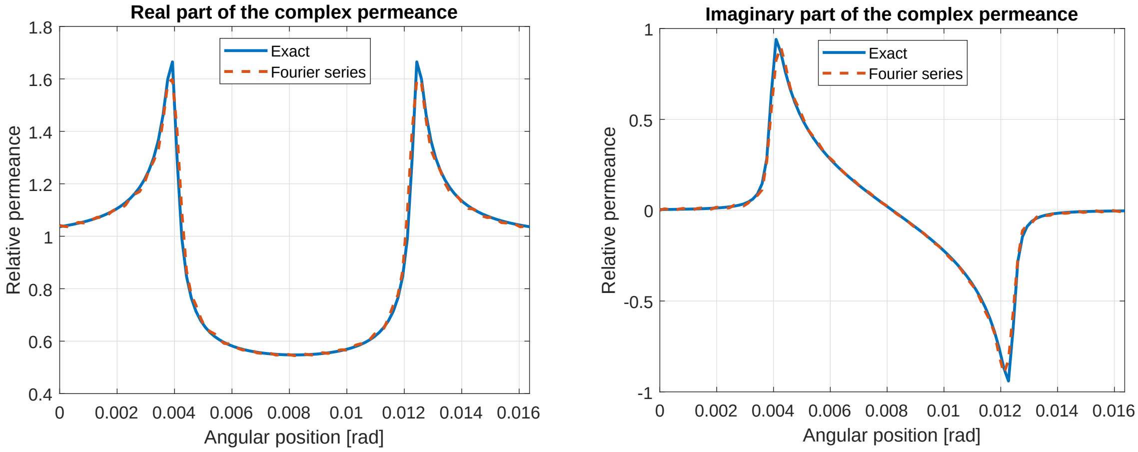

(a) Real part

(b) Imaginary part

Figure B.2: The relative permeance for one slot, including its Fourier series approximation

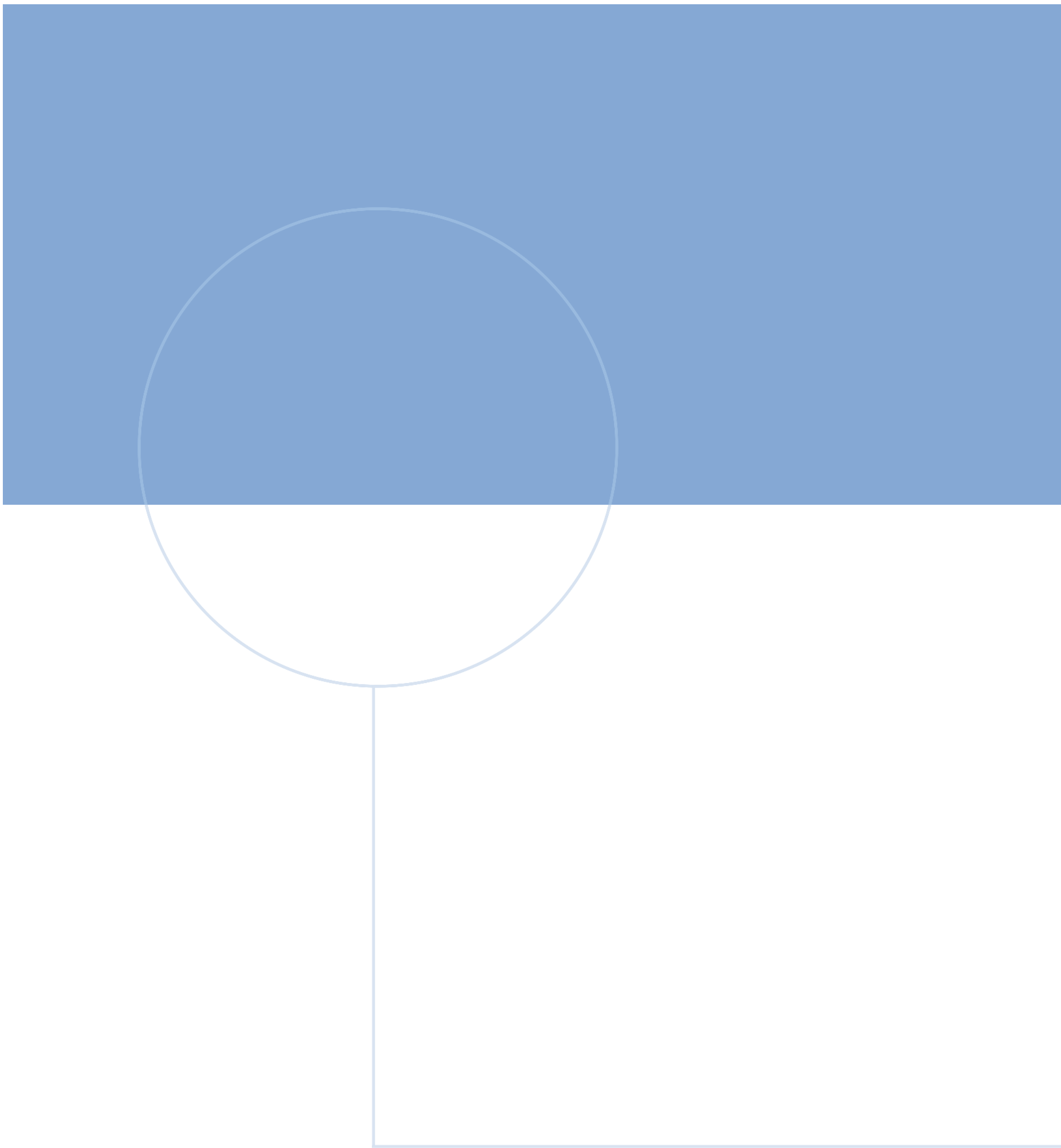

NTNU
Norwegian University of
Science and Technology

TU Delft